Title	The analysis of Ras/PIP3 self-organized localization pattern for spontaneous cell migration
Author(s)	福島, 誠也
Citation	大阪大学, 2019, 博士論文
Version Type	VoR
URL	https://doi.org/10.18910/72669
rights	
Note	

The analysis of Ras/PIP3 self-organized localization pattern for spontaneous cell migration

Submitted to Department of Biological Science,
Graduate School of Science, Osaka University

February 1, 2019

Seiya FUKUSHIMA

Abstract

Cell polarization is a common event that is necessary for cytokinesis, pinocytosis and migration of eukaryotic amoeboid cells. The remarkable example of cell polarity is the migration of Eukaryotic amoeboid cells. The decision making process of migration direction is composed of an asymmetricity in cell shape, arrangement of cytoskeleton, localization of signaling molecules and so on. Live cell imaging revealed some signaling molecules accumulate in an anterior part of a cell, that induces actin-polymerization and pseudopod formation. Especially, GTP form Ras (Ras-GTP) and PIP3 phosphatidylinositol lipid show asymmetric localization pattern on a cell membrane even in the absence of external stimuli and polarity in cell structures. In some conditions, Ras-GTP and PIP3 show self-organized spatiotemporal propagating wave pattern called Ras/PIP3 wave, that reflects a structure of signal transduction network related to cell polarization and symmetry breaking. Some mathematical models proposed the positive feedback regulations induced wave pattern formation; however, the mechanism remained unclear because of limitation of observation methods for signaling networks.

In this study, quantitative live cell imaging analysis revealed the spatiotemporal relationship between several major signaling components that includes Ras, PI3K, PTEN, PIP2 and PIP3 in the wave pattern. Especially, by using TIRF microscopy, I succeeded to analyze the behaviors of some molecules that had been difficult to observe before. As a result, I found that Ras-GTP/PI3K interaction governs the localization pattern of PIP3. Moreover, the spatiotemporal dynamics of the other components follow the dynamics of Ras-GTP. Besides, Ras-GTP exhibited wave pattern in self-organized manner, even without downstream signaling molecules including PIP3. This result illustrates that Ras is central to the emergence of excitable dynamics in the signaling pathways for asymmetric signal generation. Based on the experimental results, I constructed a new numerical model, and by simulation of the reaction-diffusion model, I confirmed the reproduction of the traveling waves of all these components observed experimentally. The molecular components essential for Ras excitability deserve further investigation. The analysis method developed in this study can be applied to screening of these components, that is expected to contribute progress of the research field.

abbreviation

ACF	Auto-correlation function
AKT	RAC-alpha serine/threonine-protein kinase or PKB
cAMP	Cyclic adenosine monophosphate
CCF	Cross-correlation function
DB	Development Buffer
DB-	Development Buffer without $CaCl_2$ and $MgCl_2$
FPS	Frame per second
GAP	Guanosine Triphosphate hydrolase activating protein
GEF	Guanine nucleotide exchange factor
GFP	Green fluorescent protein
HL5	HL5, the medium for *Dictyostelium Discoideum*
LatA	Latrunculin A
LB	Lysogeny Broth medium
LF	Low Fluorescent medium
PHD	PH domain, Pleckstrin homology domain
PI3K	Phosphoinositide 3-kinase
PIP2	Phosphatidylinositol (4,5)-bisphosphate
PIP3	Phosphatidylinositol (3,4,5)-trisphosphate
PKB	Protein kinase B or AKT
PLA2	Phospholipase A2
PLCδ1	Phospholipase C delta 1
PTEN	Phosphatase and tensin homolog
RBD	Ras binding domain
RFP	Red fluorescent protein
ROI	Region of interest
sGC	Soluble guanylyl cyclase
TIRFM	Total internal reflection fluorescence microscope
TMR	Tetramethylrhodamine
TorC	Target of rapamycin complex

Contents

Chapter 1

Introduction

1.1 Cell polarization for migration

Cell polarization commonly underlies essential cellular processes, including polarization, migration, pinocytosis, phagocytosis and division. It is one of the most fundamental question how and what components breaks symmetry during cell polarization process. Cell polarity in eukaryotic ameboid cell such as macrophages and *Dictyostelium Discoideum* is defined as an asymmetricity in cell shape, arrangement of the cytoskeleton and localization of signaling molecules. Live cell imaging studies of *Dictyostelium Discoideum*[1] have revealed the coupling of spontaneous localization of signaling molecules and fluctuation of cytoskeletal network drives pseudopod formation [4][14][38][19][21][24]. Some signaling molecules show an asymmetric localization pattern even in the absence of asymmetricity in the arrangement of cytoskeleton and external chemoattractant stimulation [77][51][39]. This means the signal transduction network has the ability to exhibit symmetry breaking spontaneously as well as response to external stimuli. The relationship between directed migration and spontaneous migration is now described as shown in Fig.1.1 [20]. Spontaneous asymmetrisity is generated in the signal transduction network and it induces spontaneous migration as a basal mode of motile cells. Chemotaxis is defined as biased spontaneous migration, in which chemoattractant only biases the frequency or probability of accumulation of signaling molecules along the specific direction. As a result, cells can migrate along the chemical gradient. In this way, the spontaneity of signal transduction network is an essential part of cell migration as well as polarization.

---

[1]The mechanism of cell migration in eukaryotic ameboid cells is commonly shared in many organisms, and many molecules are well conserved among different organisms [4][13][83][146][28]. The findings on polarization, chemotaxis and spontaneous migration introduced later are basically obtained from study using *Dictyostelium Discoideum*.
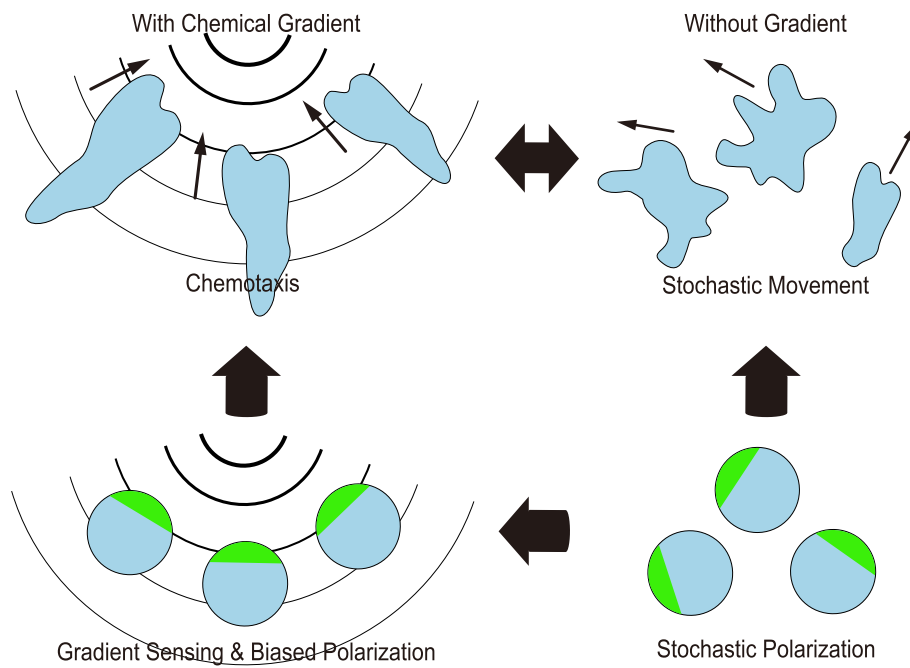
Figure 1.1: Polarization and directed migration.
Eukaryotic cells recognize the gradient of a chemoattractant and move toward the chemoattractant source. Random cell migration is caused by spontaneous polarization of the intra cellar signaling network. Recent studies have shown that the polarization along a gradient is achieved by the bias of spontaneous polarity.

1.2 Signal transduction network for cell polarization

Cells sense extracellular chemicals, organisms and other information with receptors on the cell membrane. This information is transmitted from the G-protein coupled receptors (GPCR)[2] to the intracellular signal transduction network by heterotrimeric G proteins, and processed in it (Fig.1.2) [5][6][10]. Finally, signal transduction network induces cell migration via regulation of the cytoskeletal network [10][75][15][100][101][124][31][33][126]. As described above, the molecules constituting the signal transduction network form an asymmetric localization pattern spontaneously on the cell membrane. A representative example is the localization pattern of GTP bound Ras (Ras-GTP) [94][77][103]. The localization of Ras-GTP is observed in the absence of external stimulus, and in mutant, which lacks heterotrimeric G proteins [81]. The localization pattern has been observed even without cytoskeletal network as well as polarity in cell shape after inhibition of F-actin by treatment of actin polymerization inhibitor, Latrunculin A [10][75][39]. These facts indicate that asymmetricity is generated in the signal transduction network.

The signal transduction network is constructed of many elements besides Ras. There are four major pathways, that are PIP3 pathways, TorC2 pathway, sGC pathway and PLA2 pathway [115][116][10][75][62][76][15][81][124]. PIP3 is phosphatidylinositol lipid that is phosphorylated at the 3rd, 4th, and 5th carbon positions of inositol ring. PIP3 is produced from PI(4, 5)P2 (PIP2) by phosphorylation with PI3K (kinase for the 3rd carbon position of inositol ring) and degraded by dephosphorylation by PTEN (phosphatase for the 3rd carbon position of inositol ring). PIP3 pathway is deeply involved in cell movement, adhesion, division, phagocytosis and so on [73][74][75][62][51][66][79]. *pi3k* knockout mutant, which cannot produce PIP3, shows a decrease in migration velocity and a decrease in the cell division rate[3]. *pten* knockout mutant, in which PIP3 becomes excessive, also shows a decrease in migration velocity, a decrease in cell division rate, multiple pseudopods formation and abnormally elevated adhesion [62]. PIP3 activates PKBA (or AKT) and affects chemotaxis ability, especially, at shallow gradients [82]. Since the phenotype is clear, PIP3 pathway has been studied actively. TorC2 is a complex with Tor, PiaA, Rip3, Lst8 and so on, which activates PKBA,PKBR1 and etc., and transmits a chemotactic signal [124]. It is known that TorC2 pathway works independently of PIP3 pathway in chemotaxis, and chemotactic ability drops greatly when both pathways are inhibited [12][121][122]. sGC pathway is involved in the pro-

---

[2]*Dictyostelium Discoideum* does not have receptor tyrosine kinase. GPCR is the main receptor mediating chemoattractant such as cAMP (receprtor: cARs [1][2][3][6][7][8][9]) and foric asid (receptor: fARs [35]).

[3]*pi3k* knockout mutant can hardly proliferate in the axenic medium.

duction of cGMP, which activates cGMP-binding candidate proteins, GbpA
to D [117][119]. Among them, GbpC is involved in the regulation of Myosin
II that induces cell contraction in the posterior part of a cell [118]. In addi-
tion, it has been reported that sGC localizes in pseudopods and is involved
in chemotaxis by regulating the direction change frequency [119]. PLA2
pathway was discovered as a pathway involved in chemotaxis under PIP3
inhibition condition. It has been reported that PLA2 pathway functions as
a memory of motile direction in chemotaxis [120]. In signaling cascade for
chemotaxis, Ras is located upstream of other pathways, and Ras is thought
to act as a hub of information from GPCR. Among the Signaling Networks,
there are many reports about feedback regulation and crosstalk between the
pathways, that caused the complicated behavior of the system. The im-
portant problem we should solve first is to clarify how symmetry breaking
occurs from which molecule in the signal transduction network.

Figure 1.2: Diagrams of Signaling network.
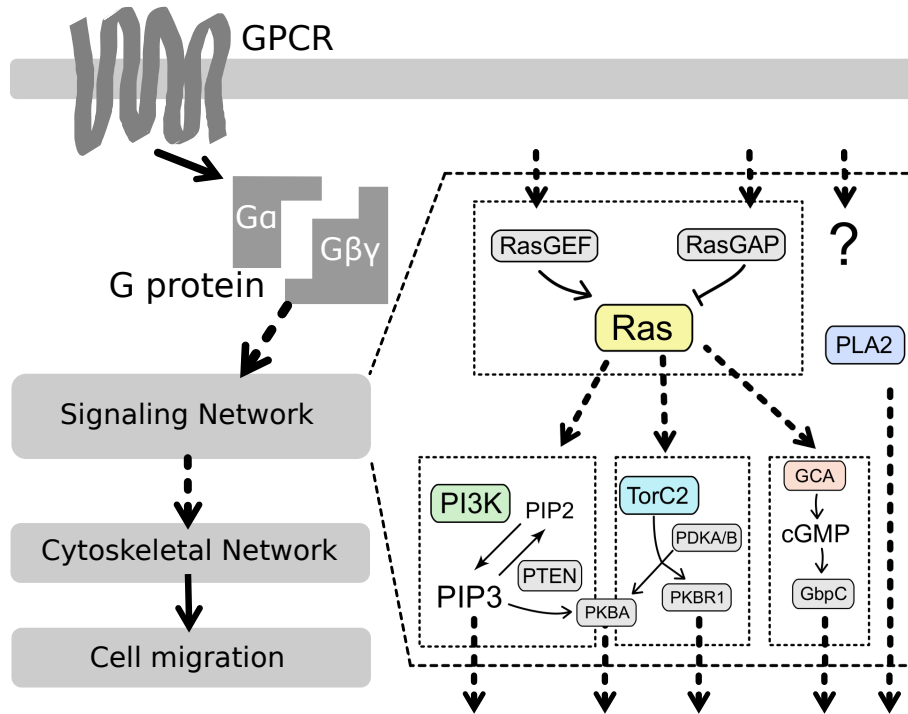The left column shows the outline of chemotactic signal transduction. External
stimuli activate GPCR, G-proteins and downstream signaling network. Among
the signaling network, asymmetric signals are generated and finally, it induces cell
migration. The right column shows detail on signaling network, in which the rela-
tionship between Ras, PIP3, TorC2, sGC, PLA2 pathways are summarized.

1.3   Excitable signaling network

As an answer to the problem "How the symmetry breaking occurs?", excitability is leading candidate. Excitability in biology has been well documented experimentally and theoretically in the study about the generation of the action potential in neurons [157][158]. The generation of the action potential is characterized by threshold for all-or-none response, constant magnification of the response, transient response, refractory-period and propagation with no reduction, which are explained by two feedback regulations, fast positive and delayed negative feedbacks (Fig.1.3). In the Hodgkin-Huxley model, voltage-gated sodium channel corresponds to fast positive feedback, that ensures all-or-none response and propagation of action potential generation. Close of sodium channel and open of potassium channel following an action potential correspond to delayed negative feedback, that ensured transient response and the refractory-period of the membrane potential. When considering about randomness, threshold for all-or-none excitation enables spontaneous response by internal fluctuations or molecular noise that are larger than the threshold, even without an external stimulus [159]. Besides, a chain-reacting generation of action potential contributes to propagation and spatiotemporal pattern formation of the membrane potential. The important point is such spontaneous response breaking symmetry, which is achieved by characteristic two feedback regulations.

Similar findings have been made in many other cellular phenomena such as cell differentiation [161][163], gene expression [162][164] and eukaryotic chemotaxis [21][27]. In the context of signal transduction network, the properties of excitable systems provide mechanisms for spontaneous pattern formation, by which a signaling domain is generated locally on the cell membrane, leading to symmetry breaking. In fact, recent evidence has revealed that chemotactic signaling pathways in *Dictyostelium* cells exhibit the characteristics of excitable systems [131][42][28][114]. Major signaling pathways such as the PIP3, TorC2 and sGC pathways can generate an all-or-none signal asymmetrically along extracellular cAMP gradients for directed cell migration [30][36]. Evidence for excitability in the PIP3 pathway includes stimulation-induced all-or- none excitation, spontaneous excitation, and traveling wave generation of the PIP3-enriched domain (PIP3 domain), and also refractory behavior in the PIP3 excitation, a phenomenon observed typically in excitable systems [131][134][136][45]. Mammalian cells also exhibit the traveling wavelike localization patterns of PIP3 [150]. This experimental evidence leads to a hypothesis that the excitability in chemotactic signaling pathways is a common feature for asymmetric signal generation in various chemotactic cells. To gain insights into the network structure that generates the evolutionary conserved dynamics for cell polarity and motility, it is important to clarify which molecules in the signaling network work as key determinants for the emergence of excitable dynamics that generate asymmetric signals.
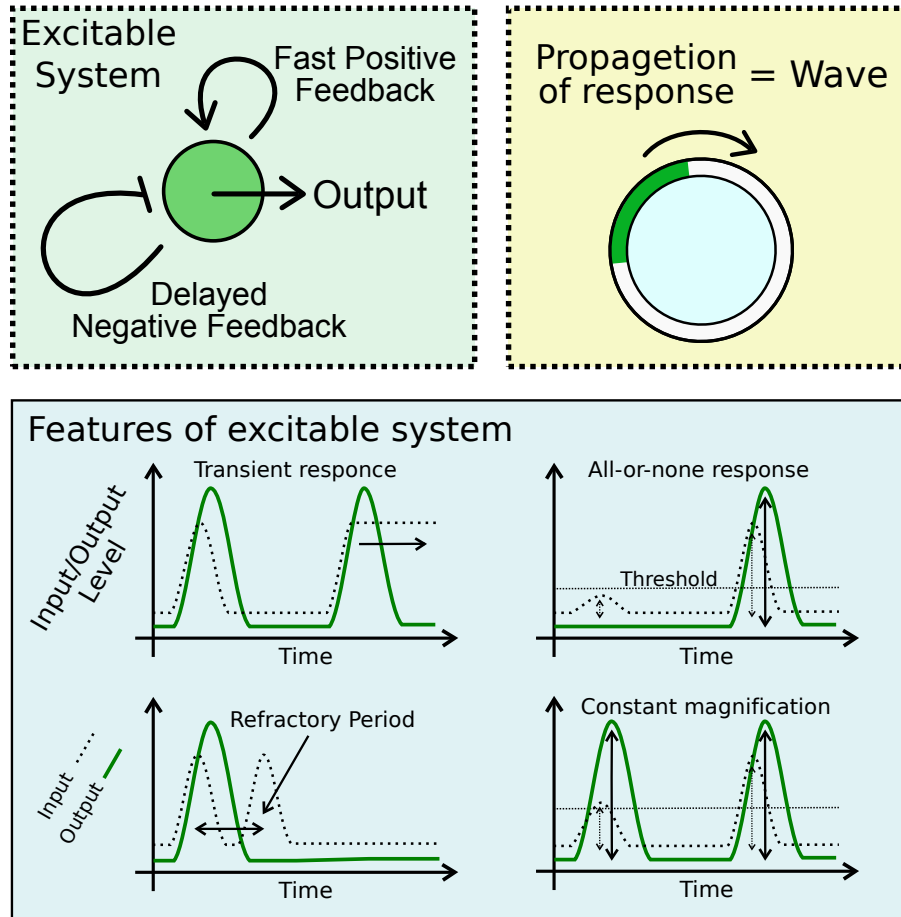
Figure 1.3: Key Features of excitable system.
The top left column shows the simplest model of excitable system containing two feedback regulations. The top right column shows the propagation of the response of excitable system. In this case, active state of membrane proteins or lipids is expected to mediate the local signal on the cell membrane, and its propagate neighborhoods. The bottom column shows characteristic features of excitable system. Transient response (top left), all-or-none response and threshold (top right), refractory period (bottom left) and constant magnification of the response (bottom right).

1.4 Ras/PIP3 signaling network

Ras and PIP3 signaling networks are key regulation pathways of cell polarization [86]. Ras-GTP and PIP3 show asymmetric localization on a cell membrane against chemoattractant stimulus. This response satisfied with the properties of excitable mechanism [42][43][28]. Ras-GTP/PIP3 shows traveling wave pattern called Ras/PIP3 wave in specific conditions, that is also an important nature caused by excitability of the system [39]. Ras-GTP is known as upstream of PIP3 in chemotactic signal transduction network and PIP3 signaling network induces pseudopod formation [75]. Ras-GTP is visualized by fluorescent protein tagged Ras binding domain (RBD) from human Raf1 protein [94]. Ras-GTP is positively regulated by guanine nucleotide exchange factors (GEFs) and negatively regulated by GTPase activating proteins (GAPs) [88][90][92]. In *Dictyostelium discoideum* cells, at least 14 Ras small GTPase family proteins, 25 RasGEFs, and 14 RasGAPs are estimated from the genome sequence [84][85][87][89][95][28][22]. Among the Ras family proteins, RasG and RasD mainly regulate PIP3 signaling network. RasGEF R is one of the important activator mediating chemotactic signal, and RasGAP NfaA is one of the important deactivator suppressing Ras activity globally [97][99].

PIP3 is visualized by fluorescent protein tagged PH domain (PHD) from PKBA(AKT) protein, which has binding specificity for PI(3,4,5)P3 [46][47][10][50][52][54][57][58]. *Dictyostelium discoideum* has six PI3Ks, PI3K1 to 6. PI3K1, 2 and 3 are important for cell migration and polarization [75][80][16]. PI3K1 to 3 are homologous to human class I PI3K p110 γ catalytic subunit (Hs p110 γ) and have same domain structure containing catalytic domain, accessory domain, C2 domain and Ras binding domain (Fig.1.4). Especially, catalytic activity of PI3K2 is higher than that of PI3K1 and 3. Interaction with Ras-GTP is necessary for activation of PI3K2 and RBD mutant of PI3K2 (PI3K2K857, 858E or PI3K(KE)) that cannot interact with Ras-GTP, cannot rescue the phenotype of *pi3k1-2* null strain [75]. *Dictyostelium* PI3Ks have N-terminus domain called "targeting domain" that is also necessary for PI3K2 catalytic activity. N-terminus truncate of PI3K2 (N-PI3K; 2-561aa of PI3K2) shows an F-actin dependent pseudopod localization regardless of other domains. PTEN is phosphatase of PIP3, that regulates PIP3 signal in a negative manner and shows mutually exclusive localization pattern with PIP3 [62][37][67][41][44]. It is expected that positive regulation from PIP2 to PTEN [63], and negative regulation from PIP3 to PTEN [72]. A recent study reported that GTP bound Arf small G protein is essential for PTEN membrane localization (Degawa 2019, under submission). PIP2 (PI(4,5)P2) is a precursor of PIP3, that mainly generated from phosphorylation of PI(4)P by PI5K [60]. PIP2 is visualized by PHD from PLCδ1 protein, but only slight change was observed while PIP3 shows a drastic change [40].

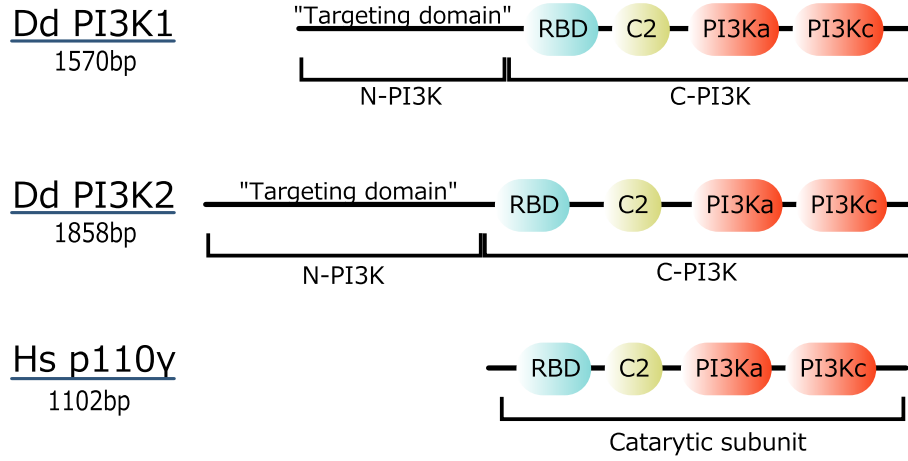The localization patterns of Ras-GTP and PIP3 are coincident in sev-

Figure 1.4: The domain structure of PI3K.
The PI3K domain structure is shown, that contains the catalytic domain (PI3Kc),
accessory domain (PI3Ka), C2 domain (C2) and Ras binding domain (RBD).

eral conditions. Ras/PIP3 co-localization was observed in the pseudopod,
phagocytic cups and on the whole of the plasma membrane during responce
for chemoattractant [77][78][52][81][40][34]. Stimulation by cAMP induces
a transient increase of Ras-GTP, PI3K and PIP3 on the membrane. First,
Ras-GTP and PI3K level increase, and PIP3 level increase following them
[77]. After that, Ras and PIP3 decrease, but PI3K remains on the membrane
for several seconds. In *pi3k* null strain, PIP3 production has never observed
any more, but Ras-GTP and N-terminus domain of PI3K still show localiza-
tion in the pseudopod. PTEN also shows the localization pattern in opposite
side of higher chemoattractant [62]. No membrane localization of PI3K was
reported under F-actin inhibit condition by Latrunculin A, in spite of the
localization pattern of Ras-GTP, PIP3 and PTEN. Besides, inhibition of
PI3K by PI3K inhibitor LY294002 results in disappearance not only PIP3
but also RBD localization patterns [39]. From these results, it is thought
that localization patterns of Ras-GTP, PIP3 and PTEN are closely regulated
each other and feedback regulation from PIP3 and its downstream compo-
nents also affects on activity of Ras and PI3K. These regulations are also
important for understanding of the symmetry breaking process, however,
the question how and which molecules breaks symmetry remains unclear.

In order to simplify the question, our group focused on the stochastic lo-
calization pattern formation of Ras-GTP and PIP3 which occurred without
external stimuli and cytoskeletal networks. Previously, it was reported that
Ras-GTP and PIP3 shows traveling wave pattern after treatment of Latrun-
culin A and Caffeine [39]. The models of PIP3 traveling wave pattern were
proposed from some groups [131][134][136]. Because the wave pattern was

vanished after treatment of LY294002, our group proposed PIP3 wave pattern model (called Shibata model, Fig.1.5) in which PIP3/PIP2 metabolism and mutual exclusion between PIP3 and PTEN constructs an excitable system. This model can well reconstruct the experimental data by numerical simulation. There are three hypotheses in this model, that are negative regulation from PIP3 to PTEN, positive regulation from PIP2 to PTEN, and inflow and outflow of PIP2 and PIP3. In this study, I started from verification of the Shibata model and try to reveal the mechanism of Ras-GTP and PIP3 wave pattern formation and symmetry breaking.
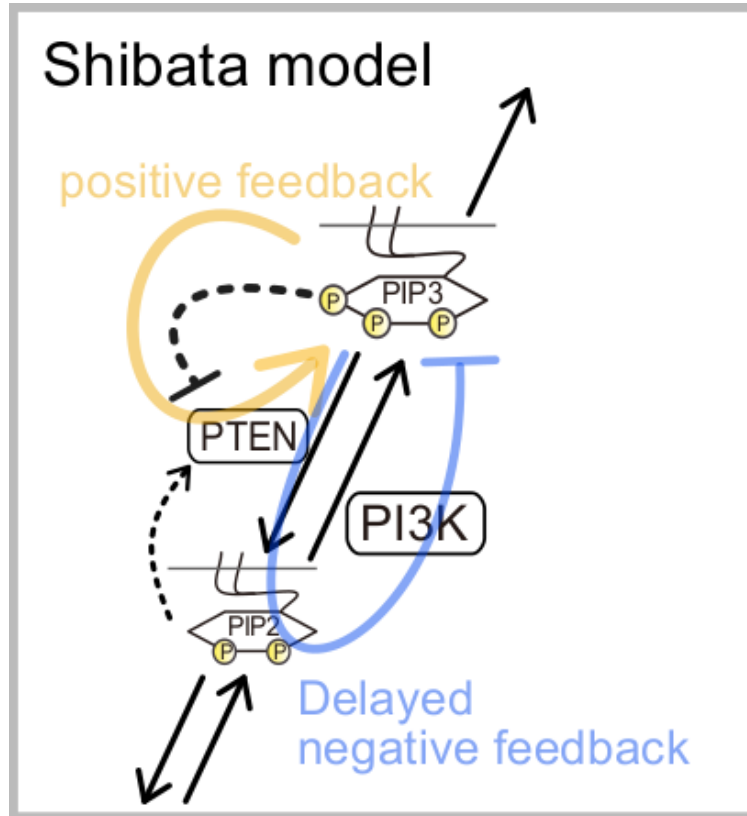

Figure 1.5: The scheme of Shibata model.
This model is explained by two feedback regulations, one is fast positive feedback composed of mutual inhibition between PIP3 and PTEN, the other is delayed negative feedback composed of inflow of PIP2 and outflow of PIP3.

1.5 Result summary

In order to reveal the network structure of Ras/PIP3 signaling and the mechanism of traveling wave pattern formation, I performed imaging study of Ras/PIP3 wave. By using Total Internal Reflection Fluorescent Microscopy (TIRF microscopy), I succeed in comprehensive observation of components of Ras/PIP3 wave including Ras-GTP, PIP3, PIP2, PTEN and PI3K on a membrane. PIP2 showed a negative correlative localization pattern with PIP3. PI3K showed membrane translocation that precedes accumulation of PIP3. Membrane translocation of PI3K regulated by Ras-GTP and localization pattern of PI3K coincided tightly with that of Ras-GTP. Ras-GTP wave as well as PI3K wave preceded PIP3 wave. Rescue experiment of *pi3k1-5* null strain revealed that PIP3 wave depended on PI3K activation by Ras-GTP/PI3K interaction. Additionally, Ras wave was observed even in *pi3k* null cells and WT cells treated with PI3K inhibitor LY294002, in spite of absence of PIP3 wave. These results indicate Ras wave is dominant in the asymmetric localization pattern formation of signaling molecules. Based on the experimental results, I developed a reaction-diffusion model that reproduced the Ras/PIP3 waves and interrelationships between all components observed experimentally. These results illustrated that Ras is central to the emergence of excitable dynamics for asymmetric signal generation and that Ras excitability is modulated by feedback regulation from downstream signaling molecules to stabilize the asymmetric signal for cell motility.

Chapter 2

Materials and Methods

2.1 Materials

2.1.1 Plasmids Construction

Plasmids were generated by Ligation or In-Fusion methods (TOYOBO, TaKaRa). All plasmids used in this study are shown in Table.2.1. As a vector for plasmids, I used pHK12 series[170] or pDM series[169]. All constructs were sequenced and checked with genomic sequence before transformation [168]. To visualized localization of PI3K2 and its mutants, Halo-tag fused PI3K2 were expressed. Ras binding mutant of PI3K2 (PI3K2^{K857,858E}) and truncates of N-PI3K2 (PI3K2$^{\Delta561-1859}$) and C-PI3K2 (PI3K2$^{\Delta2-560}$) were obtained by PCR (TOYOBO)[166]. I created optimized versions of PHD$_{PLC\delta1}$-GFP pHK12 plasmid for *Dictyostelium* cells in order to improve the expression level of PHD$_{PLC\delta1}$-GFP. I changed 5' sequences of PHD$_{PLC\delta1}$-GFP to high codon usage sequence, from ATGcacggcctacaggatgatgaggatctacaggcgctgctg to ATGcatggtttacaagatgatgaagatttacaagctttattaaaa by PCR [167].

2.1.2 Cell culture and constructs

Dictyostelium Discoideum wild-type Ax2 was used as the parental strain except gc null strain (Ax3) [165]. All constructs used in this study are shown in Table.2.2. Cells were transformed with plasmids by electroporation. Electroporation method is based on [171]. In my method, electroporate the cells at 0.65 kV and 25 μF twice, waiting for about 1 s between pulses. To observe spatiotemporal dynamics of Phosphatidylinositol lipids and their related enzymes, pairs of PHD$_{AKT/PKB}$-GFP or RFP, GFP-Nodulin, PTEN-Halo or GFP, PI3K-Halo and RBD$_{Raf1}$-GFP were co-expressed respectively. Cells were cultured axenically in HL-5 medium containing G418 (20μg/ml), Blasticydin S (10μg/ml) or hygromycin (50μg/ml) at 21 ℃ [172] (Watts and Ashworth, 1970).

Table 2.1: Plasmids List

No.	Plasmid name
1-1	RBD_{Raf1}-GFP pDM181
1-2	RBD_{Raf1}-GFP pDM358
1-3	RBD_{Raf1}-RFP pDM358
1-4	RBD_{Raf1}-RFP pDM344
2-1	$PHD_{AKT/PKB}$-GFP pHK12 neo
2-2	$PHD_{AKT/PKB}$-GFP pHK12 bla
2-3	$PHD_{AKT/PKB}$-GFP pDM358
2-4	$PHD_{AKT/PKB}$-RFP pHK12 bla
2-5	$PHD_{AKT/PKB}$-RFP pDM358
2-6	$PHD_{AKT/PKB}$-RFP pDM344
3-1	PTEN-GFP pHK12 bla
3-2	PTEN-Halo pHK12 neo
3-3	PTEN-Halo pHK12 bla
3-4	PTEN-GFP-Halo pHK12 neo
3-7	hPTEN-Halo pHK12 neo
4-1	PI3K2-Halo pHK12 neo
4-2	PI3K2-Halo pHK12 bla
4-3	$PI3K2^{K857,858E}$-Halo pHK12 neo
4-4	$PI3K2^{K857,858E}$-Halo pHK12 bla
4-5	N-PI3K2-Halo pHK12 bla
4-6	C-PI3K2-Halo pHK12 bla
5-1	GFP-Nodulin pDM358
5-2	RFP-Nodulin pDM358
5-3	Halo-Nodulin pDM358
6-1	$PHD_{PLC\delta1}$-GFP pHK12 neo
7-1	$LimE_{\Delta coil}$-RFP
8-1	GFP-Nodulin $PHD_{AKT/PKB}$-RFP pDM358
8-2	$PHD_{AKT/PKB}$-GFP RBD_{Raf1}-RFP pDM358
8-3	RBD_{Raf1}-GFP $PHD_{AKT/PKB}$-RFP pDM358
9-1	GbpD-GFP pHK12 neo
9-2	sGC-RFP pHK12 bla
9-3	nfaA-Halo pHK12 bla

Table 2.2: Constructs List

Main Gene	Construct Name	Starvation time
RBD	RBD$_{\text{Raf1}}$-GFP /Ax2	
	RBD$_{\text{Raf1}}$-GFP /*pten* null	
	RBD$_{\text{Raf1}}$-GFP /*pi3k1-5* null	
	RBD$_{\text{Raf1}}$-GFP /*gc* null (Ax3)	
	RBD$_{\text{Raf1}}$-RFP & PHD$_{\text{AKT/PKB}}$-GFP /Ax2	3h
	RBD$_{\text{Raf1}}$-RFP & PHD$_{\text{AKT/PKB}}$-GFP /*pi3k1-5* null	
	RBD$_{\text{Raf1}}$-GFP & PI3K2-Halo /Ax2	
	RBD$_{\text{Raf1}}$-GFP & PTEN-Halo /Ax2	
	RBD$_{\text{Raf1}}$-RFP & GFP-Nodulin /Ax2	
PI3K	PI3K2-Halo/Ax2	3h
	PI3K2-Halo/*pi3k1-5* null	
	PI3K2-Halo & PTEN-GFP/Ax2	
	PI3K2-Halo & PHD$_{\text{AKT/PKB}}$-GFP/Ax2	
	PI3K2$^{\text{K857,858E}}$-Halo & PHD$_{\text{AKT/PKB}}$-GFP/Ax2	3h
	N-PI3K2-Halo & PHD$_{\text{AKT/PKB}}$-GFP/Ax2	
	C-PI3K2-Halo & PHD$_{\text{AKT/PKB}}$-GFP/Ax2	
PHD	PHD$_{\text{AKT/PKB}}$-RFP & PHD$_{\text{PLC}\delta1}$-GFP /Ax2	4.5h
	PHD$_{\text{AKT/PKB}}$-RFP & GFP-Nodulin /Ax2	
	PHD$_{\text{AKT/PKB}}$-GFP & LimE$_{\Delta\text{coil}}$-RFP /Ax2	
	PHD$_{\text{AKT/PKB}}$-GFP /*pten* null	3h
	PHD$_{\text{AKT/PKB}}$-GFP /*pi3k1-5* null	
PTEN	PTEN-Halo & GFP-Nodulin /Ax2	
	hPTEN-Halo & PTEN-GFP /Ax2	5h
	hPTEN-Halo & PHD$_{\text{AKT/PKB}}$-GFP /*pten* null	
GbpD	GbpD-GFP & PHD$_{\text{AKT/PKB}}$-RFP /Ax2	3∼4h
sGC	sGC-RFP & PHD$_{\text{AKT/PKB}}$-GFP /Ax2	3∼4h
nfaA	nfaA-Halo & PHD$_{\text{AKT/PKB}}$-GFP /Ax2	3∼4h

2.1.3 Reagents

Detail about regents used in this study is shown in 2.3. The concentration of the reagent is described later. Basically the use of reagents complies with the instructions of the reagents.

Table 2.3: Reagents List

Drug Name	Manufacture	Catalog number
Latrunculin A	SIGMA	Cat#L5163
LY294002	Cayman	Cat#154447-36-6
Torin2	TOCRIS	Cat#4248
BPB	TCI Japan	Cat#A5501
Halo-tag TMR ligand	Promega	Cat#G8251
Ligation High	TOYOBO	Cat#LGK-101
KOD Plus- Ver.2	TOYOBO	Cat#KOD-211
In Fusion HD Cloning kit w/Cloning Enhancer	TaKaRa	Cat#639634

2.2   Methods

2.2.1   Preparation for live cell imaging

For imaging experiments, cells were washed in 1 ml development buffer without Ca++ and Mg++ (DB-; 5 mM Na2HPO4 and 5 mM KH2PO4) twice and starved in 1ml development buffer (DB; DB-, 2 mM MgSO4 and 0.2 mM CaCl2) for 3 to 4 hours at a density of 5.0×10^6 cells per ml on 35 mm dish. Halo-tag (Promega) fused proteins were stained with 2 μl Halo-tag TMR ligand for 30 min and washed 5 times with 1ml DB- before observation.

2.2.2   Imaging with confocal microscope

Confocal imaging was performed using an inverted microscope (ECLIPSE Ti; Nikon) equipped with a confocal unit (CSU-W1; Yokogawa) (Table.2.4). Laser sources for 488 nm and 561 nm excitation light were solid-state CW lasers (OBIS 488NM X 50MW and OBIS 561NM X 50MW, respectively; COHERENT). Time-lapse images were acquired through a 60 × oil immersion objective lens (CFI Apo TIRF 60X Oil, N.A. 1.49; Nikon) with an EM-CCD camera (iXon3 897; Andor). Cells were transferred to a 35 mm Glass Base Dish (Grass 12 ϕ, 0.15-0.18 thick; IWAKI) and suspended in 200 μl DB with 4 mM caffeine and 5 μM Latrunculin A (SIGMA). Inhibitors were added after 15 min treatment with caffeine and Latrunculin A. Latrunculin A (2 mM), LY294002 (40 mM), Torin2 (1 mM) and BPB (10 mM) in DMSO were diluted to the final concentration (DMSO 1%). Time-lapse images were obtained at 200 ms exposure for each channel at 2 s intervals (488 nm laser power was 50 μW, and 561 nm laser power was 150 μW).

Table 2.4: Spinning disk Confocal microscope

Part name	details
Housing	ECLIPSE Ti; Nikon
Confocal Unit	CSU-W1; Yokogawa
Objective lens	CFI Apo TIRF 60X Oil, N.A. 1.49; Nikon (NA 1.49)
CCD	iXon3 897; Andor (EMCCD, 512×512pixels)
Laser 1	OBIS 488NM X 50MW; COHERENT (output 488nm, 50mW)
Laser 2	OBIS 561NM X 50MW; COHERENT (output 561nm, 50mW)
Software	NIS-Elements AR; Nikon

2.2.3 Imaging with TIRF microscope

TIRF imaging was performed using an inverted microscope equipped with a handmaid prism-less TIR system [154] (Fig.2.1, Table.2.5). Laser sources for 488 nm and 561 nm excitation light were solid-state CW lasers (SAPPHIRE 488-20 and Compass 561-20, respectively; COHERENT). Lasers were guided to the back focal plane of the objective lens (CFI Apo TIRF 60X Oil, N.A. 1.49; Nikon) through a back port of the microscope. TIR and EPI illumination were switched by tilting the incident angle of the lasers. The separated images were passed through dual band laser split filter sets (Di01-R488/561-25×36, Di02R561-25×36, FF01-525/45-25 and FF01-609/54-25; Semrock; Fig.2.2.3) and captured by two EM-CCD cameras (iXon3 897; Andor) equipped with 4 × intermediate magnification lenses (VM Lens C-4 ×; Nikon). To reduce nonspecific fluorescent signals, carefully washed cover glasses and filtered buffers were used. Cells were transferred to a cover glass (25 mm radius, 0.12-0.17 thick; MATSUNAMI) that was fixed on a chamber (Attofluor Cell Chamber; Molecular Probes). The cover glass was washed by sonication (Branson 1800; Emerson Japan) in 0.1 M KOH for 30 min and in 100% EtOH for 30 min twice in advance. Cleaning solutions were washed away with milli-Q water at intervals. Cells were treated with 4 mM caffeine and 5 μM Latrunculin A in DB for 15 min. Time-lapse images were obtained at 100 ms exposure for 10 min (488 nm laser power was 20 μW, and 561 nm laser power was 20 μW). Time-lapse images were smoothed with a 1 s time window to reduce shot noise.

Table 2.5: TIRF microscope for dual color

Part name	details
Housing	ECLIPSE Ti; Nikon
TIR optics	built in laboratory
Objective lens	CFI Apo TIRF 60X Oil, N.A. 1.49; Nikon (NA 1.49)
Dichroic mirror 1	Di01-R488/561-25×36; Semrock
Dichroic mirror 2	Di02-R561-25×36; Semrock
Filter	FF01-525/45-25, FF01-609/54-25; Semrock
CCD	iXon3 897; Andor (EMCCD, 512×512pixels)
Laser 1	SAPPHIRE 488-20; COHERENT (output 488nm, 20mW)
Laser 2	Compass 561-20; COHERENT (output 561nm, 20mW)
Software	iQ2; Andor

2.2.4 Image processing and analysis

The adjustment of images from a dual camera was performed on software by using objective micrometer images as a standard. The average error of
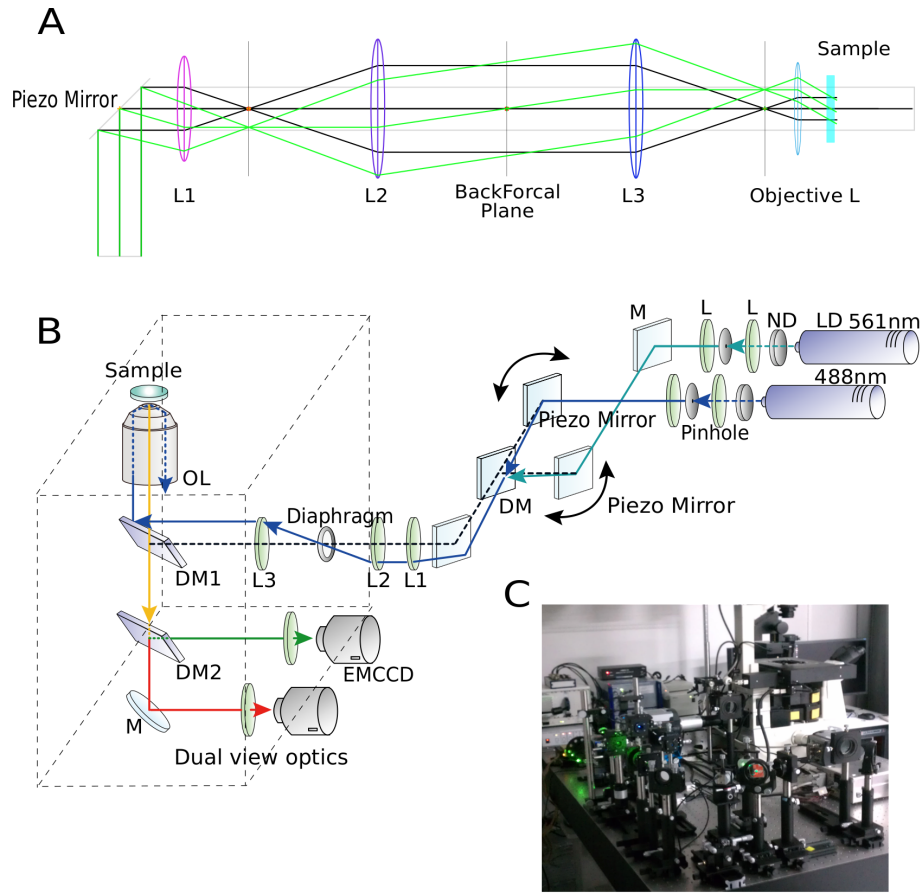
A

Sample

Piezo Mirror

L1 L2 BackForcal Plane L3 Objective L

B

Sample

OL

Diaphragm

DM1 L3 L2 L1

DM

M L L ND LD 561nm

488nm

Piezo Mirror

Pinhole

Piezo Mirror

DM2

EMCCD

M

Dual view optics

C

Figure 2.1: Overview of the constructed microscope.
A. TIRF optics diagram of the constructed microscope. Piezo mirror and three lenses to construct TIR illumination were used. **B.** Schematic diagram of the constructed microscope. TIR illumination and the dual view optics were combined. "L" represents a lens, "M" represents a mirror, and "ND" represents an ND filter. **C.** Picture of the constructed microscope.
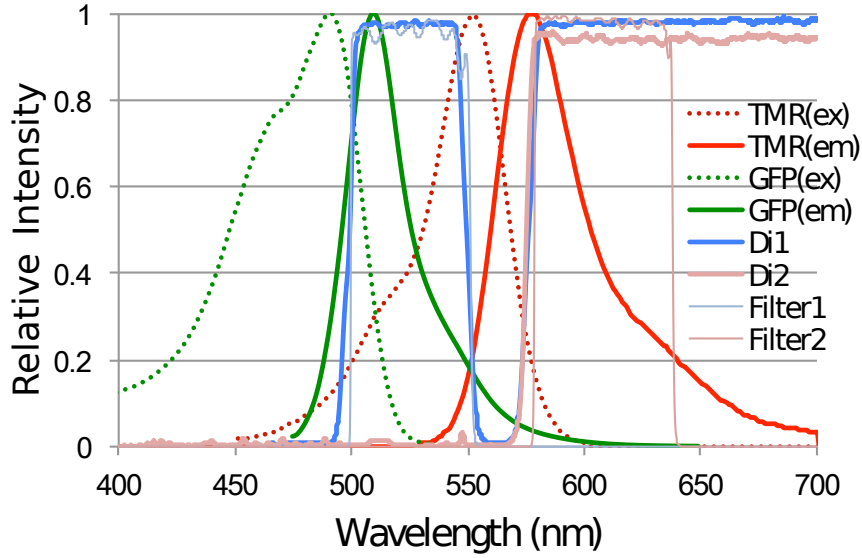
Figure 2.2: Specification of the filter set.
The model numbers of the filter sets used in this study are listed in Table.2.5.

the position after adjustment was less than 66 nm^2 (Fig.2.3). Leakage from one channel to the other was calibrated as:

$$S1_{detected} = S1 + bg_1 + Leak_{2to1} \cdot S2 \tag{2.1}$$

$$S2_{detected} = S2 + bg_2 + Leak_{1to2} \cdot S1 \tag{2.2}$$

S1 and S2 indicate the fluorescence signals from the two channels. S´ indicates the detected signal, Bg indicates the background noise and L indicates the ratio of leakage from one signal to the other channel. Leakage parameters for GFP, RFP and TMR were obtained in advance. By this correction, leaking effect become lower than noise level (Fig.2.3). Spatiotemporal dynamics of fluorescent intensity were analyzed with time trajectories. In the case of TIRF time-lapse images, time trajectories were obtaiened by the time-axis profiles of the average intensity in a ROI (region of interest). We defined the ROI as a circle with 0.2 μm (3 pixels) radius. In case of confocal time-lapse images, the fluorescence intensities were analyzed as previously described [39]. Fluorescence intensity along the rounded cell contours were measured in each frame. The intensity profiles were plotted against an angle θ and time as a 2D pattern. The line profile along the time axis was defined as the time trajectory of the membrane localization.
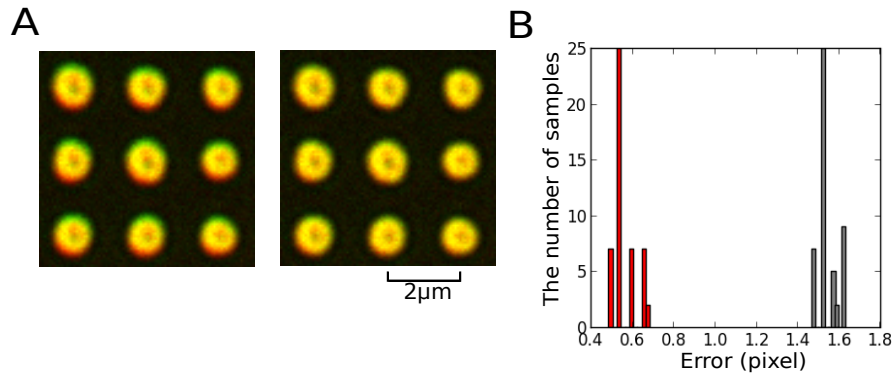
Figure 2.3: Alignment of dual view.
A. Images obtained with two cameras were overlapped with pseudo colors of green and red, respectively. The left image is before correction. There are some parts where colors look green and red, indicating that the two images do not match. The right image was improved on the software. **B.** The histogram of the deviation of the center coordinates of each spot of the objective micrometer before correction (black) and after correction (red). There is 1.5 pixels (100nm) error before the correction, which shifted to around 0.5 pixels (33nm) after the correction.
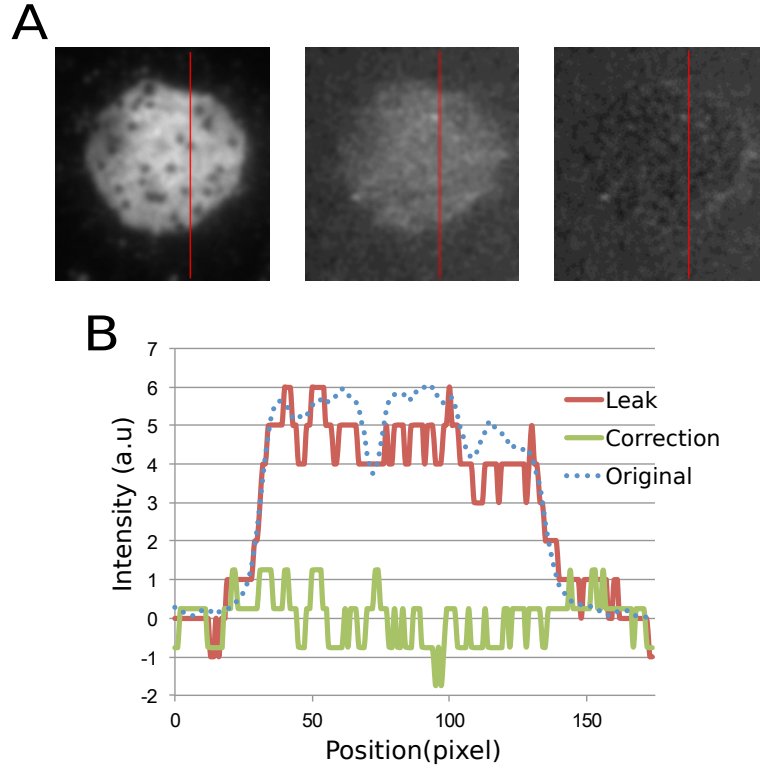
Figure 2.4: Correction of fluorescence leakage.
A. Simultaneous images of PTEN-Halo/Ax2 strain with TMR-ligand were obtained by dual view system. These images were integration of 50 frames (5 s). The left image is the original image obtained with the red channel (for TMR and RFP observation). The center image is the leakage image obtained with the green channel (for GFP observation). The right image is after correction by my method. The intensity on the red line was measured for evaluation. **B.** The intensity profile before and after correction. The red line indicates profile of the leakage image, the green line indicates that of image after correction, and the blue dotted line indicates that of the original image.

2.2.5 Time trajectory analysis

Raw trajectories were extracted from TIRF images as described above. Auto-correlation function of $F(t)$ and cross-correlation function of $F_1(t)$ and $F_2(t)$ were defined as:

$$ACF(t) = \frac{\sum_{k=0}^{n}(F(k) - \mu)(F(k + t) - \mu)}{n^2\sigma^2} \tag{2.3}$$

$$CCF(t) = \frac{\sum_{k=0}^{n}(F_1(k) - \mu)(F_2(k + t) - \mu)}{n_1 n_2 \sigma_1 \sigma_2} \tag{2.4}$$

The notation μ and σ^2 indicate the average and variance of $F(t)$, respectively.

To obtain the average trajectories like Fig.3.1H, I calculated the local maximums and minimums of the first derivative of the raw trajectories at the centers of the increasing and decreasing phases, respectively. Next, I extracted short trajectories of 60 s before and after the calculated centers from the raw trajectories. Finally, I aligned the short trajectories at their centers, normalized them by z-scores and calculated the average trajectories. The phase diagrams were drawn from the average trajectories.

2.2.6 Domain size and lifetime analysis

The domain size and duration time were calculated from binarized kymographs. Kymographs were smoothed by a mean filter with a 9-pixel window and binarized to separate the domain and background, then each domain was detected. I defined lifetime as the size of the domain along the time axis and domain size as the average spatial size of the domain in each time step. Maximum domain size and lifetime in each kymograph were plotted as shown in Fig.3.26. Domains smaller than $32°$ or shorter than 30 s were ignored.

2.2.7 Numerical simulations and reaction diffusion model

To reconstruct the spatiotemporal dynamics of the Ras/PIP3 wave patterns, I constructed a combined model of the Ras and PIP3 signaling systems (Fig.3.29). As described in result section, excitability and pattern formation derive from Ras and its regulatory network. The PIP3 signaling system follows Ras, and feedback from PIP3 to Ras maintains Ras excitability. First, I constructed a model of the PIP3 signaling system as described below.

$$\frac{\partial[PIP3]}{\partial t} = R_{PI3K} - R_{PTEN} - \lambda_{PIP3}[PIP3] + D\nabla^2[PIP3] \tag{2.5}$$

$$\frac{\partial[PIP2]}{\partial t} = -R_{PI3K} + R_{PTEN} + \lambda_{PIP3}[PIP3] + D\nabla^2[PIP2] \tag{2.6}$$

$$\overline{[PIP3]} + \overline{[PIP2]} = [PIP]_{total} \tag{2.7}$$

PIP3 is generated from PIP2 phosphorylation by PI3K (R_{PI3K}) and dephosphorylated into PIP2 by PTEN (R_{PTEN}) on the membrane (2.5), (2.6). The PTEN-independent PIP3 degradation rate, λ_{PIP3}, is also introduced because the degradation of PIP3 is observed even in pten null strain [62]. Overline notation indicates average concentration. The sum of PIP3 and PIP2 concentrations was set to be a constant value ($[PIP]_{total}$; Fig.3.4F). PIP3 and PIP2 diffuse on the membrane independently with the diffusion term $D\nabla^2$. As a simplification, I used single diffusion coefficient of molecules on a plasma membrane. The reactions related production and degradation of PIP3 were described as shown below.

$$R_{PI3K} = V_{PI3K} \left[PI3K\right] \frac{[PIP2]}{K_{PI3K} + [PIP2]} \qquad (2.8)$$

$$R_{PTEN} = V_{PTEN} \left[PTEN\right] \frac{[PIP3]}{K_{PTEN} + [PIP3]} \qquad (2.9)$$

$$[PI3K] = \beta \left[Ras\text{-}GTP\right] \qquad (2.10)$$

The reaction velocities of PIP2 phosphorylation (R_{PI3K}) and PIP3 dephosphorylation (R_{PTEN}) were described as Michaelis-Menten type enzymatic reactions, in which each term is composed with the maximum reaction rate (V_{PI3K}, V_{PTEN}) and Michaelis constant (K_{PI3K}, K_{PTEN}) (2.8), (2.9). Because PI3K shuttles between the cytosol and plasma membrane dependently on Ras-GTP interactions, I introduced Ras-GTP-dependent PI3K membrane translocation and Ras-GTP-dependent PI3K activation (2.10). β indicates the membrane association rate of PI3K, because the membrane translocation of PI3K is proportional to the Ras-GTP level (Fig.3.14F). Membrane localization of PTEN was described as shown below.

$$\frac{\partial \left[PTEN\right]}{\partial t} = -R_{PTEN} + V_{PTEN_{ass}}[PTEN]_{cytosol} \frac{[PIP2]}{K_{PIP2} + [PTEN]}$$
$$\qquad (2.11)$$

$$[PTEN]_{cytosol} = [PTEN]_{total} - \chi\overline{[PTEN]} \qquad (2.12)$$

PTEN also shuttles between the cytosol and plasma membrane and shows mutually exclusive localization pattern with PIP3 (Fig.3.30H). To satisfy these constraints, I introduced PIP3-dependent exclusion of PTEN from the membrane [63][39][131]. We assumed interaction between PTEN and PIP3 results in PTEN dissociation from the membrane and the dissociation has the same rate with PIP3 dephosphorylation, R_{PTEN} (2.11). Additionally, I introduced PTEN recruitment to the membrane by interaction with PIP2 [63] as dependent on the maximum reaction rate $V_{PTEN_{ass}}$ and Michaelis constant K_{PIP2} (2.11). Unlike the case of PI3K, the cytosolic concentration of PTEN drastically changes before and after the membrane translocation [62]. It means there is competitive effect between cytosolic concentration and membrane concentration, so I considered the cytosolic concentration of

PTEN ($[PTEN]_{cytosol}$). I assumed the cytosolic PTEN concentration is uniform inside the cytosol because of faster diffusion coefficient in cytosol than that on a membrane (2.12). Overline notation indicates average concentration, and χ indicates a constant that transforms the surface concentration on the membrane to a volume concentration in the cytosol. The total concentolatin of PTEN molecules was set to be a constant value ($[PTEN]_{total}$).

Second, I constructed the Ras signaling regulation model as an excitable network. As a template for the excitable network model, I applied the theoretical model of self-organization on the membrane reported previously [39][131], which can reconstruct well the excitable responses of a Ras/PIP3 signaling system with minimum elements. In this model, I introduced a positive regulator and negative regulator of Ras as GEFs and GAPs, respectively. The reactions of Ras activation R_{GEFs} and inactivation R_{GAPs} was described as shown below.

$$\frac{\partial \left[Ras\text{-}GDP\right]}{\partial t} = -R_{GEF} + R_{GAP} + k - \lambda_{Ras\text{-}GDP} \left[Ras\text{-}GDP\right] + D\nabla^2 \left[Ras\text{-}GDP\right]$$

(2.13)

$$\frac{\partial \left[Ras\text{-}GTP\right]}{\partial t} = R_{GEF} - R_{GAP} - \lambda_{Ras\text{-}GTP} \left[Ras\text{-}GTP\right] + D\nabla^2 \left[Ras\text{-}GTP\right]$$

(2.14)

$$R_{GEF} = \left(V_{GEFs} + V_{Feedback} \frac{[PIP3]}{K_{PIP3} + [PIP3]}\right) \frac{[Ras\text{-}GDP]}{K_{GEFs} + [Ras\text{-}GDP]}$$

(2.15)

$$R_{GAP} = V_{GAPs} [GAPs] \frac{[Ras\text{-}GTP]}{K_{GAPs} + [Ras\text{-}GTP]}$$

(2.16)

I assumed Ras-GDP to be supplied and degraded at rate k and $\lambda_{Ras\text{-}GDP}$, respectively (2.13). I assumed Ras-GTP to be degraded at rate $\lambda_{Ras\text{-}GTP}$ and supplied only by the GTP exchange reaction of Ras-GDP (2.14). R_{GEFs} was described as a Michaelis-Menten type enzymatic reaction composed of two terms (2.15). One term defines the basal activity of Ras and the other defines feedback from PIP3. Each term was assumed to be composed of the maximum reaction rate (V_{GEFs}, $V_{Feedback} \frac{[PIP3]}{K_{PIP3} + [PIP3]}$ and Michaelis constant K_{GEFs}. This formulation was based on the experimental observation that PIP3 production influences the formation of Ras waves (Fig.3.24). R_{GAPs} was described as an enzymatic reaction with maximum reaction rate V_{GAPs} and Michaelis constant K_{GAPs} (2.16). In order to promote the formation of a Ras-GTP localization patch, I introduced positive regulation from Ras-GDP and negative regulation from Ras-GTP on the recruitment of GAPs to the membrane.

$$\frac{\partial \left[GAPs\right]}{\partial t} = V_{GAPs_{ass}}[GAPs]_{cytosol} \frac{[Ras\text{-}GDP]}{K_{Ras\text{-}GDP} + [Ras\text{-}GDP]} \frac{K_\alpha + \alpha [Ras\text{-}GTP]}{K_\alpha + [Ras\text{-}GTP]}$$
$$- \lambda_{GAPs} [GAPs] + D\nabla^2 [GAPs]$$

(2.17)

$$[GAPs]_{cytosol} = [GAPs]_{total} - \chi \overline{[GAPs]} \qquad (2.18)$$

These regulations were composed of two positive-feedback loops and result in a mutually exclusive relationship between Ras-GTP and GAPs, which could stabilize spatially restricted Ras-GTP localization patches. I assumed positive regulation from Ras-GDP to be a Michaelis-Menten type enzymatic reaction composed of a maximum reaction rate ($V_{GAPs_{ass}}$ and Michaelis constant ($K_{Ras-GDP}$), and negative regulation to be ($\frac{K_\alpha + \alpha[Ras\text{-}GTP]}{K_\alpha + [Ras\text{-}GTP]}$), which I followed the previous PIP3 wave model [39]. Additionally, I assumed the degradation rate of GAPs to λ_{GAPs} and the cytosolic concentration as described in equation (2.17). These assumptions are necessary for excitable dynamics of Ras signaling in the model, however, it can be explained by another excitable model as well.

Detailed methods for the numerical simulations are described previously [131]. I evaluated a one-dimensional system with 100 grids along the membrane to reconstruct the results of the kymographs. The radius of the cells was chosen to be 5 μm with a constant time step Δt = 0.005. For the stochastic simulation, I used the τ-leap method. The spatiotemporal dynamics are described by the reaction diffusion equation described above.

The parameters are summarized in Table.2.6, 2.7. First, I set the parameters related to the PIP3 signaling pathway. We performed a simulation in which the concentration term $[Ras\text{-}GTP]$ was fixed to the value from the experiments, and adjusted the parameters to satisfy the relationships between PIP3, PI3K and PTEN to the experimental results shown in Fig.3.30. Next, I set the parameters related to the Ras wave pattern formation in the condition without feedback from PIP3 by a simulation in which the feedback term $V_{Feedback}$ was fixed to zero. Finally, I modulated $V_{Feedback}$ and V_{GEFs} to satisfy the experimental results. The initial condition is uniform and the initial condition values are summarized in Table.2.6, 2.7. It takes about 3 to 5 min that the system comes to show wave pattern. In the case of deterministic simulation, I used final values of stochastic simulation as an initial condition.

Kymographs were generated from the simulations based on this model and parameters. The parameter value of PI3K activity, V_{PI3K}, was modulated during the simulation. Then, I set the value of V_{PI3K} to 0 s^{-1} (PI3K off) or 12 s^{-1} (PI3K ON) in the PI3K on/off simulation shown in Fig.3.33. The value of Ras basal activity, V_{GEFs}, was also changed in each simulation. We varied the values of V_{GEFs} from 400 to 570 s^{-1} in 10 increments and analyzed all kymographs to obtain distributions of the domain size and duration time.

Table 2.6: Parameter List 1

Parameters	Description	Values
V_{PTEN}	Dephosphorylation rate of PIP3 by PTEN	3 s^{-1}
K_{PTEN}	Michaelis constant of PTEN dephosphorylation reaction	500 μm^{-2}
V_{PI3K}	Phosphorylation rate of PIP2 by PI3K	12 s^{-1}
K_{PI3K}	Michaelis constant of PI3K phosphorylation reaction	300 μm^{-2}
$V_{PTEN_{ass}}$	PTEN association reaction rate by PIP2	5000 $\cdot\mu$M$^{-1} \cdot \mu$m$^{-2}\cdot$s^{-1}
K_{PIP2}	Michaelis constant of PTEN association reaction	2000 μm^{-2}
λ_{PIP3}	PTEN-independent PIP3 degradation rate	0.2 s^{-1}
β	Parameter indicates magnitude of PI3K activation by Ras	0.01
PTEN$_{total}$	Total concentration of PTEN	0.1 μM
PIP$_{total}$	Density of PIPs on plasma membrane	5000 $\cdot\mu$m^{-2}
V_{GAPs}	Deactivation rate of Ras by GAPs	16 s^{-1}
K_{GAPs}	Michaelis constant of GAPs deactivation reaction	40 μm^{-2}
V_{GEFs}	Activation rate of Ras by GEFs	400-600 s^{-1}
K_{GEFs}	Michaelis constant of GEFs activation reaction	3500 $\cdot\mu$m^{-2}
$V_{feedback}$	Reaction rate of PIP3 feedback regulation	25 s^{-1}
K_{PIP3}	Michaelis constant of PIP3 feedback regulation	0.1 $\cdot\mu$m^{-2}

Table 2.7: Parameter List 2

Parameters	Description	Values
$\lambda_{Ras\text{-}GTP}$	Degradation rate of GAPs	0.2 s^{-1}
$\lambda_{Ras\text{-}GDP}$	Dissociation rate of GDP	0.003 s^{-1}
k	Association rate of Ras-GDP	$45 \cdot \mu$m$^{-2}\cdot$s^{-1}
$V_{GAPs_a ss}$	Association rate of GAPs by Ras-GDP	$1300 \cdot \mu$M$^{-1} \cdot \mu$m$^{-2}\cdot$s^{-1}
$K_{Ras\text{-}GDP}$	Michaelis constant of GAPs association reaction	3000 μm^{-2}
λ_{GAPs}	Dissociation rate of GAPs	1.2 s^{-1}
K$_\alpha$	Half-maximum concentration for negative regulation of GAPs	$120 \cdot \mu$m^{-2}
α	Parameter indicates magnitude of negative regulation of GAPs	0.001
GAPs$_{total}$	Total concentration of PTEN	0.1 μM
R	Cell radius	5 μm
D	Diffusion coefficient of molecules on plasma membrane	0.2 μm$^{-2}\cdot$s^{-1}
χ	A constant to transform surface concentration to volume concentration	$0.001 \cdot \mu$M$\cdot\mu$m^{-2}
$[PIP3]_{initial}$	Initial value of $[PIP3]$	0 μm$^{-2}\cdot$s^{-1}
$[PIP2]_{initial}$	Initial value of $[PIP2]$	5000 μm$^{-2}\cdot$s^{-1}
$[PTEN]_{initial}$	Initial value of $[PTEN]$	0 μm$^{-2}\cdot$s^{-1}
$[Ras\text{-}GTP]_{initial}$	Initial value of $[Ras\text{-}GTP]$	1000 μm$^{-2}\cdot$s^{-1}
$[Ras\text{-}GDP]_{initial}$	Initial value of $[Ras\text{-}GDP]$	1000 μm$^{-2}\cdot$s^{-1}
$[GAPs]_{initial}$	Initial value of $[GAPs]$	0 μm$^{-2}\cdot$s^{-1}

2.2.8 Single molecule imaging

Single-molecule imaging and analysis were performed as described below [153][155][55][59][156][70]. Sample preparation is described in TIRF imaging section. To detect fluorescent signal from diffusing single-molecule, I observed it with higher laser power (561 nm laser 1 mW) and shorter exposure time (16.6 or 33.3 msec). From TIRF images, I obtained a time series data set of a center coordinates of single-molecules [152]. The center coordinates were calculated by 2D Gaussian fitting of a single-molecule spot. I excluded spots which have clearly larger size than usual single-molecule spots. At the same time, I observed membrane localization of PIP3 and classified single-molecule spots as inside or outside of the PIP3 accumulation area. We defined the threshold of inside of pattern as 10% of maximum fluorescence intensity of $PHD_{AKT/PKB}$-GFP.

Next, I analyzed diffusion speed and membrane binding lifetime of each spot on a cell membrane. Diffusion constant was obtained by fitting of distribution of displacement length of the spots. From the dataset, I calculated displacement length of each spot between each time step and plot the distribution. I performed maximum likelihood estimation to obtaine the number of states, the propotions and diffusion coefficients of each states.

$$P_i\left(\Delta r\right) = \sum_{j=1}^{i} p_j \frac{\Delta r}{2D_j\Delta t + 2\varepsilon^2} e^{-\frac{\Delta r^2}{4D_j\Delta t+4\varepsilon^2}} \tag{2.19}$$

$P_i\left(\Delta r\right)$ indicates probability density of the dispracement length (Δr) at the time window (Δt). The subscript (i) indicates the number of diffusion states. D_i and p_i indicate the diffusion coefficient and the propotions of ith diffusion state, respectively. I used AIC (Akaike Information criterion) to choose the suitable number of diffusion states. AIC was calculated from below equation.

$$AIC_i = -2\sum_{m=1}^{n} \log P_i\left(\Delta r_m\right) + 2k_i \tag{2.20}$$

n is the number of samples in the dataset. k_i is the number of free parameters that presents a penalty for the number of states. ε is measurement error estimated from MSD (mean square displacement) with below equation.

$$MSD = \langle\Delta r^2\rangle \approx 4D\Delta t + 4\varepsilon^2 \tag{2.21}$$

Membrane binding lifetimes ($R\left(t\right)$) were obtained by fitting of dissociation curve with single state dissociation model with dissociation rate λ.

$$R\left(t\right) = e^{-\lambda t} \tag{2.22}$$

Chapter 3

Result

3.1   TIRF observation of PIP3 wave

It was reported that PIP3 exhibits relaxation oscillatory spatial-temporal pattern on a cell membrane [39][131]. *Dictyostelium discoideum* cells were starved 3 to 4 hours in DB buffer. Starved cells were treated with 5μM Latrunculin A and 4 mM caffeine. In this condition, each cell has no polarity in its shape and cytoskeleton, and there is no external stimulus and bias in an environment. Then, cells show a characteristic localization pattern of PIP3 that looks like crescent patches when observed by confocal microscope (Fig.3.1A). These patches move on a cell periphery like a relaxation oscillatory wave, and we call it as self-organized traveling wave or "PIP3 wave".

PIP3 waves were analyzed by the kymograph method (Fig.3.1C and E). From the kymograph, a time trajectory was obtained that showed the temporal evolution of the wave pattern (Fig.3.1F). However, because the signal to noise ratio is not enough to analyze the trajectory directory, it is necessary to sum up adjacent pixels, that traded off the spatial resolution. In the fact, spatial length of ROI on the kymograph is about 2μm although the slope length of spatial pattern along a cell periphery is less than 1μm. Besides, it is necessary to consider about the effect of the depth of confocal volume (about 0.5 to 1μm). Spatial overlap can cause miss understanding of temporal relationship. To evaluate temporal pattern without the effect of spatial pattern, it is necessary to enhance signal to noise ratio and spatial resolution in the same temporal resolution.
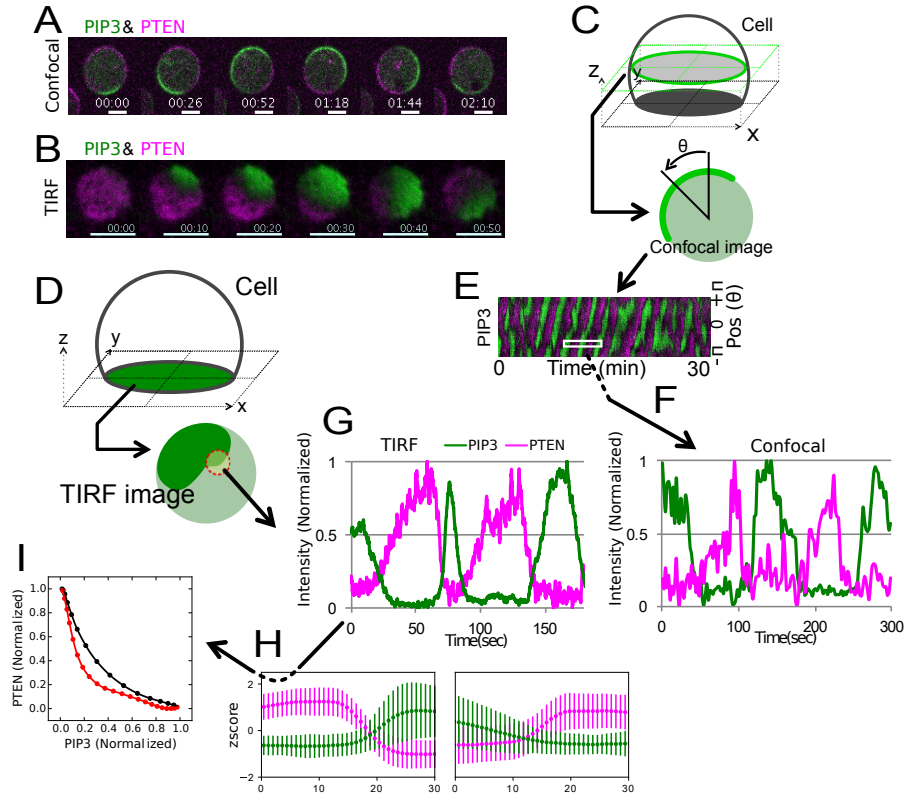
Figure 3.1: Difference between confocal and TIRF.
A, B, Time-lapse imaging of PIP3 and PTEN in a WT cell expressing
$\text{PHD}_{\text{AKT/PKB}}$-GFP and PTEN-Halo-TMR taken by confocal microscopy (A) and
TIRF microscopy (B). Scale bars in the images represent 5 μm. The time format
is "mm:ss". **C, D,** Scheme of confocal imaging and kymograph analysis (C)
and TIRF imaging and trajectory analysis (D). **E,** Kymograph showing PIP3 and
PTEN wave pattern. **F, G** Time trajectory of the PIP3 wave pattern from confocal
(F) and TIRF (G). **H,** Average trajectories of the increase phase (left) and decrease
phase (right). Data are the mean $\pm$ s.d. of the z-scores of intensity from 22 cells.
I, Phase diagrams of PIP3 and PTEN based on the average trajectories shown in
(H). The black line indicates the increase phase along the horizontal axis and the
red line indicates the decrease phase.

Then, I introduced TIRFM to improve the signal to noise ratio. As shown in Fig.3.1F, a focal plane of TIRFM is bottom of the cell, and illumination depth is less than 200 nm from grass surface. It enables selective excitation of fluorophore on a cell membrane and reduced cytosolic background. It equipped low noise EMCCD cameras that is usually applied for live cell single-molecule imaging. These gimmicks enhanced signal to noise ratio of images. By using this system, I obtained more detailed about the localization pattern of PIP3 and PTEN simultaneously (Fig.3.1E). From the images, I obtained the time trajectory like Fig.3.1G with a ROI as a circle with 0.2μm radius. This indicates this method achieved both of higher signal to noise ratio and spatial resolution. I analyzed average dynamics of PIP3 and PTEN from the trajectories of 6 cells (Fig.3.1H), and obtained phase-diagram (Fig.3.1I). PIP3 and PTEN exhibit mutual exclusive and relaxation oscillation pattern, that is consistent with confocal study.

3.1.1   Observation of PIP2

TIRF simultaneous observation method was applied for imaging of PIP2 and PIP3. While PIP3 is visualized by $PHD_{AKT/PKB}$, imaging of PIP2 was difficult in *Dictyostelium discoideum* cells because there is a suitable probe for PIP2 imaging in *Dictyostelium* cells. First, I tried to use $PHD_{PLC\delta1}$ that is well known PIP2 probe used in mammalian cells [48][49]. I observed $PHD_{PLC\delta1}$-GFP by confocal microscopy with PIP3 wave ($PHD_{AKT/PKB}$-RFP), but no signal change was observed about $PHD_{PLC\delta1}$-GFP (Fig.3.2A). Next, I observed them by TIRF microscopy and found the contrary localization change of PIP2 with PIP3 (Fig.3.2B). However, the signal was weak and difficult to analyze the relationship in detail (Fig.3.2C-E).

In order to improve the imaging quality, I introduced another PIP2 probe, Nodulin [61][53]. In contrast with $PHD_{PLC\delta1}$, contrary localization was observed with GFP-Nodulin even by confocal microscopy (Fig.3.3A). Nodulin is observed suitable for reporting PIP2 dynamics in *Dictyostelium* cells. However, observation of PIP2 wave was still difficult because of the shallow range of signal fluctuation (Fig.3.3B and C).

Then, GFP-Nodulin was observed by TIRF microscopy (Fig.3.4A). As shown in Fig.3.4B, GFP-Nodulin exhibited clear negative correlative localization pattern with PIP3 wave. Cross-correlation function shown in Fig.3.4D, average trajectory shown in Fig.3.4E and Phase-diagram of PIP2 and PIP3 shown in Fig.3.4F indicate PIP3 level correlates with negative values of PIP2 level. PIP2 and PIP3 didn't exhibit mutual exclusive patterns, that is different from the relationship between PIP3 and PTEN. In a previous study, it was hypothesized that inflow of PIP2 and outflow of PIP3 are the motive force of excitable oscillation of the PIP3 wave [39][131]. However, simultaneous imaging of PIP2 and PIP3 revealed trajectory of increasing phase and decreasing phase is in almost same orbit. This means the total amount of PIP2 and PIP3 are almost constant during wave evolution,
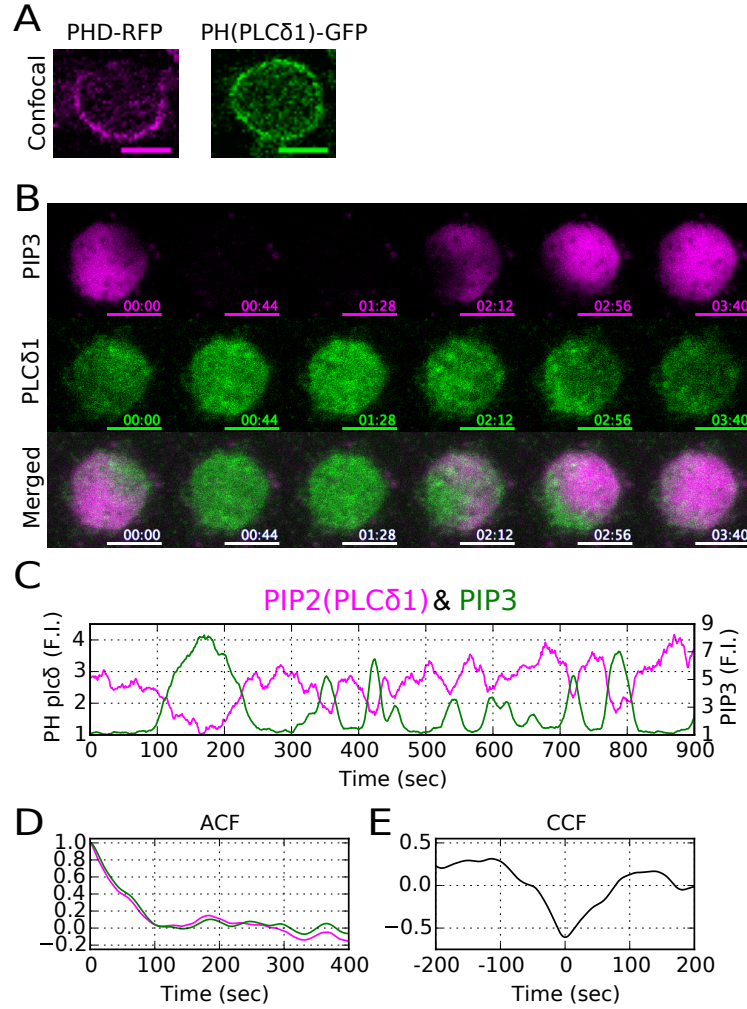
Figure 3.2: TIRF image of PHD$_{\text{PLC}\delta 1}$-GFP.
A, Confocal images of PHD$_{\text{AKT/PKB}}$-RFP and PHD(Plcd1)-GFP. Scale bars in the images represent 5 μm. **B,** Simultaneous time-lapse TIRFM imaging of PIP3 PHD$_{\text{AKT/PKB}}$-RFP and PHD(Plcd1)-GFP. **C,** Typical time trajectory. **D, E,** Auto- and cross-correlation functions of the trajectory.
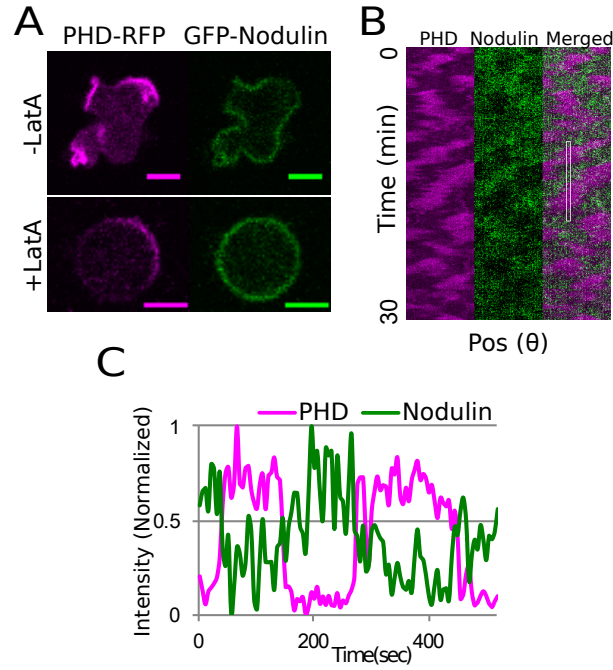
Figure 3.3: Confocal imaging of GFP-Nodulin.
A, Confocal images of $PHD_{AKT/PKB}$-RFP and GFP-Nodulin before and after treatment with Latrunculin A. Scale bars in the images represent 5 μm. **B,** Kymograph of time-lapse imaging. **C,** Time trajectory of $PHD_{AKT/PKB}$-RFP and GFP-Nodulin in the ROI shown in the kymograph (B).

that cannot explain the motive force in the model. This suggests another motive force is necessary to explain the wave pattern.
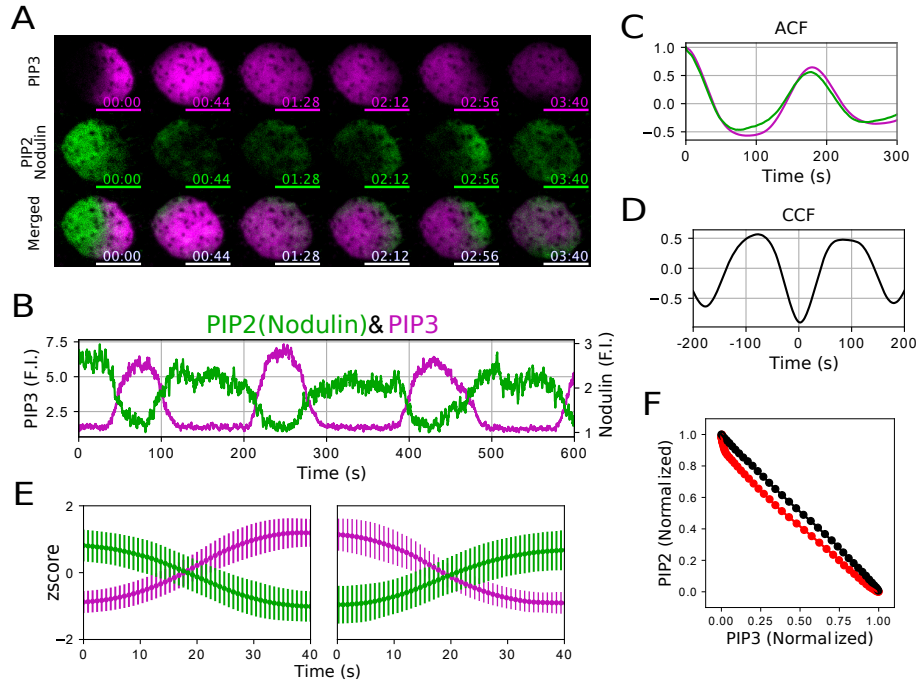
Figure 3.4: Imaging of GFP-Nodulin.
A, Simultaneous time-lapse TIRFM imaging of $PHD_{AKT/PKB}$-RFP and GFP-Nodulin. Scale bars in the images represent 5 μm. **B,** Typical time trajectory. **C, D,** Auto- and cross-correlation functions of the trajectory. **E,** Average trajectories of the increase phase (left) and decrease phase (right). Data are the mean $\pm$ s.d. of the z-scores of intensity from 26 cells. **F,** Phase diagrams of PIP3 and PIP2 based on the average trajectories shown in (E). The black line indicates the increase phase along the horizontal axis and the red line indicates the decrease phase.

3.1.2 Observation of hPTEN

As one of the candidates of motive force, next, I focused on PTEN. As shown in Fig 3.1, PTEN exhibits characteristic mutual exclusive localization pattern with PIP3. It was reported that human PTEN (hPTEN) rescued the phenotype of *pten* null mutant in part even though hPTEN looks no localization on a cell membrane [143][71]. In order to clarify whether hPTEN really does not exhibit membrane localization, I performed TIRF observation of hPTEN with PIP3 wave. As a result, hPTEN-Halo localized on a membrane, but didn't exhibit a wave pattern like *Dictyostelium* PTEN (Fig.3.5A and B). The auto-correlation function of hPTEN has no peak, though that of PIP3 has peak around 40 to 50 sec (Fig.3.5C). These results indicate that the localization pattern of PTEN is not necessary for PIP3 wave.
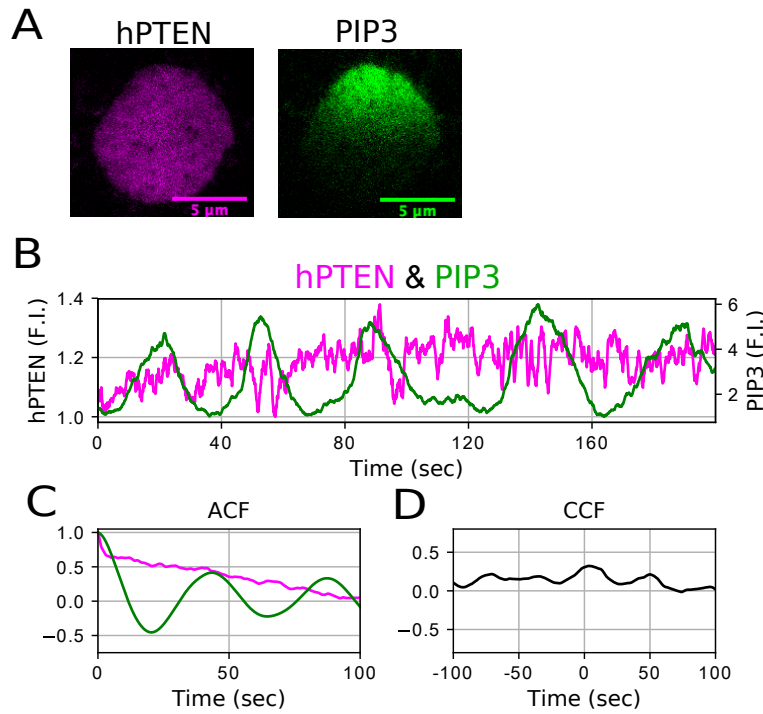
Figure 3.5: Imaging of hPTEN.
A, TIRF images of hPTEN and PIP3 in *pten* null cells expressing hPTEN-Halo-TMR and PHD$_{\text{AKT/PKB}}$-GFP. **B,** Typical time trajectory. **C, D,** Auto- and cross-correlation functions of the trajectory.

3.2 Analysis of PI3K on a cell membrane

3.2.1 TIRF imaging of PI3K

Next, I applied TIRF observation for PI3K as a candidate of motive force for pattern formation. No membrane localization of PI3K was reported under condition with Latrunculin A in spite of the localization pattern of PIP3. However, observation by confocal microscope cannot detect the membrane localization of low membrane to cytosolic ratio because of overlap between membrane and cytosol. To confirm this point, I performed simultaneous observations of PI3K2-Halo-TMR and $PHD_{AKT/PKB}$-GFP by using TIRFM. I succeeded in observation of membrane localization of PI3K on a cell membrane and found PI3K exhibits closely coupled localization pattern with PIP3 wave (Fig.3.6A). This result suggests PI3K can take a role of the motive force of PIP3 pattern formation.

To clarify the relationship between PIP3 wave and PI3K localization pattern, I performed a quantitative analysis of the spatiotemporal dynamics between them. As as result, PIP3 wave propagation was slightly delayed compared with the PI3K localization pattern (Fig.3.6B). This delay was also detected in the cross-correlation analysis (Fig.3.6D). The peak time having a positive value means that PIP3 follows PI3K. I calculated the average dynamics of both PIP3 and PI3K from 126 individual trajectories in a ROI from 21 cells (Fig.3.6E). and obtained the phase diagram of PIP3-PI3K that looks an ellipse-like trace (Fig.3.6F). These results indicate the localization pattern of PI3K precedes that of PIP3.

As reported before, PI3K exhibits F-actin dependent localization, and does not exhibit significant membrane localization after treatment of 5 μM Latrunculin A. I observed the dynamics of F-actin by actin binding protein, $LimE_{\Delta coil}$ under this condition. As shown in Fig.3.7A, F-actin didn't exhibit any localization pattern. This means the localization pattern of PI3K under this condition is F-actin independent. I examined the domain dependency of membrane localization of PI3K by using N-PI3K and C-PI3K (N-terminal and C-terminal part of PI3K2). As shown in Fig.3.7B and C, both of N-PI3K and C-PI3K didn't exhibit the localization pattern. N-terminal region of PI3K is known as targeting domain that mediates F-action dependent localization of PI3K. C-terminal region is a homologue of human PI3K γ that include catalytic domain, accessory domain, C2 domain and Ras binding domain(RBD). Then, I performed the same experiment with PI3K(KE) ($PI3K2^{K857,858E}$) that has catalytic activity, but cannot interact with Ras-GTP because of mutations in its RBD [74]. This mutant also exhibit no localization pattern (Fig.3.7D). Time-lapse imaging also indicate no localization change of PI3K(KE) at all (Fig.3.8). These results indicate that N-terminal domain and RBD are necessary for the F-actin independent membrane localization pattern of PI3K.
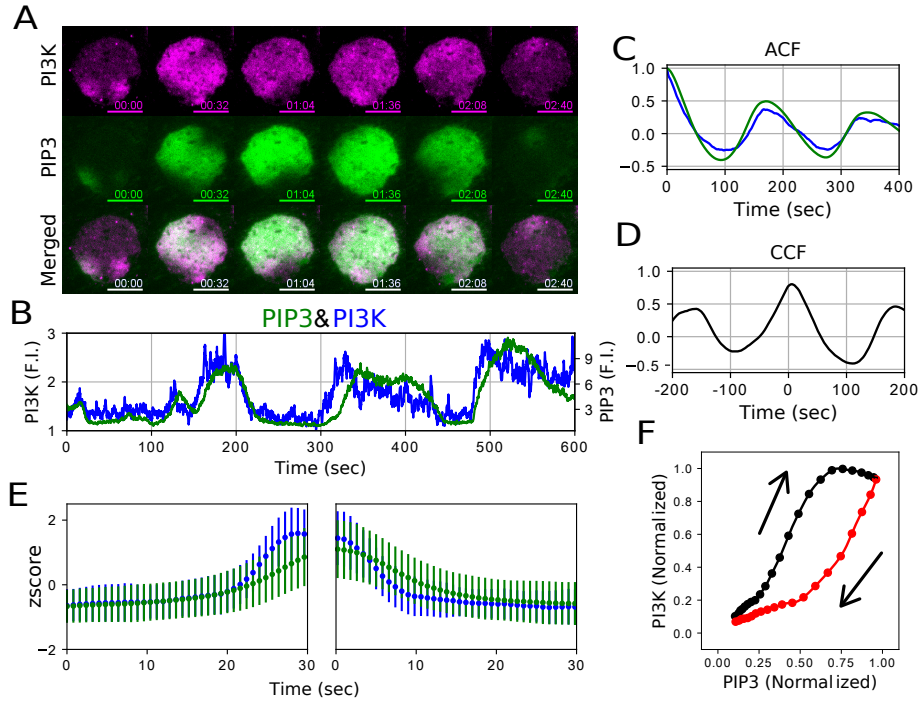
Figure 3.6: Simultaneous imaging of PI3K and PIP3.
A, Simultaneous time-lapse TIRFM imaging of PI3K2-Halo-TMR and PHD$_{\mathrm{AKT/PKB}}$-GFP. Scale bars in the images represent 5 μm. **B,** Typical time trajectory. **C, D,** Auto- and cross-correlation functions of the trajectory. **E,** Average trajectories of the increase phase (left) and decrease phase (right). Data are the mean $\pm$ s.d. of the z-scores of intensity from 21 cells. **F,** Phase diagrams of PIP3 and PI3K based on the average trajectories shown in (E).
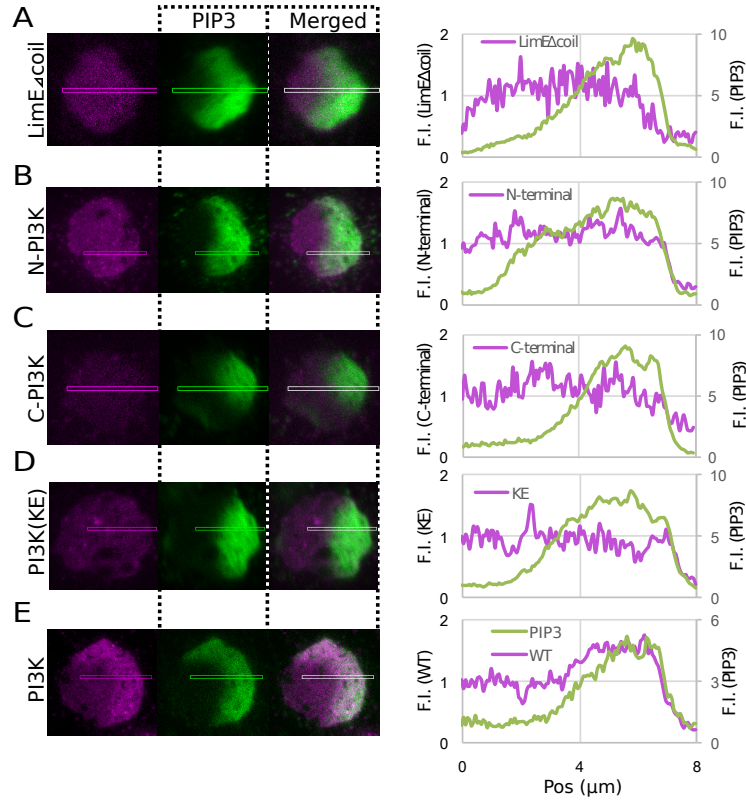
Figure 3.7: TIRF imaging of membrane localization of PI3K truncates and mutant.
A-E Simultaneous imaging of PIP3 (PHD$_{AKT/PKB}$-GFP) and F-actin reporter LimE$_{\Delta coil}$-RFP (A), N-PI3K2-Halo-TMR (B), C-PI3K2-Halo-TMR (C), PI3K2^{K857,858E}-Halo-TMR (D) or PI3K2-Halo-TMR (E) expressed in Ax2 strain taken with TIRF microscope. Left graphs show line profile of the rectangles shown in the images. Horizontal axis correspond to the long side of the rectangle. Vertical axis indicate the magnitude of fluorescent intensity based on the average intensity of outside of the PIP3-enriched domain.
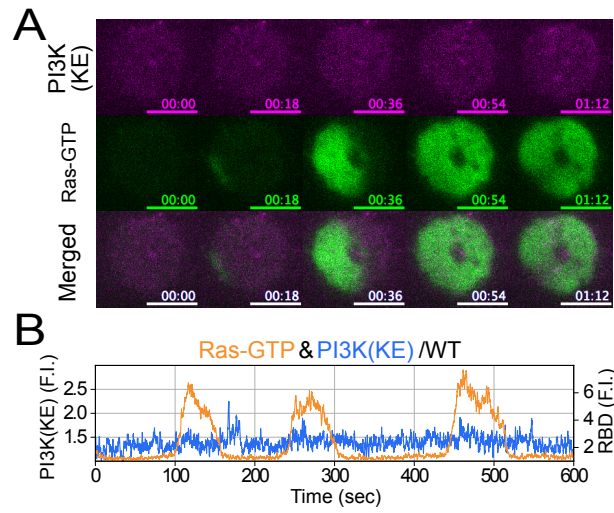
Figure 3.8: Simultaneous imaging of PI3K(KE) and PIP3.
A, Simultaneous time-lapse imaging of Ras-GTP (RBD$_{\text{Raf1}}$-GFP) and
PI3K2$^{\text{K857,858E}}$-Halo-TMR. Scale bars in the images represent 5 μm and time
format is "mm:ss". **B,** Typical examples of time trajectories of PI3K(KE) (blue)
and Ras-GTP (orange) from TIRF simultaneous imaging. Vertical axis F.I.
indicates magnitude of fluorescent intensity divided by the minimum value of each
trajectory.

3.2.2 Single-molecule imaging of PI3K

To examine the detail of membrane binding of PI3K, I used single-molecule imaging technique and measured membrane binding lifetime. Single-molecule imaging was performed by TIRF microscopy. PI3K2-Halo expressed cells were treated with 1 to 10 nM Halo-tag TMR-ligand for 30 min. After that I washed cells with 1 ml DB 10 times to reduce non-specific binding of TMR-ligand, and observed them. As a result, I obtained light spot from single-molecule fluorophore with 16.3 msec exposure (Fig.3.9A). The position of each molecule was calculated by 2D Gaussian fitting of the light spot. By repeating for each frame, I tracked association, diffusion and dissociation of each molecule. From the time from association to dissociation of each trajectory, dissociation curve of membrane binding of PI3K was obtained (Fig.3.9B), that reveals about 70 msec lifetime of membrane binding. From the displacement length of each step of the trajectories, probability density of displacement length of PI3K was obtained (Fig.3.9C), that indicates there are two peaks at shorter (0.05μm) and longer (0.2μm) displacement, means PI3K has not less than two diffusion states. Then, I calculated AIC (Akaike Information Criterion) value from the likelihood of fitting by 1 to 5 states models, and found 4 states model is probable to explain the diffusion profile (Fig.3.9D). The parameters, diffusion constant and rate of subpopulations were shown in Fig.3.9E. There are two fast diffusion states and two slow diffusion states. Population of slower diffusion states is about 40%.

Next, I observed single-molecule of PI3K2-Halo-TMR and PIP3 wave simultaneously (Fig.3.10C). Each molecule was categorized inside or outside of the PIP3-enriched domain (PIP3 domain) as "active" or "inactive", respectively. In PIP3 domain, PI3K is expected to be activated and has high catalytic activity. A membrane binding lifetime of WT PI3K in the active site (0.100 ± 0.020 s) is prolonged twice as that in inactive site (0.055 ± 0.003 s) (Fig.3.10A and D), that is appropriate to localization analysis of PI3K and PIP3 (Fig.3.6A). At the same time, probability density of the displacement length in the active site is shorter and looks single peak (Fig.3.10B). The population of slower diffusion states is about 72% (Fig.3.10E). A membrane binding lifetime in inactive site became shorter and population of slower diffusion states is 32.4%. These results indicate that membrane binding stability varies depending on the difference of membrane fractions. This trend was not changed even in motile cells (Fig.3.11), suggesting that the behavior of PI3K is independent of F-actin on a cell membrane.
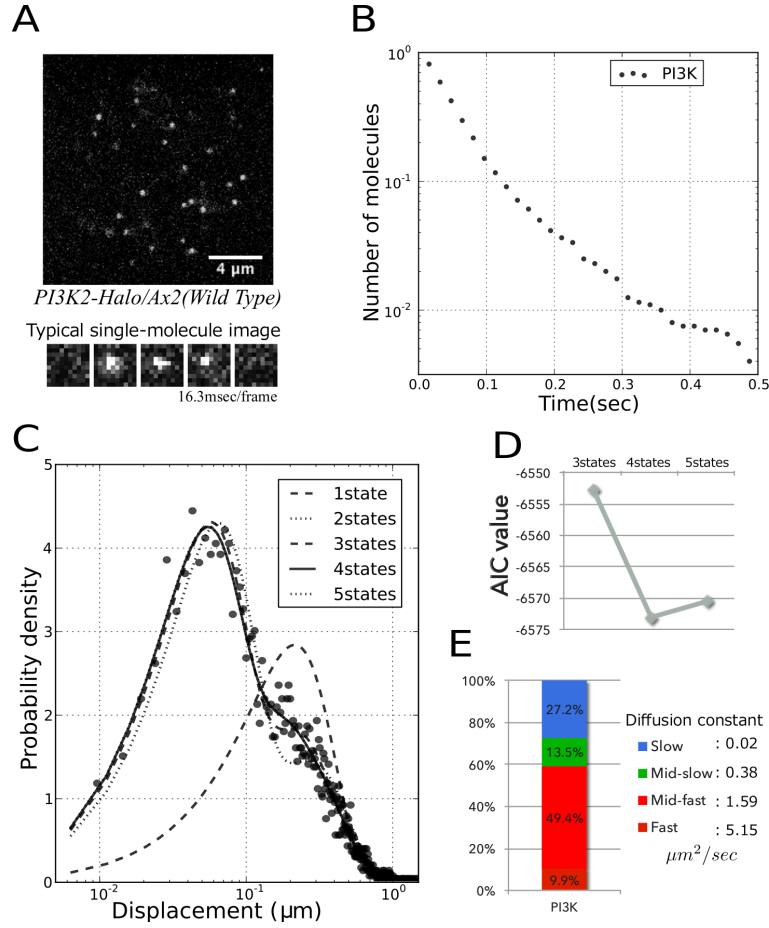
Figure 3.9: Single-molecule imaging of PI3K.
A, Single-molecule image of PI3K2-Halo-TMR taken by TIRF-microscope in 16.3 msec exposure time. **B,** Dissociation curve analysis of membrane binding of PI3K. It reveals about 70 msec lifetime of membrane binding. **C,** Diffusion distribution of PI3K. There are two peaks at short (0.05 μm) and long (0.2 μm) displacement. **D,** AIC (Akaike Information Criterion) analysis indicates 4 states model is probable to explain the diffusion profile. **E,** Rate of subpopulations of diffusion states from fitting of 4 states model.
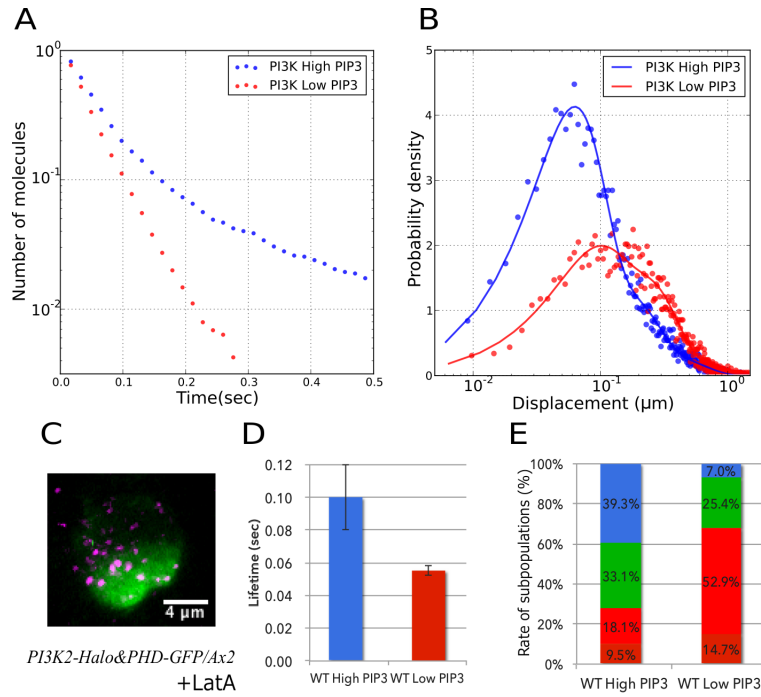
Figure 3.10: Stabilization of PI3K binding on PIP3-enriched domain.
A, B, Dissociation curve (A) and diffusion distribution (B) of PI3K, which are compared between inside and outside of PIP3 domain.**C,** Simultaneous imaging of PI3K single-molecule and PIP3 bulk localization. **D,** Comparison of binding lifetime. Data are the mean $\pm$ s.d. **E,** Comparison of rate of subpopulations of dissociation states. Diffusion constants are shown in Fig.3.9E.
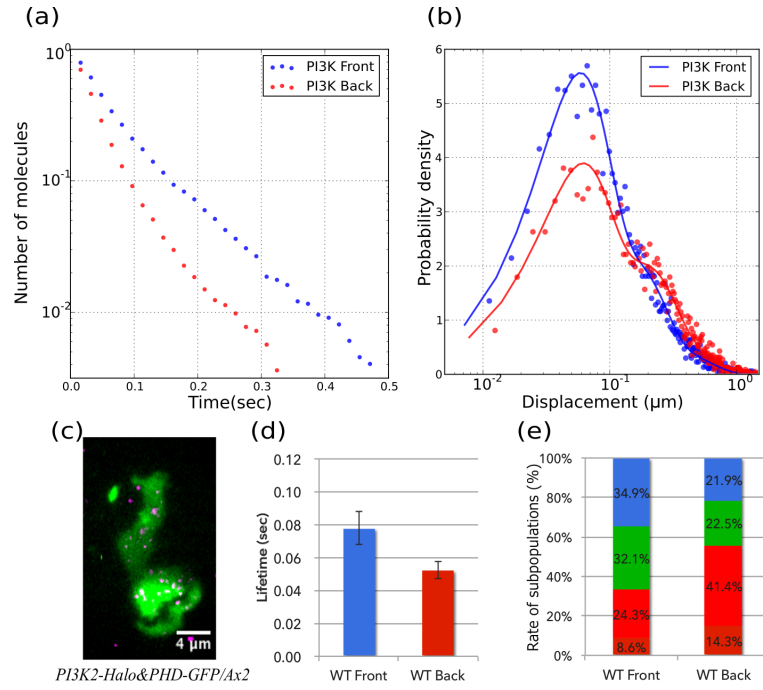
Figure 3.11: Single-molecule of PI3K in motile cells.
A, B, Dissociation curve (A) and diffusion distribution (B) of PI3K, which are compared between inside and outside of PIP3 domain.**C,** Simultaneous imaging of PI3K single-molecule and PIP3 bulk localization in a motile cell. **D,** Comparison of binding lifetime. Data are the mean $\pm$ s.d. **E,** Comparison of rate of subpopulations of dissociation states. Diffusion constants are shown in Fig.3.9E.

To clarify the difference between WT PI3K, N-PI3K, C-PI3K and PI3K(KE), I applied single-molecule analysis to PI3K mutant and truncates. All of them exhibits longer membrane binding lifetime in active site, but the magnitude of the difference was much smaller than that of WT PI3K. PI3K(KE) exhibits almost same membrane binding lifetime in inactive site (0.06 ± 0.002 s) as that of WT PI3K but the increment of a membrane binding lifetime in the active site (0.07 ± 0.005 s) is a 75% reduction compared with WT (Fig.3.12A and D). This result suggests the increment of membrane binding lifetime in active site depends on interaction of Ras-GTP via RBD.

On the other hand, C-PI3K also shows shorter membrane binding lifetime in the active site (0.05 ± 0.003 s; Fig.3.12B and E), even though C-PI3K has active RBD. C-PI3K has the shortest membrane binding lifetime in inactive site (0.04 ± 0.001 s), suggesting that the N-terminal domain is necessary for stable membrane binding of PI3K. Unexpectedly, N-PI3K also exhibits prolonged membrane binding lifetime in the active site (0.07 ± 0.011 s), that is almost same as that of PI3K(KE). This indicates that N-terminal domain also responsible for difference of membrane fractions. The same membrane binding lifetime between PI3K(KE) and N-PI3K suggests that N-terminal domain is dominant in the membrane binding lifetime of PI3K(KE) as well as N-PI3K. It is expected that shorter membrane binding lifetime of N-PI3K in inactive site is due to contribution of C-terminal domains. Summarized these results, the N-terminal domain is necessary for stability of pre-binding on a membrane before interaction with Ras-GTP while RBD is necessary for localization pattern of F-actin independent membrane localization of PI3K. N-terminal domain contains the membrane fraction sensitive part that enables different membrane binding lifetime between active and inactive site in F-actin independent manner. I noticed that the increment of a membrane binding lifetime of WT PI3K in the active site is about twice, and the increment of membrane intensity of PI3K in PIP3 wave also 2 to 3 times or so (Fig.3.6B), which were well consistent. These results suggest that PI3K localization pattern can be explained by differences in dissociation rate of PI3K that depends on interaction with Ras-GTP.

3.3 Relationship between Ras and PIP3 waves

3.3.1 Simultaneous imaging of Ras and PIP3 wave

From the result that PI3K localization pattern precedes that of PIP3 and PI3K localization is regulated by its RBD, I confirmed a temporal relationship between Ras wave and PIP3 wave. I observed Ras, PI3K and PIP3 to examine the spatiotemporal relationship during self-organized pattern formation by TIRF microscopy. Simultaneous observations of RBD_{Raf1}-RFP and $PHD_{AKT/PKB}$-GFP revealed that both probes exhibited closely coupled wave propagation on the membrane (Fig.3.13A). Quantitative analysis
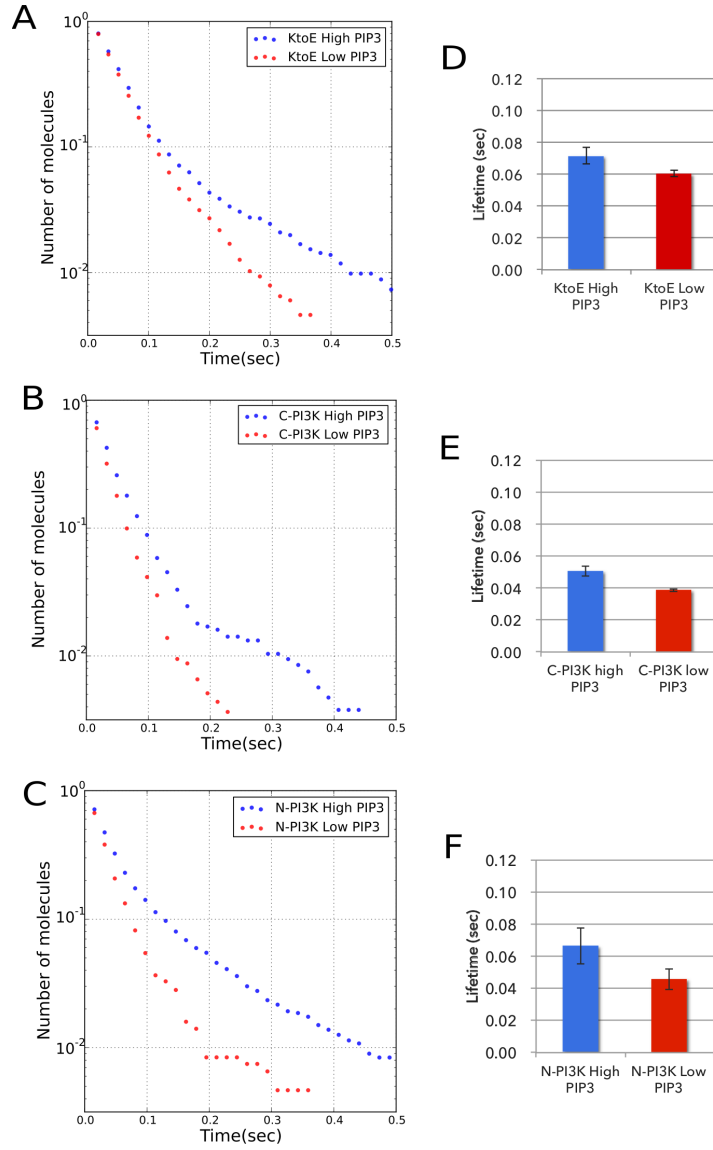
Figure 3.12: Dissociation of PI3K mutant and truncates.
A-C, Dissociation curve analysis of PI3K(KE) (A), C-PI3K (B) and N-PI3K (C).
D-F, Comparison of binding lifetimes. Data are the mean $\pm$ s.d.

of the spatiotemporal dynamics revealed the PIP3 wave propagation was
slightly delayed compared with the Ras wave propagation (Fig.3.13B). A
cross-correlation function of PIP3 dynamics against Ras dynamics had a
positive peak time value, meaning that PIP3 follows Ras-GTP (Fig.3.13D).
I calculated the average dynamics of both Ras-GTP and PIP3 from 90 indi-
vidual trajectories from 15 cells (Fig.3.13E) and obtained the phase diagram
(Fig.3.13F). This diagram shows a characteristic ellipse-like trace which is
consistent with that of PIP3 and PI3K, means Ras-GTP preceding PIP3. I
calculated the peak time of the cross-correlation function in each cell and
obtained the distribution , which showed the lag time of PIP3 against Ras-
GTP was about 0.9 ± 0.6 s on average. That is consistent with that of PIP3
against PI3K (2.3 ± 1.1 s on average; Fig.3.17C). These results indicate PIP3
wave follows Ras wave as well as PI3K.
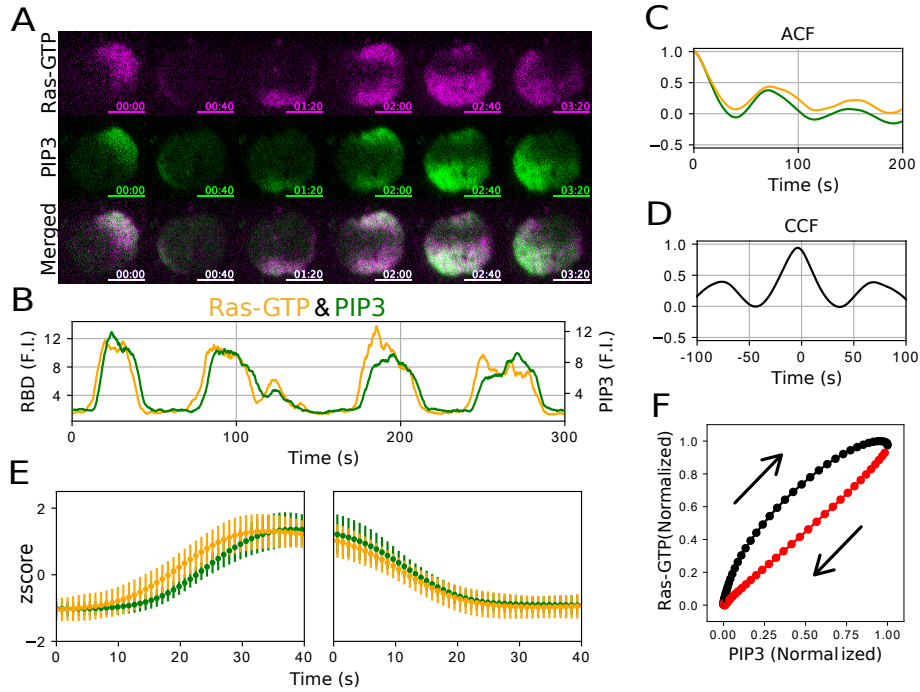
Figure 3.13: Simultaneous imaging of Ras-GTP and PIP3.
A, Simultaneous time-lapse TIRFM imaging of RBD$_{\text{Raf1}}$-RFP and PHD$_{\text{AKT/PKB}}$-
GFP. Scale bars in the images represent 5 μm. **B,** Typical time trajectory. **C, D,**
Auto- and cross-correlation functions of the trajectory. **E,** Average trajectories of
the increase phase (left) and decrease phase (right). Data are the mean $\pm$ s.d. of
the z-scores of intensity from 15 cells. **F,** Phase diagrams of PIP3 and Ras-GTP
based on the average trajectories shown in (E).

Next, I analyzed the spatiotemporal relationship between Ras-GTP and
PI3K in the wave propagation. The oscillatory dynamics of PI3K on the cell

membrane coincided tightly with that of Ras-GTP (Fig.3.14A and B), as revealed in the auto- and cross-correlation functions of the time trajectories (Fig.3.14C and D) and the averaged dynamics of both proteins calculated from 132 individual trajectories from 22 cells (Fig.3.14E). A phase diagram of PI3K/Ras-GTP shows that the amount of PI3K on the membrane was proportional to the amount of Ras-GTP (Fig.3.14F). The peak time of the cross-correlation function was 0.0 ± 0.7 s on average (Fig.3.17B), indicating no delay between the Ras-GTP and PI3K waves. These results clearly indicate that the membrane localization of PI3K is tightly regulated by Ras-GTP during wave propagation.
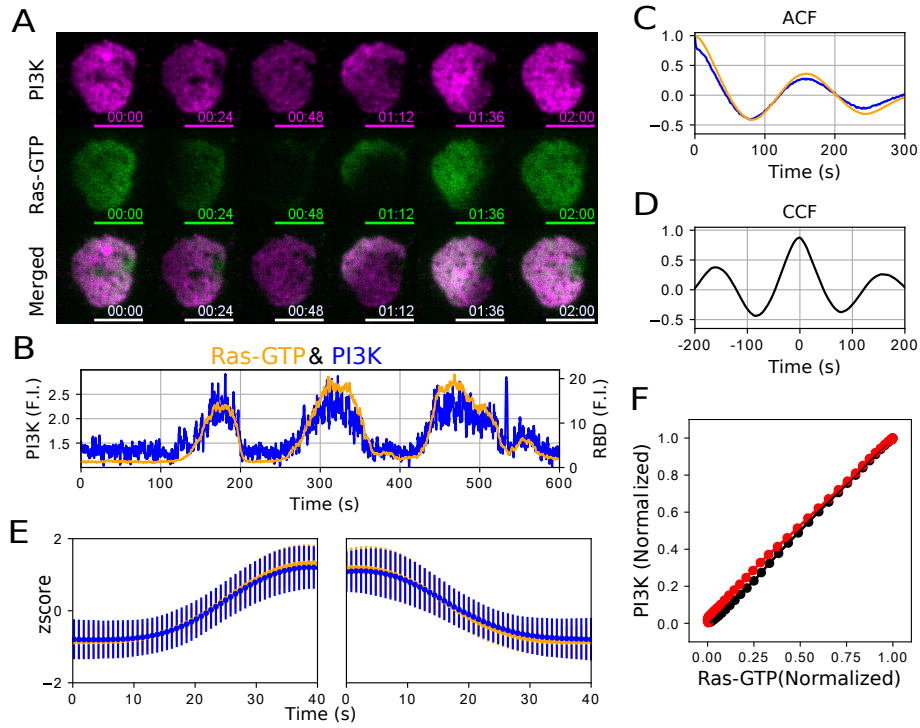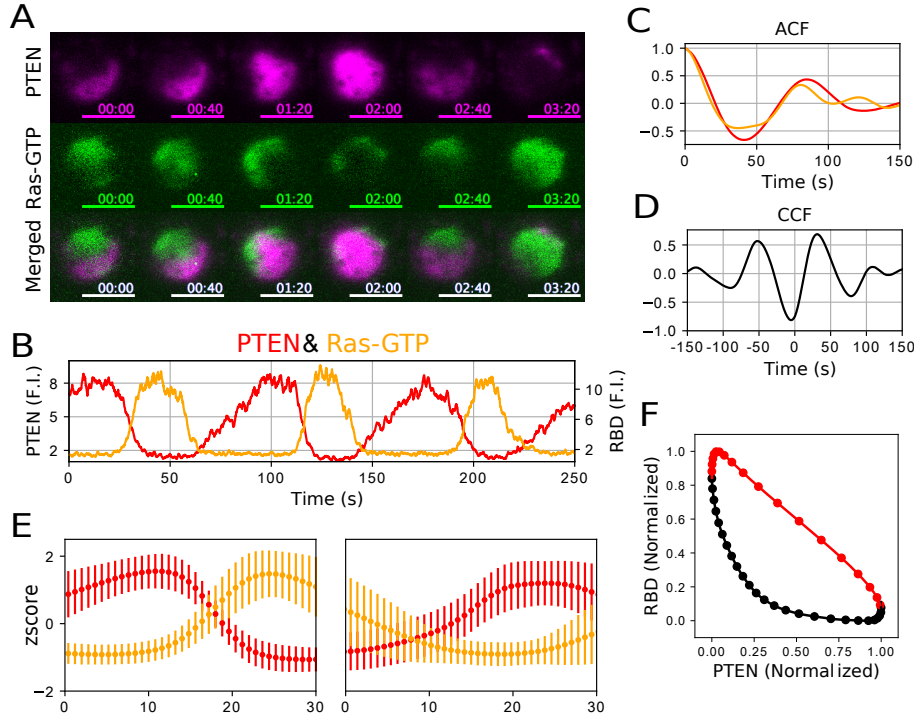

Figure 3.14: Simultaneous imaging of Ras-GTP and PI3K.
A, Simultaneous time-lapse TIRFM imaging of PI3K2-Halo-TMR and RBD$_{\text{Raf1}}$-GFP. Scale bars in the images represent 5 μm. **B,** Typical time trajectory. **C, D,** Auto- and cross-correlation functions of the trajectory. **E,** Average trajectories of the increase phase (left) and decrease phase (right). Data are the mean $\pm$ s.d. of the z-scores of intensity from 22 cells. **F,** Phase diagrams of Ras-GTP and PI3K based on the average trajectories shown in (E).

I confirmed the relationship of PTEN and PIP2 against Ras-GTP as well. The temporal dynamics of PTEN delayed against Ras wave (Fig.3.15A and B), that is consistent with the results above. The negative peak of the cross-correlation function of Ras-GTP and PTEN comes minus value (Fig.3.15D). The average minus peak value 4.7 ± 0.8 s (Fig.3.17D) also indicates the inverted dynamics of PTEN delayed with PI3K. Average trajectory and phase diagram shown in Fig.3.15E and F indicates that increase of Ras-GTP precedes a decrease of PTEN and PTEN increases after Ras-GTP has decreased. PIP2, that shows an inverse relationship with PIP3, also delayed against Ras wave (Fig.3.16A and B). The minus peak value of cross-correlation function of Ras-GTP and PIP2 was 2.7 ± 2.4 s on average (Fig.3.17E). Phase diagram shown in Fig.3.16F was a mirror image of that of PIP3 and Ras-GTP, that is well consistent with other results. These results indicate that PIP3, PIP2 and PTEN localization patterns follow Ras wave pattern.

Figure 3.15: Simultaneous imaging of Ras-GTP and PTEN.
A, Simultaneous time-lapse TIRFM imaging of PTEN-Halo-TMR and RBD$_{Raf1}$-GFP. Scale bars in the images represent 5 μm. **B,** Typical time trajectory. **C, D,** Auto- and cross-correlation functions of the trajectory. **E,** Average trajectories of the increase phase (left) and decrease phase (right). Data are the mean $\pm$ s.d. of the z-scores of intensity from 19 cells. **F,** Phase diagrams of PTEN and Ras-GTP based on the average trajectories shown in (E).
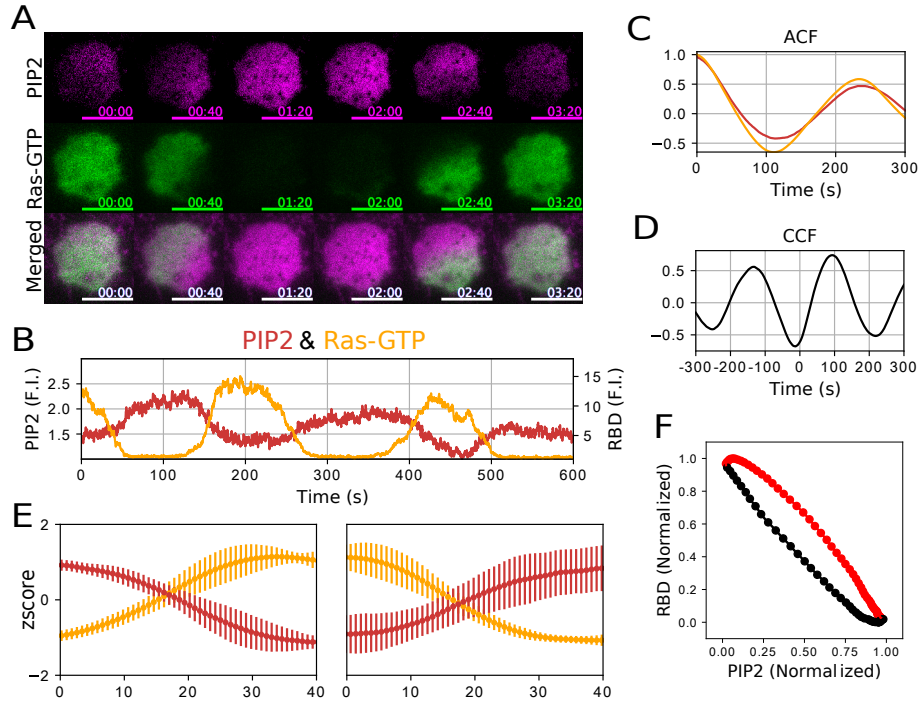
Figure 3.16: Simultaneous imaging of Ras-GTP and PIP2.
A, Simultaneous time-lapse TIRFM imaging of RFP-Nodulin and RBD$_{Raf1}$-GFP. Scale bars in the images represent 5 μm. **B,** Typical time trajectory. **C, D,** Auto- and cross-correlation functions of the trajectory. **E,** Average trajectories of the increase phase (left) and decrease phase (right). Data are the mean $\pm$ s.d. of the z-scores of intensity from 23 cells. **F,** Phase diagrams of PIP2 and Ras-GTP based on the average trajectories shown in (E).
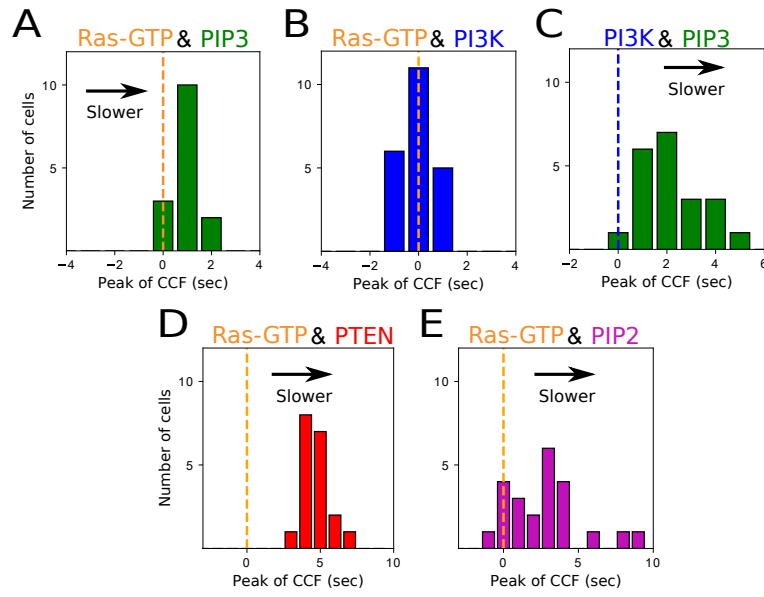
Figure 3.17: Delay of wave patterns against Ras-GTP wave.
A-E, Distribution of peak time of the cross-correlation functions. Dotted lines indicate time zero. The average peak values are 0.9 ± 0.6 s (B: n = 15 cells), 0.0 ± 0.7 s (A: n = 22 cells), 2.3 ± 1.1 s (C: n = 21 cells), 4.7 ± 0.8 s (D: n = 19 cells) and 2.7 ± 2.4 s (E: n = 23 cells), respectively.

3.3.2 Ras wave without PIP3 wave

To see whether the Ras wave requires the PIP3 wave or not, I observed Ras-GTP in *pi3k1-5* null and *pten* null cells. PIP3 wave was not observed in both mutants because PI3K and PTEN are essential for PIP3 wave generation [39]. As a result, Ras-GTP exhibited the wave propagation even in *pi3k1-5* null and *pten* null cells, whereas PIP3 didn't (Fig.3.18A and B). Compared with the wave patterns in WT cells, Ras waves in the mutant cells exhibited zigzag or disconnected patterns more frequently. I counted the cells showing Ras-GTP-enriched domain (Ras domain) and obtained the ratio of cells showing Ras domain (Ras domain ratio). The Ras domain ratio in WT, *pi3k1-5* and *pten* null cells were 84% (n=1541), 63% (n=1487) and 76% (n=1982), respectively (Fig.3.20A). The oscillatory periods were prolonged in both mutants compared with WT (Fig.3.20B). Because the *pi3k1-5* null cells exhibited no PIP3 accumulation at all and the *pten* null cells exhibited excess PIP3 signals to cover the whole membrane (Fig.3.18B), these results indicate PIP3 production and degradation are not necessary for the Ras wave generation, but have some effects on maintaining the Ras waves.
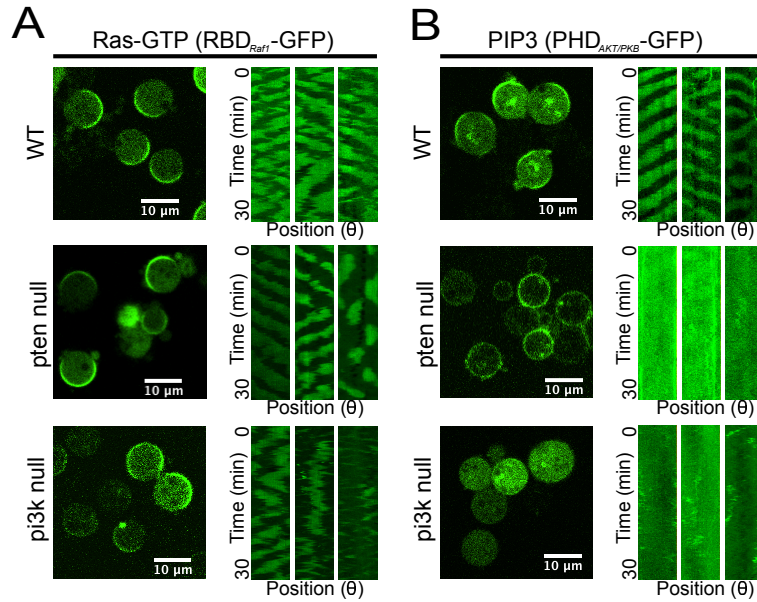

Figure 3.18: Ras wave in PIP3 production mutants.
A, B, Confocal images (left) and typical kymographs (right) of Ras wave (A) and PIP3 wave (B) in WT, *pten* null and *pi3k1-5* null cells. PIP3 waves were not observed in *pten* null and *pi3k1-5* null cells.

I further examined the possible involvement of other parallel chemotactic signaling pathways in the Ras wave generation with Torin2 and BPB, which are specific inhibitors for the TorC2 pathways, respectively. When these inhibitors were added to *pi3k1-5* null cells, no obvious changes in Ras waves were observed (Fig.3.19B and 3.20A). Even in the cells with all four major pathways (the PIP3, TorC2, PLA2, and sGC pathways) inhibited [122][102], the Ras waves were still observed, but with some defects (Fig.3.19A, C and 3.20A). Thus, none of the four major pathways, which mediate chemotactic signals downstream of Ras small GTPase, were necessary for the Ras wave formation. That is, the spatiotemporal dynamics of Ras is excitable without the activities of the downstream pathways.

Furthermore, I confirmed that Ras-GTP/PI3K interaction is required for PIP3 wave generation based on the observation that PIP3 localization in the *pi3k1-5* null cells transformed with PI3K2-Halo-TMR but not with PI3K2^{K857,858E}-Halo-TMR (Fig.3.21). Taken together with the observation that the Ras wave is generated independently of PIP3, PI3K and PTEN, these results demonstrate that Ras-GTP wave triggers PIP3 waves through Ras-GTP/PI3K interaction, and that PIP3 subordinates with Ras wave.

3.3.3 contribution of Ras subtypes on Ras wave.

Within the Ras superfamily in *Dictyostelium* cells, RasC and RasG are well characterized as regulators of cAMP-induced chemotactic signaling [91][92][77][96][124]. To see which Ras have a major role in the wave generation, I observed RBD$_{Raf1}$-GFP in *rasG*- and *rasC*-null cells. Both mutant cells showed Ras waves (Fig.3.22A and B). The efficiencies observed in *rasG*- and *rasC*-null cells were about 40% (n=650) and 84% (n=1247), respectively (Fig.3.22C). RasG-deficient cells exhibited longer wave periods than WT cells, but with wave propagations that terminated during the observation (Fig.3.22D), while Ras waves in *rasC* null were indistinguishable to those in WT. These results indicate that Ras waves are mainly mediated by the regulation of RasG activity, but not RasC with some redundancy.
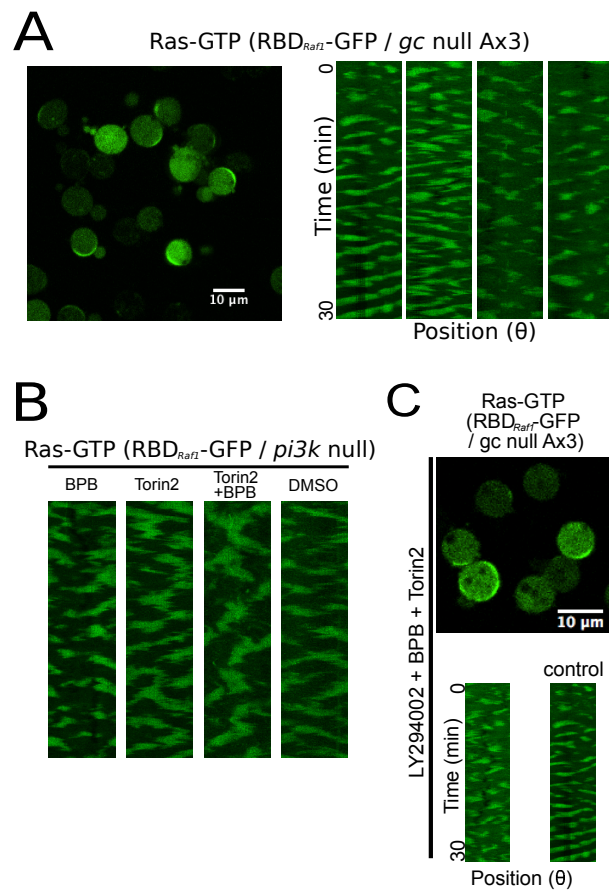
Figure 3.19: Ras wave under major four signaling pathways inhibition.

A, Confocal image and kymographs of *gc* null cells (Ax3 strain). **B,** Kymographs of *pi3k1-5* null cells treated with 2 μM BPB, 10 μM Torin2, the combination of them and 1% DMSO. **C,** Confocal image and kymographs of *gc* null cells (Ax3 strain) treated with the combination of 100 μM LY294002, 10 μM Torin2 and 2 μM BPB.
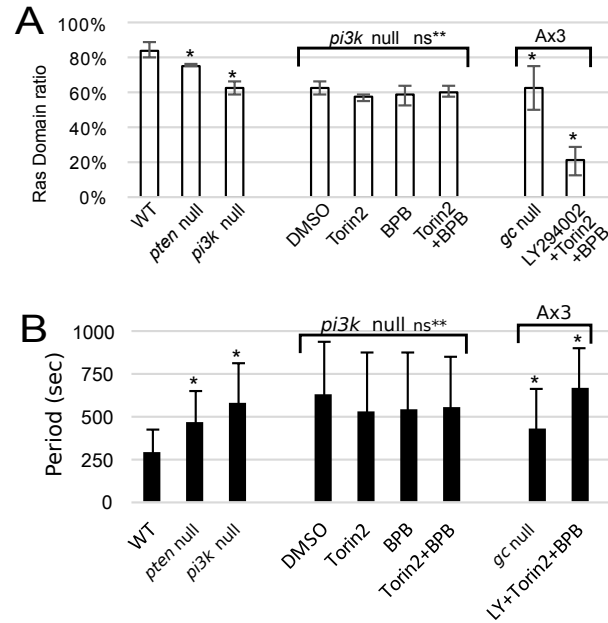
Figure 3.20: Ras domain ratios and wave periods.
A, Ratio of the number of cells showing Ras-GTP-enriched domains. Data are mean
± s.d. of three independent experiments, and more than 200 cells were counted in
each experiment. (* P < 0.01 Welch's t-test against WT; ns** P > 0.01 Welch's
t-test against *pi3k1-5* null). **B,** Ras wave periods were calculated from the auto-
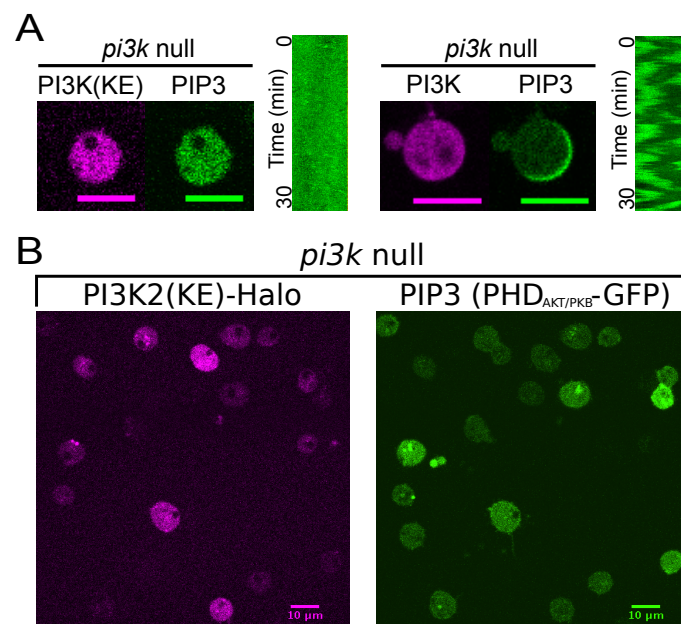correlation function of more than 20 cells and averaged (* P < 0.01 Welch's t-test
against WT; ns** P > 0.01 Welch's t-test against *pi3k1-5* null).

Figure 3.21: Rescue experiment of *pi3k1-5* null mutant.
A, Confocal images of the rescue experiments of *pi3k1-5* null cells with PI3K or PI3K(KE). Scale bars in the images represent 10 μm. **B,** PIP3 domain formation is not rescued in these cells. More than 100 cells were observed for each experiment.
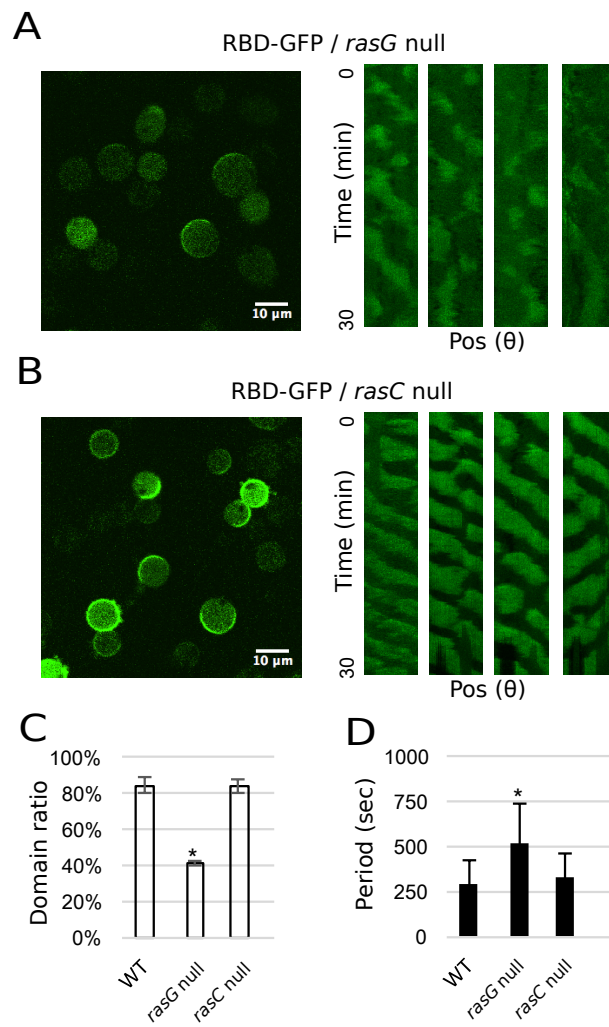
Figure 3.22: Contribution of Ras subtypes to Ras wave.
A, B, Confocal image and kymographs of *rasG* null (A) and *rasC* null cells (B).
C, D, Ras domain ratios and wave periods of WT, *rasG* null and *rasC* null cells.

3.4 The regulations of Ras excitability

3.4.1 PI3K inhibition experiments and Ras wave

In contrast to Ras waves being generated in *pi3k1-5* null cells (Fig.3.18A), a previous study has shown that Ras waves were suppressed by the PI3K inhibitor LY294002 [79][39], suggesting feedback from PI3K/PIP3 to Ras. In order to investigate this apparent inconsistency between the genetic and pharmacological inhibition of PI3K activity in more detail, I performed PI3K inhibition experiments with LY294002. When treated with 40μM LY294002, the Ras wave vanished in some cells, as reported previously (Fig.3.23A). I counted the number of cells showing Ras domain and obtained the Ras domain ratio (Fig.3.23C). Before LY294002 treatment, about 80% of cells showed Ras domain, but 10 minutes after the treatment, Ras domains were vanished about 30% of cells. However, after 1 hour from the treatment, recover of Ras domain formation was observed in 15% of cells. This transition was not observed in *pi3k1-5* null cells. Recovery of the Ras domain was observed even after the treatment with higher concentration LY294002 (Fig.3.23B). When treated with 100μM LY294002, the Ras domain ratio became 1% 10 minutes after the treatment and recovers to 36% 60 minutes after the treatment (Fig.3.23D). It was reported that 100μM LY294002 suppress PIP3 pathway almost same level as *pi3k1-5* null cells, but it affect another pathway in some degree ([125]). The result of *pi3k1-5* null cells treated with 100μM LY294002 indicates that off-target of LY294002 also inhibits Ras domain formation. However, the effect was not seen in 40μM concentration, suggesting that the influence of off-target is smaller than that of the influence of PI3K inhibition.

In order to analyze detail of the transition after the LY294002 treatment, I obtained domain ratio of Ras-GTP and PIP3 in 5 minutes interval (Fig.3.24A and B). Before LY294002 treatment, about 80% of cells showed both Ras and PIP3 domains, in which RBD_{Raf1} and $PHD_{AKT/PKB}$ were colocalized on the membrane. 10 minutes after the treatment, Ras and PIP3 domains were observed only in about 10% and 1% of cells, respectively. After that, Ras domains started to recover 15 minutes after treatment. 60 minutes after the treatment, Ras domains had recovered in about 37% of cells. Ras domains recovered gradually in the presence of LY294002, whereas PIP3 domains didn't under the condition of 100μM LY294002 (Fig.3.24A). These results are consistent with the conclusion that Ras wave generation is essentially independent of PIP3 production (Fig.3.18A).

In the case of 40μM LY294002, Ras domain ratio marked minimum value (46 %) at 5 minutes (Fig.3.24B). After that, Ras domain ratio recovered gradually. Along the drop and recovery of the Ras domain ratio, the PIP3 domain ratio also showed drop and recover in the same time course. The PIP3 domain ratio was always lower than the Ras domain ratio, also suggesting that formation of PIP3 domain follows that of Ras domain. There
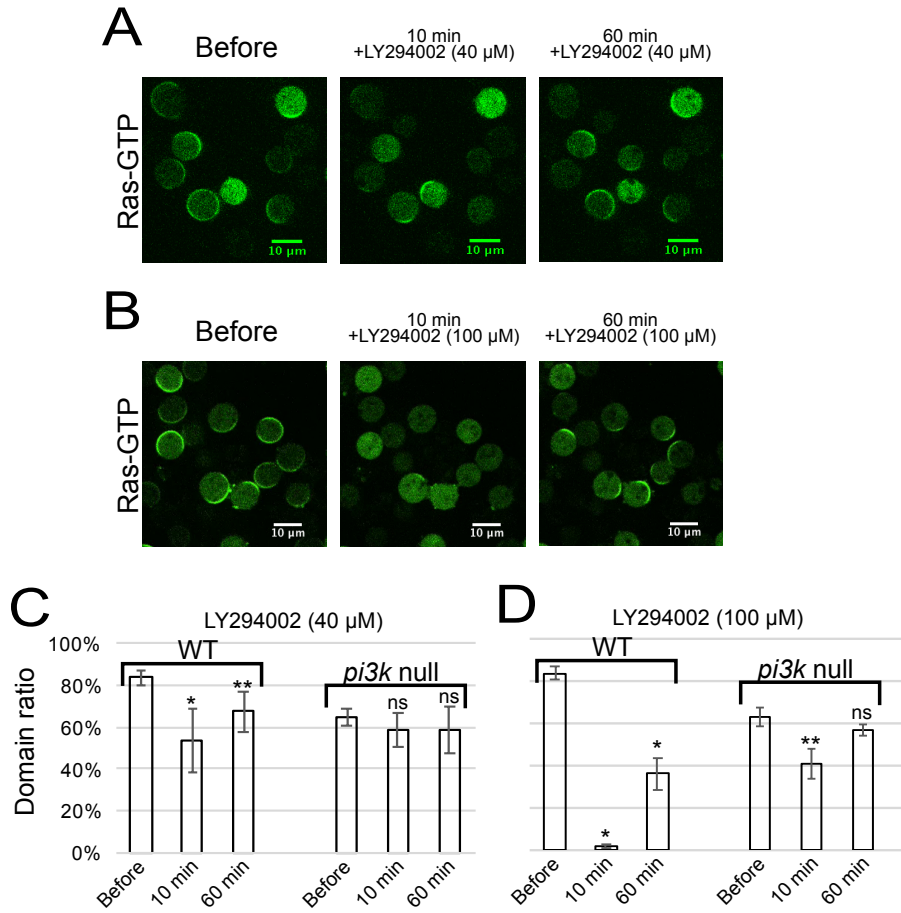
Figure 3.23: Recovery of Ras wave after PI3K inhibition.
A, B, Response of Ras waves to a PI3K inhibitor (40 or 100 μM LY294002) before
(left) and after 10 min (center) and 60 min (right) from the treatment. **C, D,** Ratio
of the number of cells showing Ras domains before and after treatment with 40 or
100 μM LY294002 in WT and *pi3k1-5* null cells. Data are mean $\pm$ s.d. of three
independent experiments. More than 45 cells were counted in each experiment. (*
$P < 0.01$, ns > 0.01 Welch's t-test; comparisons were made with "Before" column
for the same cell type. ** $P < 0.05$ Welch's t-test; comparisons were made with
"Before" and "10 min" columns for the same cell type).

were no remarkable effects by 40μ LY294002 on the Ras domains in *pi3k1-5* null cells (Fig.3.24D). But after 100μ LY294002 treatment, the Ras domain ratio in *pi3k1-5* null cells decreased and had a minimum value (40 %) at 10 minutes (Fig.3.24C). These results indicate that the transition after the LY294002 treatment has two phases. One is a fast decrease which is PI3K inhibition dependent and has bottom at 5 minutes or less. The other is the slow decrease which is LY294002 off-target dependent and has bottom at 10 minutes. The transient defects of Ras waves by PI3K inhibition suggest that Ras, PI3K and PIP3 waves are tightly coupled in WT cells at the default state.
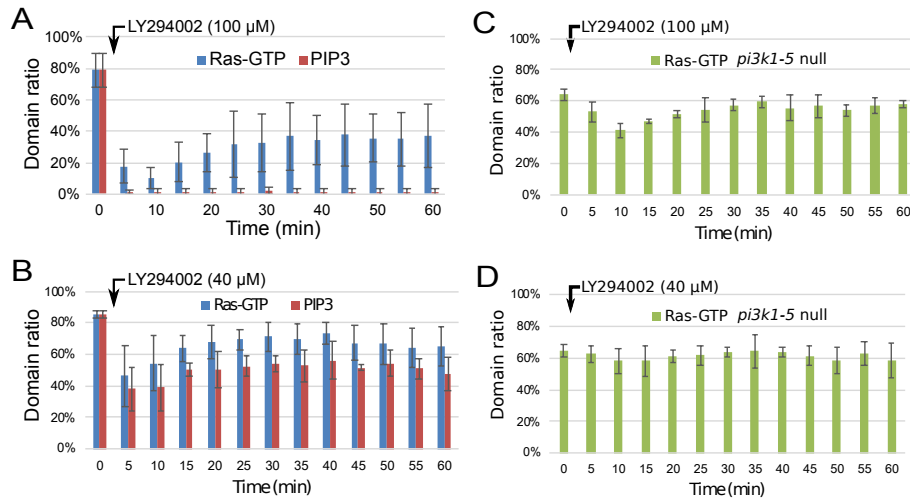

Figure 3.24: Transition of the Ras domain ratio after PI3K inhibition.

A-D, C, Ratio of the number of cells showing Ras-GTP or PIP3 domains after treatment with LY294002. Data are mean $\pm$ s.d. of three independent experiments. More than 40 PHD$_{\text{AKT/PKB}}$-GFP and RBD$_{\text{Raf1}}$-RFP doubly expressed cells (A and B), and more than 50 PHD$_{\text{AKT/PKB}}$-GFP expressed *pi3k1-5* null cells were observed (C and D).

Next, I focused on the pattern of Ras wave and domain formation. Kymographs of Ras-GTP localization pattern before and after the treatment were shown in Fig.3.25. After the treatment, Ras-GTP wave patterns are vanished once and most of cells show no recovering of Ras-GTP wave under the condition with 100μM LY294002. Some cells show recovering of Ras-GTP wave or stochastic Ras domain formation as shown in Fig.3.25A. This trend is similar to that under the condition with 40μM LY294002 (Fig.3.25B). In *pi3k1-5* null cells, Ras waves were unstable and sometimes showed zigzag or disconnected patterns mixed with traveling wave, standing wave and stochastic domain formation even before the treatment (Fig.3.25C). After the treatment, Ras wave patterns were vanished or disordered once, and after that, it showed a disordered pattern again, that is different from the case of WT cells. When *pi3k1-5* null cells were treated with 40μM LY294002, no obvious change was observed (Fig.3.25D).

In order to clarify the difference of Ras domain pattern, I measured domain size and lifetime of each domain in each cell before and after the treatment (Fig.3.26). Domain size is defined as the average spatial size of each domain and the lifetime is defined as a duration time of each domain. In the case of WT cells treated with 100μM LY294002 and 40μM LY294002, the domain size became smaller and lifetime became shorter after the treatment than that before (Fig.3.26A and B). In almost all cells, the scattered plot of domain size and lifetime shift smaller and shorter area after the treatment (Fig.3.26C), that was not seen in the case of *pi3k1-5* null cells. These results indicate that inhibition of PI3K and PIP3 production is critical for domain size and duration time of Ras-GTP wave. This suggests feedback regulation from PIP3 to Ras contributes to maintain excitation of the Ras signaling pathway spatiotemporally. It is expected that less continuous of the Ras domain after PI3K inhibition is derived from drop of excitability of the Ras signaling pathway. I discussed this point later.

For comparison, I performed PTEN inhibition experiment with some PTEN inhibitors, 30μM VO-OHpic and 50μM SF1670 [64][65][68][69]. However, no significant effect on Ras/PIP3 wave was observed in *Dictyostelium* cells. Another method for manipulating PTEN activity is necessary for further experiment.
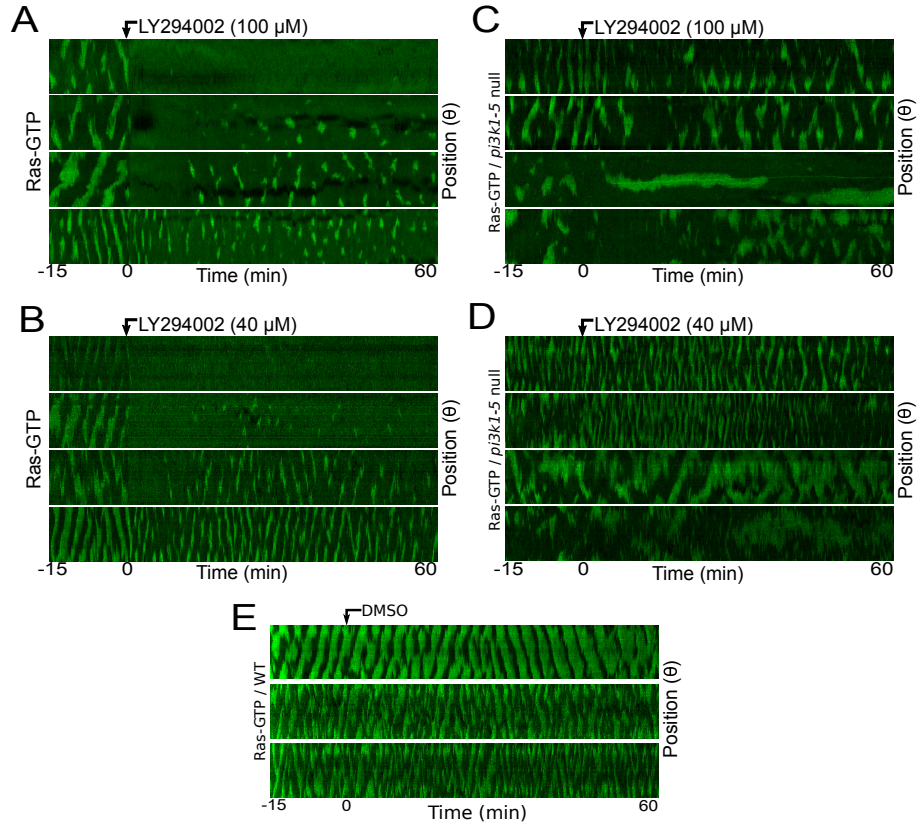
Figure 3.25: Kymograph analysis of recovery of Ras domain.
A-D, Kymographs show typical responses of Ras wave to the treatment of
LY294002 in WT cells (A, B) and *pi3k1-5 null* cells (C, D), respectively. **E,** Ky-
mograph shows typical responses of Ras wave to the treatment of 0.25% DMSO in
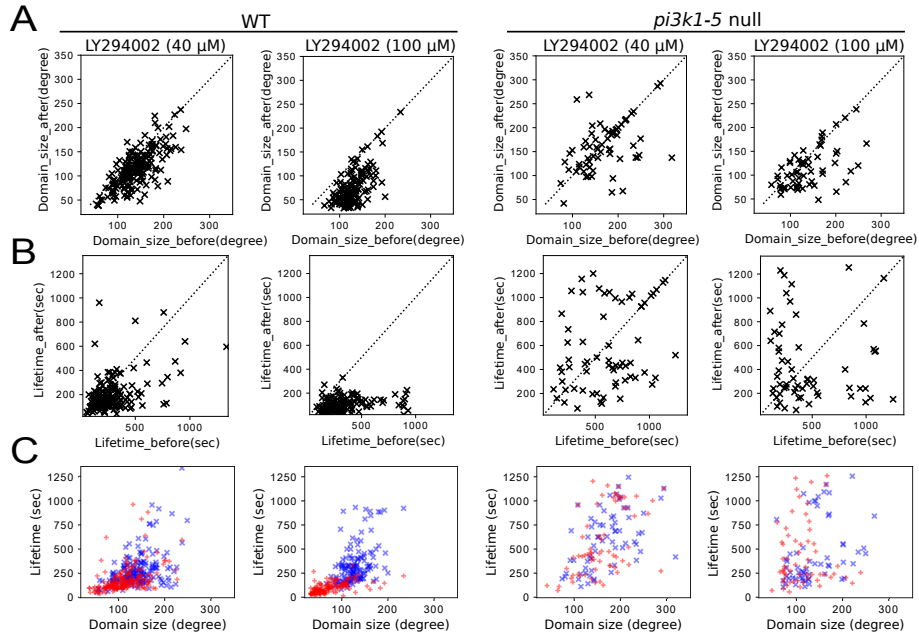WT cells.

Figure 3.26: Transition of the size and lifetime of Ras domain after PI3K inhibition.

A, B The domain size (A) and lifetime (B) of the Ras wave pattern before and after the treatment of LY294002 in each cell. Dotted lines indicate where before equals after. These values were measured and averaged in each cell. 191, 140, 66 and 63 cells were measured, respectively. **C,** Distribution of domain size and lifetime of Ras domain formation before (blue) and after (red) the treatment.

3.4.2   Crosstalk regulation from sGC pathway.

A recent study revealed that soluble guanylyl cyclase (sGC) pathway exhibits an excitable respnse against cAMP stimuli with shorter refractory period than Ras/PIP3 pathway [128]. In this study, it was discussed that the existence of cross talk between sGC pathway and Ras/PIP3 pathway. In fact, the Ras domain ratio was decreased in *gc* null mutant (Fig.3.20. On the other hand, it was reported that membrane sGC localization strongly depends on F-actin. Actually, sGC localization in Latrunculin A treated cells was not reported.

Then, I performed TIRF observation of sGC in sGC-RFP and $PHD_{AKT/PKB}$-GFP double expressed cells treated with Latrunculin A (Fig.3.27A). Trajectory analysis revealed that sGC shows a negative correlative localization pattern with PIP3 wave (Fig.3.27C-E). This result suggests that the opposite regulation for the sGC and PIP3 signalings in the excitable Ras wave under the condition lacking F-actin. I noticed that GbpC which is a major cGMP effector didn't show any localization pattern under this condition (data not shown), though GbpD, it has no cGMP binding ability shows the same localization pattern as sGC (Fig.3.27B, F-H). These results suggest that sGC localization patterns under presence of Latrunculin A is a cGMP independent process. The effect of the crosstalk regulation from sGC pathway to Ras/PIP3 pathway requires further investigation.
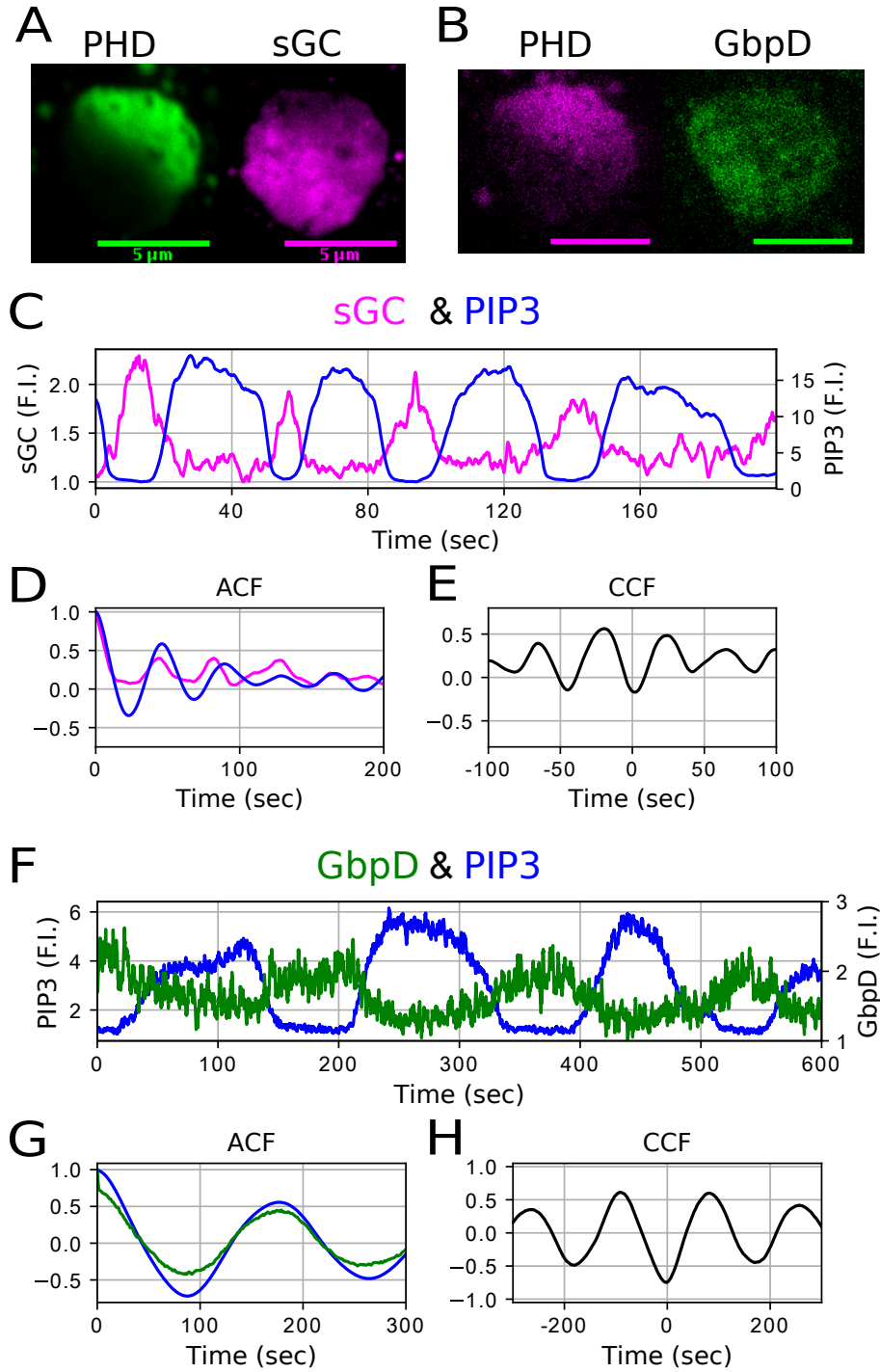
Figure 3.27: Observation of sGC and GbpD.
A, B Simultaneous TIRF image of sGC-RFP and PHD(AKT/PKB)-GFP (A) and GbpD-GFP and PHD(AKT/PKB)-RFP (B). Scale bars in the images represent 5 μm. **C, F,** Typical time trajectory. **D-E, G-H,** Auto- and cross-correlation functions of the trajectory.

3.4.3 For the identification of Ras regulators.

As a candidate of delayed negative regulator of Ras excitability, I performed some experiment about NfaA, that is one of the major RasGAP in Ax2 strain. NfaA was found as mutant of *Dictyostelium* Nurofibromin-1 homologous gene (NF1), that is related to the human nerve tumor, Neurofibroma [139]. NF1 and nfaA are RsaGAP family protein and contain PHD and SEC14 homology module which related to lipid binding. Axenic strain 2 of *Dictyostelium discoideum* (Ax2) that I used as a WT strain in this study, is mutant isolated from NC4. NC4 has NF1 protein, and Ax2 has NfaA instead of NF1. NfaA was reported that weaker RasGAP activity than NF1 [108].

First, I observed localization pattern of NfaA-Halo-TMR in NfaA-Halo and $PHD_{AKT/PKB}$-GFP double expressed cells (Fig.3.28A). As a result, NfaA showed the localization pattern coinsides with PIP3 wave (Fig.3.28B-D), though the magnitude was weaker than that of PIP3. It suggests that NfaA can play a role of delayed negative regulator. Next, I observed PIP3 localization pattern in *nfaA* knockout cells (Fig.3.28E). Before the treatment of 4mM caffeine (Fig.3.28E left), PIP3-enriched domains in *nfaA* null cells were larger than that in WT cells, suggesting that nfaA negatively regulate Ras/PIP3-enriched domain formation as reported before [99]. However, after the treatment of 4mM caffeine (Fig.3.28E right), the domain size became normal size as well as that in WT cells. These results indicate that NfaA mediates negative regulation of Ras and PIP3 signaling, but it is not essential for Ras excitability and Ras/PIP3 wave formation.
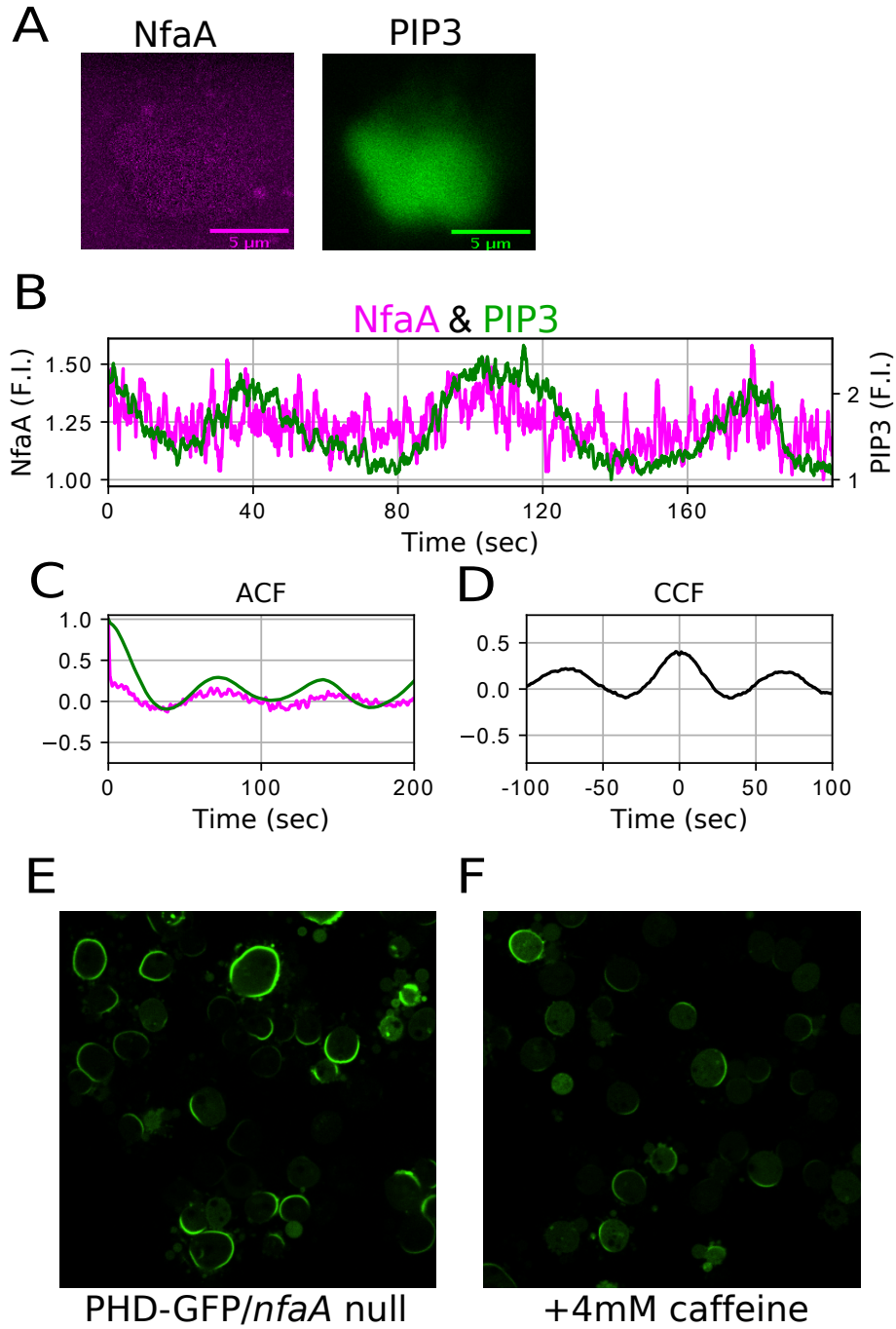
Figure 3.28: Observation of NfaA and *nfaA* null cells.
A, Simultaneous TIRF image of NfaA-Halo-TMR and PHD(AKT/PKB)-GFP.
Scale bars in the images represent 5 μm. **B,** Typical time trajectory. **C, D,** Auto-
and cross-correlation functions of the trajectory. **E, F,** Confocal images of *nfaA*
null cells expressing PHD(AKT/PKB)-GFP before (E) and after (F) treatment of
4mM caffeine.

3.5   Approach from modeling and simulation

3.5.1   Modeling of Ras/PIP3 signaling system

I constructed a theoretical model for the phosphatidylinositol lipids signaling pathway, including Ras, PI3K, PTEN, PIP3 and PIP2 to validate proposed mechanism for the self-organization of asymmetric signals (Fig.3.29). Ras excitability was modeled with positive and delayed negative feedbacks on Ras, two features commonly assumed in excitable systems and have been adopted in previous models for the self-organization of PIP3 domains [39][21][136]. The spatiotemporal dynamics of other components, including PI3K, PTEN, PIP2 and PIP3 were described by a series of reaction-diffusion equations based on the experimental observations. In brief, PI3K on the membrane is proportional to Ras-GTP levels and PIP2 catalyzes PIP3 production according to a simple Michaelis-Menten (MM) type enzymatic reaction (Fig.3.7, 3.8, 3.14 and 3.21). PTEN is recruited to the membrane via interaction with PIP2 and excluded from the membrane by interaction with PIP3, two phenomena also described by MM type binding reactions [63]. The sum of PIP3 and PIP2 concentrations locally on the membrane is constant (Fig.3.4). I introduced feedback from PIP3 to Ras to recapture the observed Ras/PI3K-PIP3 positive feedback (Fig.3.24). I introduced a hypothetical RasGEF mediates the feedback which activates Ras in a PIP3-dependent manner. Detail of the model is summarized in the Methods section (Section 2.2.7). The parameters and initial condition values are summarized in Table.2.62.7.
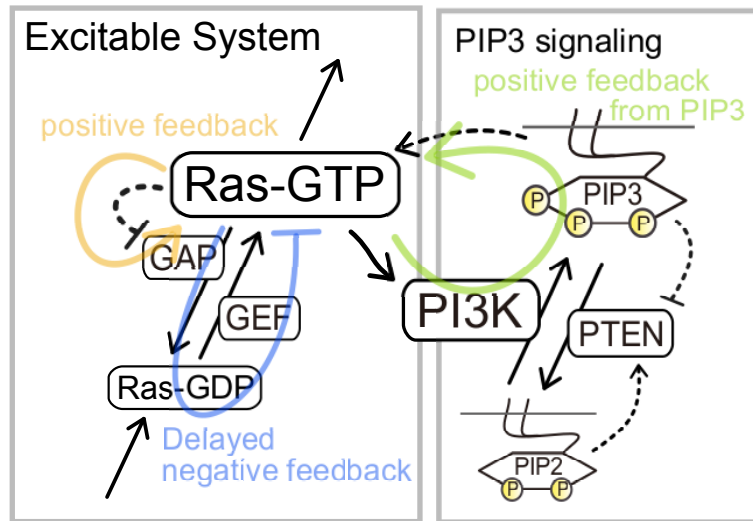

Figure 3.29: Modeling of Ras/PIP3 wave.

Scheme of the Ras/PIP3 wave model used in this study. See the Methods section (Section 2.2.7) for details.

3.5.2 Deterministic spatiotemporal simulation

I first performed the simulation to see whether or not the model can reconstruct relationship between Ras/PI3K, PTEN, PIP2 and PIP3 waves in a manner consistent with the experimental observations summarized in Fig.3.30. The detail method and model construction are described in Section 2.2.7. In this model, I introduced Ras-GTP dependent activation of PI3K and a conservation of a sum of the total number of PIP3 and PIP2 molecules. Without PI3K activity, the model successfully reconstructed Ras waves without PIP3 or PTEN waves, because of the positive and delayed negative feedbacks on Ras (Fig.3.31B). The parameters I used in this study is shown in Table.2.6, 2.7. When PI3K activity was turned on, the model reproduced PTEN and PIP3 waves in addition to Ras waves. The temporal behavior of Ras/PI3K, PTEN, PIP2 and PIP3 exhibited oscillatory dynamics (Fig.3.31A), and phase portraits plotted in the corresponding coordinates were consistent with the experimental observations (Fig.3.31C and Fig.3.30F, J, H, E). The model reproduced the triangle-shaped dynamics in Ras/PI3K-PTEN, ellipse-shaped dynamics in Ras/PI3K-PIP3 (or Ras/PI3K-PIP2), crescent-shaped dynamics in PTEN-PIP3 (or PTEN-PIP2), and the inverse relation in PIP3-PIP2. Thus, the temporal dynamics of all 10 studied combinations of the PI3K-PTEN pathway can be explained by this model, in which Ras-GTP triggers the other waves through interaction with PI3K.
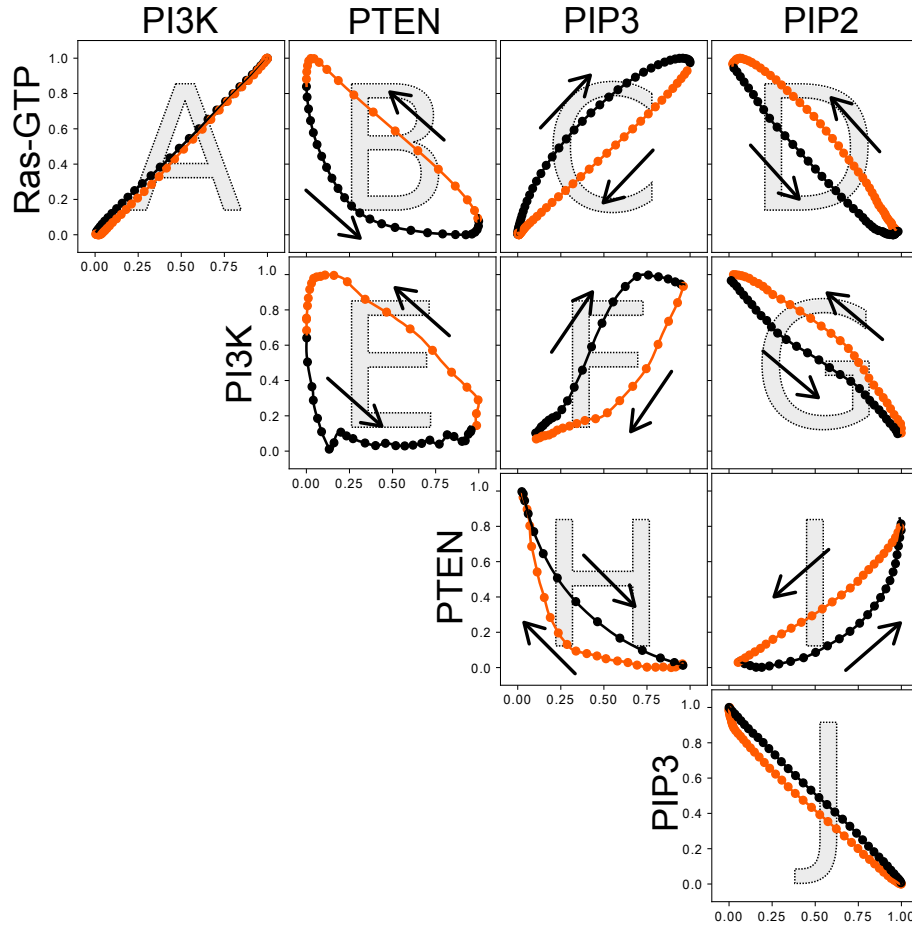
Figure 3.30: Summary of the interrelationship from experimental observations.
The summary of the interrelationship between traveling wave components from experimental observations is shown. Average dynamics of two arbitrary components are shown as an orbit in the corresponding coordinates. Arrows indicate temporal progression. Black lines indicate increased phase along the horizontal axis and red lines indicate the decreased phase. The values are the normalized fluorescence intensities based on the average trajectories.
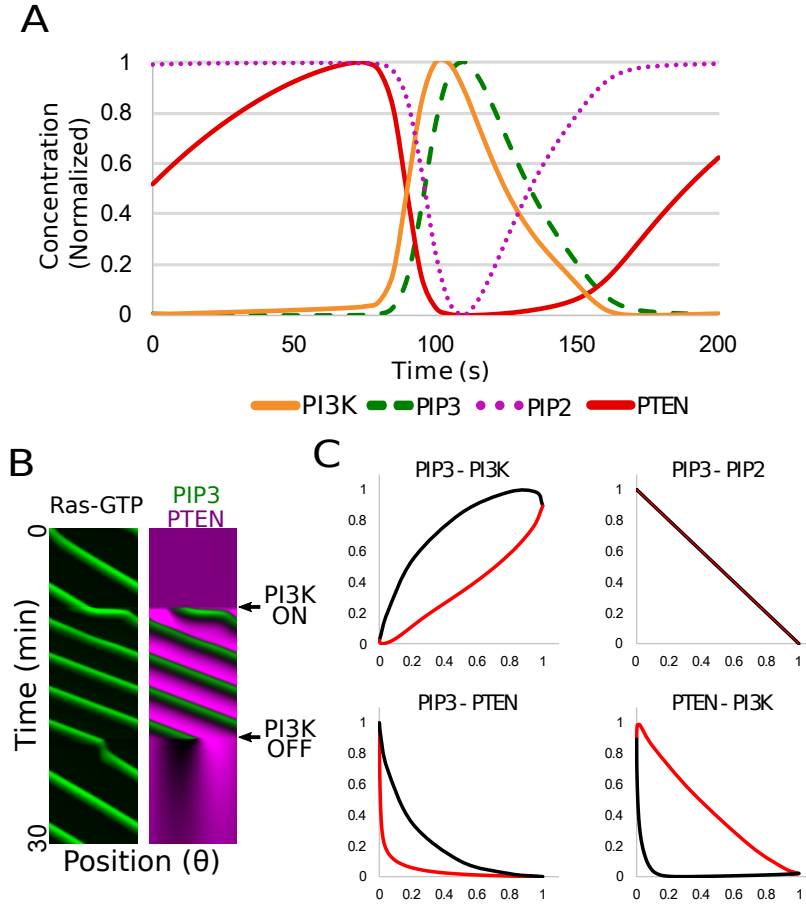
Figure 3.31: Spatiotemporal simulation of Ras/PIP3 wave.
A, An example of a steady state time course of Ras-GTP/PI3K, PIP3, PIP2 and PTEN on a membrane obtained from the simulation. **B,** The kymograph generated by a simulation based on the model. $V_{GEFs} = 550s^{-1}$. **C,** Phase portraits generated from the deterministic simulation.

3.5.3   Stochastic spatiotemporal simulation

I performed stochastic simulation and reconstruct the wave pattern formation of Ras/PIP3 wave (Fig.3.32). As described in Section 2.2.7., I applied stochasticity by introducing poison noise in the simulation by using Tau-leaping method. I used same parametes with deterministic simulation shown in Table.2.6, 2.7. As a result, I success to reconstruct noise dependent symmetry breaking and stochastic change of direction of wave propagation (Fig.3.32B).

Next, I examined the effects of Ras/PI3K-PIP3 positive feedback on Ras wave generation by mimicking the PI3K inhibition experiment shown in Fig.3.25. PI3K inhibition was simply mimicked by changing PI3K activity term, V_{PI3K} during simulation. Besides, I performed the simulation with various V_{GEFs} values to obtain various Ras domain pattern by changing basal Ras actibity. V_{GEFs} determines the basal activity of RasGEFs acting independently of PIP3 signaling. In the presence of PI3K activity, traveling waves were generated even at low V_{GEFs} (Fig.3.33A and B). This is because positive feedback regulation from PIP3 to Ras improved excitation and pattern formation of Ras. Upon the inhibition of PI3K and thus the positive feedback regulation, Ras wave dynamics became dependent on V_{GEFs}. Under two extreme conditions of low and high V_{GEFs}, Ras waves were totally impaired or unaffected, respectively. Under intermediate conditions, Ras waves exhibited a recovery after a transient loss (3.33A middle).

The transient loss and recovery can be explained by relaxation of the system from the loss of positive regulation. In this excitable system, Ras-GTP basal levels and positive feedback regulations defines the distance to the threshold of excitation. PI3K inhibition induces both decrease of Ras-GTP basal levels and magnitude of positive feedback regulation, leading to a loss of Ras excitation. Then, the delayed negative feedback working on Ras gradually loses because of lower Ras-GTP level, allowing the system to exceed another Ras-GEF basal level. If the basal level with noise reaches the threshold, the system recovers domain formation or wave pattern formation. This relaxation effect depends on the system and it cannot explain recovery after the long lag time seen in the experiment. The recovery can be also reproduced by increasing V_{GEFs} with a lag time after PI3K inhibition, which can be explained by changing the expression levels of the components responsible for Ras excitation.

Finally, I performed a kymograph analysis of the Ras dynamics obtained from the simulation and found that the size and lifetime of the Ras domain became smaller and shorter after the inhibition of PI3K activity, respectively, which is in good agreement with the experimental observations (Fig.3.33C-E). These results suggest that PIP3 waves contribute to the maintenance of Ras excitability via positive feedback, and that my model could almost fully reproduce the behaviors of Ras/PIP3 signaling observed in this study.
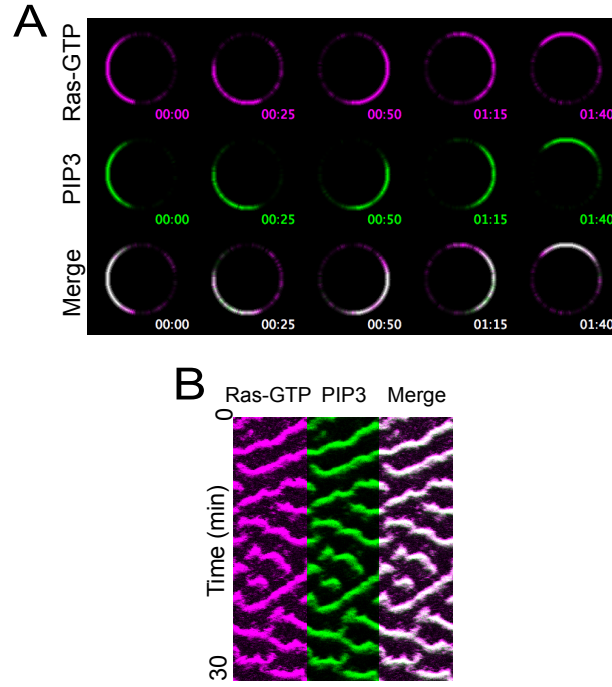
Figure 3.32: Stochastic simulation of Ras/PIP3 wave.
A, Ras-GTP and PIP3 traveling waves generated from the spatiotemporal stochastic simulation of the model shown in Fig.6A. $V_{\mathrm{GEFs}} = 550s^{-1}$. **B,** Kymographs based on (A).
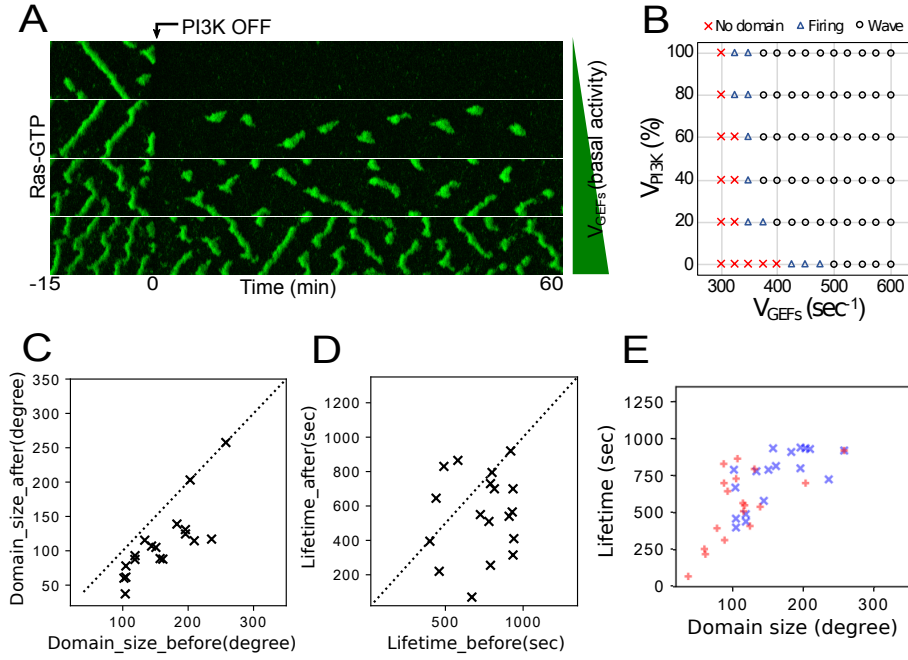
Figure 3.33: Reconstruction of PI3K inhibition experiment.
A, Spatiotemporal stochastic simulation of the model and PI3K inhibition. Kymographs show waves before and after PI3K inhibition. After PI3K inhibition, Ras waves vanished immediately, but recovered after a few minutes, depending on the basal activity ($V_{GEFs} = 400, 420, 450, 500 s^{-1}$). **B,** The plot shows the relationship between the Ras-GTP localization pattern and parameters ($V_{GEFs} = 300 \sim 600 s^{-1}$ in 25 increments and $V_{PI3K} = 0 \sim 100$ % in 20 increments). **C, D,** Distribution of the domain size and lifetime transition of the Ras wave pattern in each cell. Dotted lines indicate where 'before' equals 'after' ($V_{GEFs} = 400 \sim 570 s^{-1}$ in 10 increments). **E,** Distribution of domain size and duration time of Ras wave pattern before (blue) and after (red) the PI3K inhibition.

Chapter 4

Discussion

Live-cell imaging analysis of asymmetric signal generation in the phosphatidylinositol lipids signaling pathway demonstrates there exists at least three characteristics of the self-organization processes. First, all components observed in the signaling pathway are self-organized to generate traveling waves along the membrane in a closely coupled manner (Section 3.3.1). Second, among these components, Ras small GTPase has a central role in the asymmetric signal generation and triggers the wave generation of the other components through PI3K activation (Section 3.3.2). Third, feedback on Ras from the downstream molecules stabilizes the asymmetric signal generation (Section 3.4.1). Overall, these experimental observations demonstrate that Ras has excitable dynamics and governs spatiotemporal dynamics in the phosphatidylinositol lipids signaling pathway for the asymmetric signal generation. The mathematical modeling of the spatiotemporal dynamics of Ras/PIP3 wave can explain that Ras excitability breaks symmetry in the phosphatidylinositol lipids signaling pathway, thus generating PIP3-enriched domains (PIP3 domain) for cell motility (Section 3.5).

4.1 High-sensitive observation of membrane localization patterns.

High-sensitive multi-color TIRF microscopy enabled to observe all of PIP3 related molecules along with PIP3 wave (Section 3.1.1 and 3.2.1). Fluctuation of PIP2 had not been reported because of the narrow dynamic range of PIP2 probes. PI3K localization on a membrane had not been observed because of the low ratio of membrane signal against cytosolic signal. TIRF microscopy is suitable for sensitive observation because of high signal to noise ratio and lower cytosolic background. This method enabled to observe both of PIP2 and PI3K localization pattern on a membrane as shown in Fig.3.4 and 3.6. Besides, high temporal resolution of this method also enables to detect the delay of the PIP3 wave propagation against the PI3K localization pattern and Ras wave (Fig.3.17). This observation method can be applied

77

for evaluation of localization and symmetry breaking of all molecules on a membrane. In fact, this method contribute to finding other molecules showing membrane localization pattern on a membrane (Fig.3.27 and 3.28). Additionally, by combining single-molecule analysis method, it realized to obtain the membrane binding parameters at the same time (Section 3.2.2).

4.2 Single-molecule analysis revealed the behavior of PI3K on a cell membrane.

About translocation of PI3K, previous studies mainly focused on F-actin dependent pseudopod translocation mediated by N-terminal domain. In this study, I found the F-actin independent membrane translocation of PI3K (Section 3.2). Localization observation and single-molecule analysis revealed that the localization pattern is regulated by interaction with Ras-GTP. Though the N-terminal domain is necessary for the pre-binding to a cell membrane, it also exhibited a prolonged membrane binding lifetime in the active sight, indicating that is responsible for difference of membrane fractions. (Fig.4.1). The analysis of displacement length revealed PI3K has more than 4 diffusion states on a membrane (Fig.3.9). In the case of PTEN, the number of diffusion states was expected 3 states, suggesting there are more complex regulations in PI3K membrane binding. The population of two slow diffusion states of PI3K was increased in the active site, indicates slow diffusion state related to interaction with Ras-GTP (Fig.3.10). The number of diffusion states and the population of slow diffusion states were not changed even without an actin polymerization inhibitor Latrunculin A (Fig.3.11). A membrane binding lifetime was also not changed in the condition without Latrunculin A, indicating that the behavior of PI3K on a cell membrane can be explained in F-actin independent manner. It is expected that F-actin dependent localization of PI3K is not the localization to the cell membrane, but the enrichment to the cytosol in pseudopod with high F-actin concentration. That induces high association of PI3K on a membrane, but not affects on dissociation and diffusion of PI3K on a membrane. These results demonstrated that importance of Ras-GTP on the regulation of PI3K on a cell membrane.

4.3 PIP3 signaling pathway is regulated by Ras wave.

From the simultaneous imaging of PIP3, PIP2, PTEN, PI3K and Ras-GTP, I found accumulation of Ras-GTP and PI3K happened before the increase of PIP3 and decrease of PTEN (Fig.3.13 and 3.15). The order of temporal development reflects the mechanism of pattern formation. This result suggests Ras-GTP mediated PI3K membrane translocation is a key event
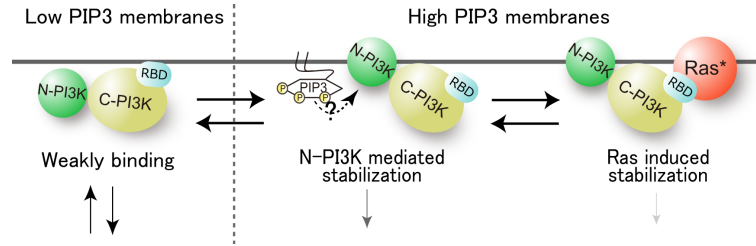
Figure 4.1: Summary of the single molecule analysis of PI3K.
.

of symmetry breaking of PIP3 localization (Fig.4.2). PTEN localization change can be explained by negative regulation from PIP3 [39][72]. From the observation that PIP3 and PTEN shows mutually exclusive localization pattern, it is estimated that there PIP3 suppresses the membrane binding of PTEN. Recently, it was reported that small G protein Arf regulates PTEN membrane binding and mutual exclusive localization of PTEN against PIP3 (Degawa et al., preparing submission). Accumulation of PI3K induces PIP3 increase, and PIP3 increase induces PTEN decrease. This induces more increase of PIP3 in positive feedback manner. Dissipation of Ras-GTP and PI3K also happened before the decrease of PIP3 and increase of PTEN. This indicates a positive feedback regulation composed of PIP3 and PTEN acts like two state switch, and the transition is regulated by Ras-GTP. This can enhance the response of PIP3 localization to the 'all or none' signal from Ras-GTP. The model and numerical simulation of PIP3 wave is well reconstructed the wave pattern and relationships (Fig.3.31), that supports PIP3 signaling pathway is two state switch regulated by Ras signaling.
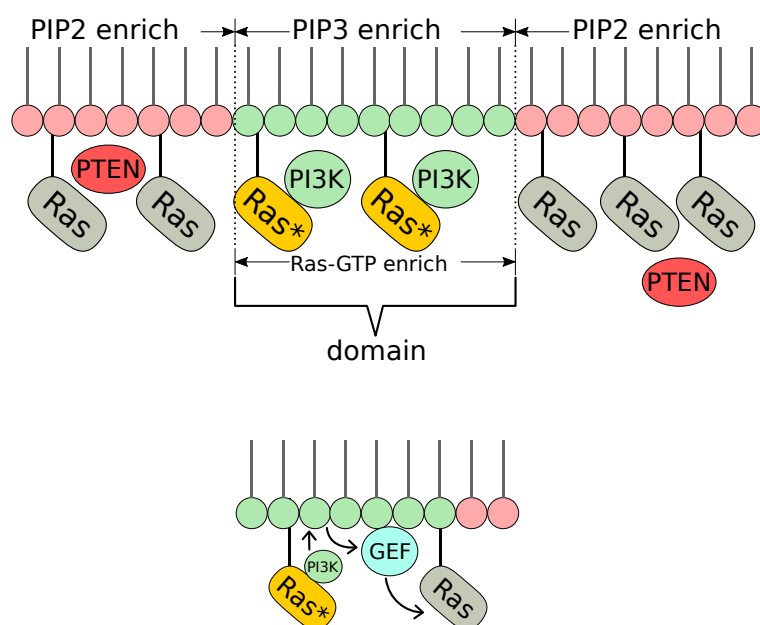
Figure 4.2: Ras-GTP dependent PIP3 domain formation.

.

4.4 Ras wave is dominant in signal transduction symmetry breaking.

PIP3 wave depends on Ras wave, but Ras wave is observed even in *pi3k* null strain (Fig.3.18). Careful observation revealed that only Ras waves were recovered after treatment of LY294002 in spite of no PIP3 wave (Fig.3.23). Additionally, inhibition of TorC2 or PLA2 have no effect on Ras wave. Even inhibited all four major pathways, Ras waves were observed (Fig.3.19 and 3.20). These results indicate Ras wave is independent from downstream four major parallel pathways examined above. Previous studies reported spontaneous Ras activation is seen in trimeric G protein knockout mutants [81], and I demonstrated downstream pathway is not necessary for Ras wave. These results indicate components of Ras wave is the core of excitable dynamics of symmetry breaking.

The number of cells showing Ras wave is reduced in *rasG* null cells while there is no difference between *rasC* null cells and WT cells (Fig.3.22). This means RasG mainly activated in Ras wave; however, there is complemental Ras proteins because some cells lacking RasG still show Ras wave. RasG is known as one of a major mediator of chemotaxis signaling, but the regulation mechanism remains unknown. RasD and RasB were reported that one of the complemtal Ras of RasG [93]. Especially, *rasG* null phenotype was resculed completely by expressing RasD, and partially by expressing RasB. The difference of functions and the meaning of functional overlap remain unclear. It is also unclear how much regulating components and downstream components are shared in Ras family proteins. These problems should be considered to understand Ras regulatory network.

4.5 Modeling of Ras excitable system for Ras/PIP3 wave.

The excitable system is composed of two feedback regulations, fast positive and delayed negative feedbacks. In this study, I assumed five feedback regulations based on the results and estimations from experimental observations (Fig.3.29). Three of them are related to PIP3 signaling and the others are Ras signaling. First is Ras-PI3K-PIP3 positive feedback. The observation in the presence of Latrunculin A revealed that F-actin-independent membrane translocation of PI3K via interaction with Ras-GTP (Fig.3.24). While Ras signaling exhibited the wave pattern without the PI3K activity (Fig.3.18), inhibition of PI3K had an effect on Ras wave stability and Ras excitability (Fig.3.23). These results indicate that there is Ras-PI3K-PIP3 positive feedback regulation. Second is the negative regulation of PTEN by PIP3 as described above, that composes positive feedback regulation for two state switch. Third is PTEN-PIP2 positive feedback. PTEN has a binding site for PIP2 at its N-terminus [63]. That is, cytosolic PTEN binds to the

PIP2-enriched membrane where PTEN catalyzes the further production of PIP2 from PIP3. It was reported that the dissociation rate of PTEN was prolonged on a PIP2 containing membrane, that was confirmed by *In vitro* study using artificial membrane (Yoshioka et al., preparing submission). It remains unclear that this regulation is necessary for the two state switch behavior of PIP3 and PTEN [56][104], but PIP2 binding profile of PTEN is necessary for PTEN proper function. Fourth is positive feedback by mutual inhibition between Ras-GTP and RasGAP, and fifth is delayed negative feedback, that was introduced as a shortage of Ras-GDP. Overall, these feedback mechanisms can produce a local excitation of Ras-GTP, which in turn recruits PI3K to the membrane, leading to the local excitation of PIP3. Intrinsic molecular noise in the system can generate the excitable dynamics spontaneously for random cell migration without external guidance cues.

Ras exhibits excitable dynamics, but the components of the Ras excitable system remains unclear. In this study, I applied the Shibata model to the excitable model of Ras because the Shibata model can well reconstruct many experimental data with minimum components [39][131][133][138]. One of the important regulation is mutual inhibition that composes fast positive feedback. Recently, it was reported that Ras, PI(3,4)P2 and RasGAP2 composed mutually inhibitory feedback regulation [113], that is suitable for the model. An experimental evidence of delayed negative feedback has not been reported. There are roughly two possibilities. One is delayed activation of RasGAP or inactivation of RasGEF after Ras excitation, the other is a shortage of Ras-GDP like the Shibata model. Currently, there is no report about RasGAP and RasGEF regulated in delay timing. It was reported that membrane localization of RasG is regulated by methylation of its isoprenylcysteine, that occurs immediately after cAMP stimulation [98]. It is possible that the regulation of membrane localization of Ras induces shortage of Ras-GDP. However, there is no experimental evidence because protein tagged RasG has some defect in its function that cannot rescue *rasG* strain completely. The molecular components essential for Ras excitability deserve further investigation.

4.6 Ras excitable model in the chemotaxis.

The molecular mechanisms for chemotaxis are evolutionary conserved among various cell types including mammalian neutrophils and *Dictyostelium discoideum*, in which spontaneous cell motility is biased directionally along chemical gradients [23][28][45]. In fact, Ras-GTP- and PIP3 domains are biased directionally under attractant gradients toward the higher concentration even in Latrunculin A treated immobile cells [11][51][32], meaning that chemotactic cells can sense spatial differences in attractants across their cell body. Gradient sensing has been explained theoretically by a local excitation and global inhibition (LEGI) model combined with a signal transduction ex-

citable network (STEN) model [17][21][25][26][29][36][112]. LEGI can detect gradient signals by combining the exciter and the inhibitor, and the output of LEGI is generated at the membrane that faces the higher chemoattractant concentration. STEN works as an amplifier of LEGI output to generate a localized signal in an all-or-none manner [21].

The idea that Ras can be regarded as the core of excitable dynamics, is consistent with LEGI-STEN model. Ras-GTP-enriched domains (Ras domain) can be generated even when impaired the downstream pathways, including PIP3, TorC2, PLA2 and sGC(Fig.3.20), meaning that the Ras regulatory network constitutes the core of the excitable system to generate asymmetric all-or-none signals. At the same time, these signals are stabilized via feedback from downstream pathways [81][111][127]. In addition, several studies provide evidence that chemoattractant receptors and their cognate trimeric G proteins, upstream of Ras, are also unnecessary for spontaneous Ras-GTP accumulation at the leading edge pseudopod in a polarized cell [81]. Thus, the asymmetric Ras signal self-organizes independent of upstream and downstream molecules, but it is biased and stabilized by them. Spatial differences in Ras activity derived from chemoattractant receptors can be amplified in an all-or-none manner along chemical gradients. The internal signals that are generated spontaneously are integrated with external signals derived from the chemoattractant receptors through the spatiotemporal regulations of Ras, leading to biased asymmetric signals along the chemical gradients for chemotaxis.

4.7 For the identification of network structure of Ras excitable system.

Ras small GTPases and the regulatory network make up a complex system comprised of various Ras family proteins, RasGEFs and RasGAPs. In *Dictyostelium discoideum* cells, at least 14 Ras family proteins, 25 RasGEFs, and 14 RasGAPs are estimated from the genome sequence [95] [30]. Our findings here demonstrate that the Ras regulatory network has excitable dynamics, meaning that it has a threshold for excitation. In general, RasGEFs and RasGAPs regulate Ras positively and negatively, respectively. That is, the inputs from RasGEFs and RasGAPs can be regarded as excitatory and inhibitory signals for Ras. These signals are integrated through the regulation of Ras activity and cause excitation when the network exceeds the threshold. This concept is analogous to a neuron in neuronal networks (Fig.4.3), because the neuron has characteristics of an excitable system in which excitatory and inhibitory signals derived from presynaptic cells are integrated in the postsynaptic cell during the signal processing, although the Ras signaling network is spatial communication in a single cell that differs from cell-to-cell communication in a neuronal network. From the viewpoint of molecular signal processing in excitable systems, it is important to clar-

ify the network structure of the Ras regulatory system, which will provide mechanistic insight into cellular decision-making processes. Because Ras and the phosphatidylinositol lipids signaling pathway are involved in onco-genesis and metastasis, understanding the mechanisms that determine and regulate the threshold of the excitable system are important issues in the biological and medical sciences.
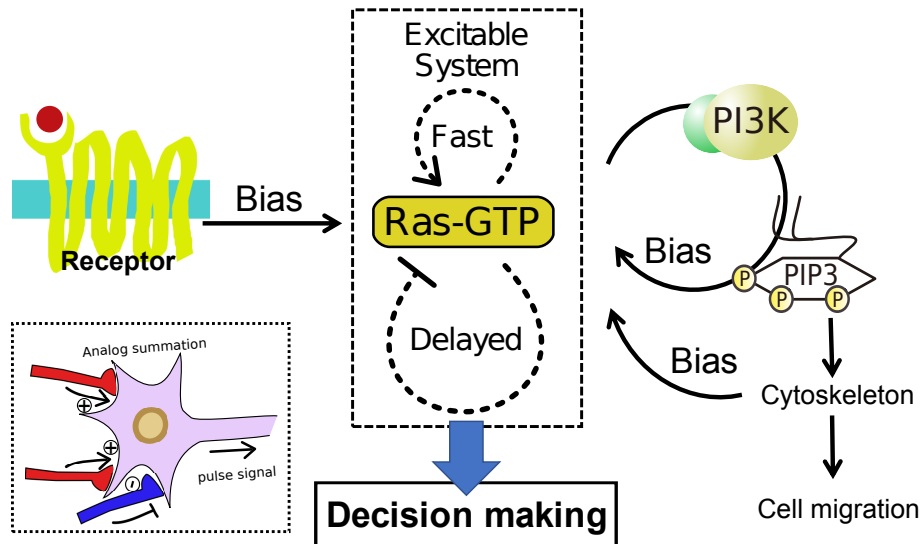

Figure 4.3: Excitable signaling network is one of a fundamental decision making system.

.

4.8   Technical and application aspect of this study.

In this research, it became a breakthrough for discovery that the localization change of PIP2 and PI3K could be observed by high sensitive TIRF microscopy. By using this TIRF, it is possible to detect the localization of proteins with low membrane binding affinity and changes of probes with weak fluorescence or poor dynamic range. The membrane binding properties of molecules are complex due to interaction with lipids and membrane proteins, that is difficult to evaluate accurately with two-hybrid assay or *in vitro* systems because of difference of environments. Besides, it was not possible to evaluate the asymmetric distribution of molecules on a membrane in a single cell. I'm currently analyzing the membrane localization of 25 Ras-GEFs and confirmed that there are periodic changes like a Ras wave in 13 RasGEFs by this method. Only two of them could be detected by the conventional method using confocal microscopy, indicating that the importance of this method. As a variation of this method, it is possible to evaluate the membrane binding affinity of molecules even showing no localization change by measuring the fluorescence intensity ratio between the cytoplasm (by Epi-fluorescence) and the cell membrane (by TIRF) (Degawa et al., preparing submission). These methods are easier than single molecule measurement and useful for an assay because higher throughput can be obtained when evaluating the degree of substantial membrane localization. Of course, it is necessary to consider about other regulation independent of membrane binding affinity like conformation change and complex formation.

Cell polarization in the Ras signaling network is important for the symmetry breaking process of cell migration, that is a fundamentally important function for a cell to create a reaction field in a specific range on a membrane. The study about the cell polarization is expected to be bases for cell manipulation, cell engineering, artificial cell creation and so on. If it is possible to design the spontaneous behaviors of the cell by modulating the nature of the signaling network, it will be a great step in a cell engineering. The signal transduction system of Ras and PIP3 plays a major role in the fundamental functions of cells, such as chemotactic migration and cell division. That is also a focus of attention in the field of medicine because of deep involvement in cellular canceration [141][142][144][149]. To reveal the regulation mechanism of these signal transduction networks is indispensable for understanding of acquisition of migration by a cancer cell, that is a troublesome problem in cancer treatment. At the root of the phenomenon that cells with the same genetic information acquire different movement manner, there is regulation of cell polarization and signaling network, and I hope further research will explain the various behaviors of cancer cells. How do cells, the existences of irregular shapes that move around the microscopic world, decide where to go? Is it controllable by mankind? These questions make and keep us excited.

Bibliography

About Chemotaxis

[1] Konijn, T. M., Van De Meene, J. G., Bonner, J. T., & Barkley, D. S. (1967). The acrasin activity of adenosine-3', 5'-cyclic phosphate. *Proceedings of the National Academy of Sciences*, 58(3), 1152-1154.

[2] Janssens, P. M., & Van Haastert, P. J. (1987). Molecular basis of transmembrane signal transduction in Dictyostelium discoideum. *Microbiological reviews*, 51(4), 396.

[3] Klein, P. S., Sun, T. J., Saxe, C. L., Kimmel, A. R., Johnson, R. L., & Devreotes, P. N. (1988). A chemoattractant receptor controls development in Dictyostelium discoideum. *Science*, 241(4872), 1467-1472.

[4] Devreotes P. N. and Zigmond S. H. (1988). Chemotaxis in Eukaryotic Cells: A Focus on Leukocytes and *Dictyostelium.*, *Annu. Rev. Cell Biol*, 4: 649–86.

[5] Kesbeke, F., HAASTERT, P. J., De Wit, R. J., & Snaar-Jagalska, B. E. (1990). Chemotaxis to cyclic AMP and folic acid is mediated by different G proteins in *Dictyostelium discoideum. Journal of Cell Science*, 96(4), 668-673. was

[6] Saxe III, C. L., Johnson, R., Devreotes, P. N., & Kimmel, A. R. (1991). Multiple genes for cell surface cAMP receptors in *Dictyostelium discoideum. Developmental genetics*, 12(1 - 2), 6-13.

[7] Saxe, C. 3., Ginsburg, G. T., Louis, J. M., Johnson, R., Devreotes, P. N., & Kimmel, A. R. (1993). CAR2, a prestalk cAMP receptor required for normal tip formation and late development of Dictyostelium discoideum. *Genes & Development*, 7(2), 262-272.

[8] Johnson, R. L., Saxe, C. 3., Gollop, R., Kimmel, A. R., & Devreotes, P. N. (1993). Identification and targeted gene disruption of cAR3, a cAMP receptor subtype expressed during multicellular stages of Dictyostelium development.

Genes & development, 7(2), 273-282.

[9] Louis, J. M., Ginsburg, G. T., & Kimmel, A. R. (1994). The cAMP receptor CAR4 regulates axial patterning and cellular differentiation during late development of Dictyostelium. *Genes & Development*, 8(17), 2086-2096.

[10] Parent C. A., Blacklock B. J., Froehlich W. M., Murphy D. B. and Devreotes P. N. (1998). G Protein Signaling Events Are Activated at the Leading Edge of Chemotactic Cells., *Cell*, 95, 81–91.

[11] Parent, C. A., & Devreotes, P. N. (1999). A cell's sense of direction. *Science*, 284(5415), 76570.

[12] Meili, R., Ellsworth, C., Lee, S., Reddy, T. B., Ma, H., & Firtel, R. a. (1999). Chemoattractant-mediated transient activation and membrane localization of Akt/PKB is required for efficient chemotaxis to cAMP in *Dictyostelium. The EMBO Journal*, 18(8), 20922105.

[13] Marcus Thelen. (2001). Dancing to the tune of chemokines., *Nat. Immunol*, 2, 129–134.

[14] Van Haastert PJ. M. and Postma M. (2007). Biased Random Walk by Stochastic Fluctuations of Chemoattractant-Receptor Interactions at the Lower Limit of Detection., *Biophys. J*, 93(5), 1787–1796.

[15] Chen, L., Iijima, M., Tang, M., Landree, M. A., Huang, Y. E., Xiong, Y., ··· Devreotes, P. N. (2007). PLA2 and PI3K/PTEN Pathways Act in Parallel to Mediate Chemotaxis. *Developmental Cell*, 12(4), 603614.

[16] Hoeller, O., & Kay, R. R. (2007). Chemotaxis in the absence of PIP3 gradients. *Current Biology*, 17(9), 813-817.

[17] Xu, X., Meier-Schellersheim, M., Yan, J., & Jin, T. (2007). Locally controlled inhibitory mechanisms are involved in eukaryotic GPCR-mediated chemosensing. *The Journal of cell biology*, 178(1), 141-153.

[18] Takagi H., Sato M. J., Yanagida T. and Ueda M. (2008). Functional analysis of spontaneous cell movement under different physiological conditions., *PLoS ONE*, e2648.

[19] King, J. S., & Insall, R. H. (2009). Chemotaxis: finding the way forward with *Dictyostelium. Trends in Cell Biology*, 19(10), 523530.

[20] Swaney K. F., Huang C. H. and Devreotes P. N. (2010). Eukaryotic Chemotaxis: A Network of Signaling Pathways Controls Motility, Directional Sensing, and Polarity., *Annu. Rev. Biophys*, 39, 265–289.

[21] Xiong, Y., Huang, C.-H., Iglesias, P. A., & Devreotes, P. N. (2010). Cells navigate with a local-excitation, global-inhibition-biased excitable network. *Proc. Natl. Acad. Sci. U.S.A.*, 107, 17079–17086.

[22] Lee, S., Shen, Z., Robinson, D. N., Briggs, S., & Firtel, R. A. (2010). Involvement of the cytoskeleton in controlling leading-edge function during chemotaxis. *Molecular biology of the cell*, 21(11), 1810-1824.

[23] Iglesias, P. A., & Devreotes, P. N. (2012). Biased excitable networks: How cells direct motion in response to gradients. *Current Opinion in Cell Biology*, 24(2), 245253.

[24] Huang C. H., Tang M., Shi C., Iglesias P. A. and Devreotes P. N. (2013). An excitable signal integrator couples to an idling cytoskeletal oscillator to drive cell migration. *Nat. Cell Biol*, 15(11), 1307–16.

[25] Levine, H., & Rappel, W. J. (2013). The physics of eukaryotic chemotaxis. *Physics today*, 66(2).

[26] Jin, T. (2013). Gradient sensing during chemotaxis. *Current opinion in cell biology*, 25(5), 532-537.

[27] Shi, C., & Iglesias, P. A. (2013). Excitable behavior in amoeboid chemotaxis. *Wiley Interdisciplinary Reviews: Systems Biology and Medicine*, 5(5), 631-642.

[28] Tang M, Wang M., Shi C, Iglesias P. A., Devreotes P. N. and Huang C. H. (2014). Evolutionarily conserved coupling of adaptive and excitable networks mediates eukaryotic chemotaxis, *Nat. Commun*, 5, 5175.

[29] Nakajima, A., Ishihara, S., Imoto, D., & Sawai, S. (2014). Rectified directional sensing in long-range cell migration. *Nature communications*, 5, 5367.

[30] Artemenko, Y., Lampert, T. J., and Devreotes, P. N. (2014). Moving Toward a Paradigm L Common Mechanism of Chemotactic Signaling in Dyctyostelium and Mammalian Leukocytes. *Cell Mol Life Sci*, 71(19), 37113747.

[31] Graziano, B. R., & Weiner, O. D. (2014). Self-organization of protrusions and polarity during eukaryotic chemotaxis. *Current opinion in cell biology*, 30, 60-67.

[32] Collins, S. R., Yang, H. W., Bonger, K. M., Guignet, E. G., Wandless, T. J., & Meyer, T. (2015). Using light to shape chemical gradients for parallel and automated analysis of chemotaxis. *Molecular Systems Biology*, 11(4), 804.

[33] Nichols, J. M., Veltman, D., & Kay, R. R. (2015). Chemotaxis of a model organism: progress with Dictyostelium. *Current opinion in cell biology*, 36, 7-12.

[34] Veltman, D. M., Williams, T. D., Bloomfield, G., Chen, B. C., Betzig, E., Insall, R. H., & Kay, R. R. (2016). A plasma membrane template for macropinocytic cups. *Elife*, 5, e20085.

[35] Pan, M., Xu, X., Chen, Y., & Jin, T. (2016). Identification of a chemoattractant G-protein-coupled receptor for folic acid that controls both chemotaxis and phagocytosis. *Developmental cell*, 36(4), 428-439.

[36] Devreotes, P. N., Bhattacharya, S., Edwards, M., Iglesias, P. A., Lampert, T., & Miao, Y. (2017). Excitable Signal Transduction Networks in Directed Cell Migration. *Annual Review of Cell and Developmental Biology*, 33(1), 103125.

About Ras/PIP3 signaling

[37] Comer F. I., Parent C. A. (2002). PI 3-Kinases and PTEN: How Opposites Chemoattract., *Cell*, 109, 541–544.

[38] Weiner, O. D., Marganski, W. A., Wu, L. F., Altschuler, S. J., & Kirschner, M. W. (2007). An actin-based wave generator organizes cell motility. *PLoS biology*, 5(9), e221.

[39] Arai Y., Shibata T., Matsuoka S., Sato M. J., Yanagida T. and Ueda M. (2010). Self-organization of the phosphatidylinositol lipids signaling for random cell migration., *Proc. Natl. Acad. Sci. U.S.A.*, 107, 12399–12404.

[40] Gerisch G., Ecke M., Wischnewski D. and Schroth-Diez B. (2011). Different modes of state transitions determine pattern in the Phosphatidylinositide-Actin system., *BMC Cell Biol*, 12, 42.

[41] Gerisch, G., Schroth-Diez, B., Mller-Taubenberger, A. and Ecke, M. (2012). PIP3 waves and PTEN dynamics in the emergence of cell polarity., *Biophys.*

J., 103, 11701178.

[42] Nishikawa M., Hörning M., Ueda M. and Shibata T. (2014). Excitable Signal Transduction Induces Both Spontaneous and Directional Cell Asymmetries in the Phosphatidylinositol Lipid Signaling System for Eukaryotic Chemotaxis., *Biophys. J*, 106, 723–734.

[43] Takeda K., Shao D., Adler M., Charest P. G., Loomis W. F., Levine H., Groisman A., Rappel W. J. and Firtel R. A. (2014). Incoherent Feedforward Control Governs Adaptation of Activated Ras in a Eukaryotic Chemotaxis Pathway., *Sci. Signal*, 5, 205.

[44] Lange, M., Prassler, J., Ecke, M., Mller-Taubenberger, A., & Gerisch, G. (2016). Local Ras activation, PTEN pattern, and global actin flow in the chemotactic responses of oversized cells. *Journal of Cell Science*, 129(18), 34623472.

[45] Miao, Y., Bhattacharya, S., Edwards, M., Cai, H., Inoue, T., Iglesias, P. A., & Devreotes, P. N. (2017). Altering the threshold of an excitable signal transduction network changes cell migratory modes. *Nature Cell Biology*, 19(4), 329340.

[46] Insall, R., Kuspa, A., Lilly, P. J., Shaulsky, G., Levin, L. R., Loomis, W. F., & Devreotes, P. (1994). CRAC, a cytosolic protein containing a pleckstrin homology domain, is required for receptor and G protein-mediated activation of adenylyl cyclase in Dictyostelium. *The Journal of Cell Biology*, 126(6), 1537-1545.

[47] Lilly, P. J., & Devreotes, P. N. (1995). Chemoattractant and GTP gamma S-mediated stimulation of adenylyl cyclase in Dictyostelium requires translocation of CRAC to membranes. *The Journal of cell biology*, 129(6), 1659-1665.

[48] Garcia P., Gupta R., Shah S., Morris A. J., Rudge S. A., Scarlata S., Petrova V., McLaughlin S. and Rebecchi MJ. (1995). The pleckstrin homology domain of phospholipase C-delta 1 binds with high affinity to phosphatidylinositol 4,5-bisphosphate in bilayer membranes., *Biochemistry*, 34(49), 16228–34.

[49] Stauffer, T. P., Ahn, S., & Meyer, T. (1998). Receptor-induced transient reduction in plasma membrane PtdIns (4, 5) P2 concentration monitored in living cells. *Current Biology*, 8(6), 343-346.

[50] Servant, G., Weiner, O. D., Herzmark, P., Balla, T., Sedat, J. W., & Bourne, H. R. (2000). Polarization of chemoattractant receptor signaling during neutrophil chemotaxis. *Science*, 287(5455), 1037-1040.

[51] Janetopoulos, C., Ma, L., Devreotes, P. N., & Iglesias, P. A. (2004). Chemoattractant-induced phosphatidylinositol 3,4,5-trisphosphate accumulation is spatially amplified and adapts, independent of the actin cytoskeleton. *Proc. Natl. Acad. Sci. U.S.A.*, 101(24), 89516.

[52] Dormann, D., Weijer, G., Dowler, S., & Weijer, C. J. (2004). In vivo analysis of 3-phosphoinositide dynamics during Dictyostelium phagocytosis and chemotaxis. *Journal of cell science*, 117(26), 6497-6509.

[53] Vincent P., Chua M., Nogue F., Fairbrother A., Mekeel H., Xu Y., Allen N., Bibikova T. N., Gilroy S. and Bankaitis V. A. (2005). A Sec14p-nodulin domain phosphatidylinositol transfer protein polarizes membrane growth of Arabidopsis thaliana root hairs., *J. Cell Biol*, 168(5), 801–12.

[54] Vrnai, P., & Balla, T. (2006). Live cell imaging of phosphoinositide dynamics with fluorescent protein domains. *Biochimica et Biophysica Acta (BBA)-Molecular and Cell Biology of Lipids*, 1761(8), 957-967.

[55] Matsuoka S., Iijima M., Watanabe T. M., Kuwayama H., Yanagida T., Devreotes P. N. and Ueda M. (2006). Single molecule analysis of chemoattractant-stimulated membrane recruitment of a PH domain-containing protein., *J. Cell. Sci*, 119, 1071–1079.

[56] Kortholt, A., King, J. S., Keizer-Gunnink, I., Harwood, A. J., & Van Haastert, P. J. (2007). Phospholipase C regulation of phosphatidylinositol 3, 4, 5-trisphosphate-mediated chemotaxis. *Molecular biology of the cell*, 18(12), 4772-4779.

[57] Mark A. Lemmon. (2007). Pleckstrin Homology (PH) domains and phosphoinositides., *Biochem. Soc. Symp*, 74, 81–93.

[58] Park, W. S., Do Heo, W., Whalen, J. H., O'Rourke, N. A., Bryan, H. M., Meyer, T., & Teruel, M. N. (2008). Comprehensive identification of PIP3-regulated PH domains from C. elegans to H. sapiens by model prediction and live imaging. *Molecular cell*, 30(3), 381-392.

[59] Knight, J. D., & Falke, J. J. (2009). Single-molecule fluorescence studies of a PH domain: new insights into the membrane docking reaction. *Biophysical journal*, 96(2), 566-582.

[60] Fets, L., Nichols, J. M. E., & Kay, R. R. (2014). A PIP5 kinase essential for efficient chemotactic signaling. *Current Biology*, 24(4), 415421.

[61] Ghosh, R., de Campos, M. K. F., Huang, J., Huh, S. K., Orlowski, A., Yang, Y., ⋯ Bankaitis, V. A. (2015). Sec14-nodulin proteins and the patterning of phosphoinositide landmarks for developmental control of membrane morphogenesis. *Molecular Biology of the Cell*, 26(9), 17641781.

[62] Iijima, M., & Devreotes, P. (2002). Tumor suppressor PTEN mediates sensing of chemoattractant gradients. *Cell*, 109(5), 599610.

[63] Iijima, M., Huang, Y. E., Luo, H. R., Vazquez, F., & Devreotes, P. N. (2004). Novel Mechanism of PTEN Regulation by Its Phosphatidylinositol 4,5-Bisphosphate Binding Motif Is Critical for Chemotaxis. *J. Biol. Chem*, 279(16), 1660616613.

[64] Schmid, A. C., Byrne, R. D., Vilar, R., & Woscholski, R. (2004). Bisperoxovanadium compounds are potent PTEN inhibitors. *FEBS letters*, 566(1-3), 35-38.

[65] Rosivatz, E., Matthews, J. G., McDonald, N. Q., Mulet, X., Ho, K. K., Lossi, N., ... & Lam, E. W. F. (2006). A small-molecule inhibitor for phosphatase and tensin homologue deleted on chromosome 10 (PTEN). *ACS chemical biology*, 1(12), 780-790.

[66] Iijima M. and Devreotes P. N. (2006). Tumor Suppressor PTEN Mediates Sensing of Chemoattractant Gradients., *Cell*, 109(5), 599–610.

[67] Pramanik M. K., Iijima M., Iwadate Y. and Yumura S. (2009). PTEN is a mechanosensing signal transducer for myosin II localization in *Dictyostelium* cells., *Genes Cells*, 14(7), 821–34.

[68] Mak, L. H., Vilar, R., & Woscholski, R. (2010). Characterisation of the PTEN inhibitor VO-OHpic. *Journal of chemical biology*, 3(4), 157-163.

[69] Li, Y., Prasad, A., Jia, Y., Roy, S. G., Loison, F., Mondal, S., ... & Luo, H. R. (2011). Pretreatment with phosphatase and tensin homolog deleted on chromosome 10 (PTEN) inhibitor SF1670 augments the efficacy of granulocyte transfusion in a clinically relevant mouse model. *Blood*, 117(24), 6702-6713.

[70] Matsuoka S., Shibata T. and Ueda M. (2013). Asymmetric PTEN Distribution Regulated by Spatial Heterogeneity in Membrane-Binding State Transitions., *PLoS Comput. Biol*, e1002862.

[71] Nguyen, H. N., Afkari, Y., Senoo, H., Sesaki, H., Devreotes, P. N., & Iijima, M. (2014). Mechanism of human PTEN localization revealed by heterologous

expression in *Dictyostelium.*, *Oncogene*, 33(50), 5688–96.

[72] Matsuoka, S., & Ueda, M. (2018). Mutual inhibition between PTEN and PIP3 generates bistability for polarity in motile cells. *Nature communications*, 9(1), 4481.

[73] Zhou K., Takegawa K., Emr S. D. and Firtel R. A. (1995). A phosphatidylinositol (PI) kinase gene family in *Dictyostelium discoideum*: biological roles of putative mammalian p110 and yeast Vps34p PI 3-kinase homologs during growth and development., *Mol. Cell. Biol*, 10, 5645–56.

[74] Funamoto, S., Milan, K., Meili, R., & Firtel, R. A. (2001). Role of Phosphatidylinositol 3´ Kinase and a Downstream Pleckstrin Homology Domain-Containing Protein in Controlling Chemotaxis in *Dictyostelium. The Journal of Cell Biology*, 153(4), 795810.

[75] Funamoto S., Meili R., Lee S., Parry L. and Firtel R. A. (2002). Spatial and temporal regulation of 3-phosphoinositides by PI 3-kinase and PTEN mediates chemotaxis., *Cell*, 109, 611–623.

[76] Huang Y. E., Iijima M., Parent C. A., Funamoto S., Firtel R. A. and Devreotes P. (2003). Receptor-mediated regulation of PI3Ks confines PI(3,4,5)P3 to the leading edge of chemotaxing cells., *Mol. Cell. Biol*, 14(5), 1913–22.

[77] Sasaki A. T., Chun C., Takeda K. and Firtel R. A. (2004). Localized Ras signaling at the leading edge regulates PI3K, cell polarity, and directional cell movement., *J. Cell Biol*, 167(3), 505–18.

[78] Postma, M., Roelofs, J., Goedhart, J., Loovers, H. M., Visser, A. J., & Van Haastert, P. J. (2004). Sensitization of Dictyostelium chemotaxis by phosphoinositide-3-kinase-mediated self-organizing signalling patches. *Journal of cell science*, 117(14), 2925-2935.

[79] Loovers, H. M., Postma, M., Keizer-Gunnink, I., Huang, Y. E., Devreotes, P. N., & van Haastert, P. J. M. (2006). Distinct roles of PI(3,4,5)P3 during chemoattractant signaling in *Dictyostelium*: a quantitative in vivo analysis by inhibition of PI3-kinase. *Molecular Biology of the Cell*, 17(4), 150313.

[80] Takeda, K., Sasaki, A. T., Ha, H., Seung, H. A., & Firtel, R. A. (2007). Role of phosphatidylinositol 3-kinases in chemotaxis in *Dictyostelium. Journal of Biological Chemistry*, 282(16), 1187411884.

[81] Sasaki A. T., Janetopoulos C., Lee S., Charest P. G., Takeda K., Sundheimer L. W. (2007). Meili R., Devreotes P. N. and Firtel R. A., G protein-independent Ras/PI3K/F-actin circuit regulates basic cell motility., *J. Cell Biol*, 178, 185–91.

[82] Bosgraaf, L., Keizer-Gunnink, I., & Van Haastert, P. J. M. (2008). PI3-kinase signaling contributes to orientation in shallow gradients and enhances speed in steep chemoattractant gradients. *Journal of Cell Science*, 121(21), 35893597.

[83] Weiger, M. C., Wang, C.-C., Krajcovic, M., Melvin, A. T., Rhoden, J. J., & Haugh, J. M. (2009). Spontaneous phosphoinositide 3-kinase signaling dynamics drive spreading and random migration of fibroblasts. *Journal of Cell Science*, 122(Pt 3), 313323.

[84] Reymond, C. D., Gomer, R. H., Mehdy, M. C., & Firtel, R. A. (1984). Developmental regulation of a Dictyostelium gene encoding a protein homologous to mammalian ras protein. *Cell*, 39(1), 141-148.

[85] Pawson, T., Amiel, T., Hinze, E., Auersperg, N., Neave, N., Sobolewski, A., & Weeks, G. (1985). Regulation of a ras-related protein during development of Dictyostelium discoideum. *Molecular and cellular biology*, 5(1), 33-39.

[86] Reymond, C. D., Gomer, R. H., Nellen, W., Theibert, A., Devreotes, P., & Firtel, R. A. (1986). Phenotypic changes induced by a mutated ras gene during the development of Dictyostelium transformants. *Nature*, 323(6086), 340.

[87] Daniel, J., Spiegelman, G. B., & Weeks, G. (1993). Characterization of a third ras gene, rasB, that is expressed throughout the growth and development of Dictyostelium discoideum. *Oncogene*, 8(4), 1041-1047.

[88] Boguski, M. S., & McCormick, F. (1993). Proteins regulating Ras and its relatives. *Nature*, 366(6456), 643.

[89] Daniel, J., Bush, J., Cardelli, J., Spiegelman, G. B., & Weeks, G. (1994). Isolation of two novel ras genes in Dictyostelium discoideum; evidence for a complex, developmentally regulated ras gene subfamily. *Oncogene*, 9(2), 501-508.

[90] Lee S., Escalante R. and Firtel R. A. (1997). A Ras GAP is essential for cytokinesis and spatial patterning in *Dictyostelium.*, *Development*, 124(5), 983–96.

[91] Tuxworth, R. I., Cheetham, J. L., Machesky, L. M., Spiegelmann, G. B., Weeks, G., & Insall, R. H. (1997). *Dictyostelium* RasG is required for normal

motility and cytokinesis, but not growth. *The Journal of cell biology*, 138(3), 605-614.

[92] Lee, S., Parent, C. A., Insall, R., & Firtel, R. A. (1999). A novel Ras-interacting protein required for chemotaxis and cyclic adenosine monophosphate signal relay in *Dictyostelium*. *Molecular Biology of the Cell*, 10(9), 2829-2845.

[93] Khosla, M., Spiegelman, G. B., Insall, R., & Weeks, G. (2000). Functional overlap of the Dictyostelium RasG, RasD and RasB proteins. *J Cell Sci*, 113(8), 1427-1434.

[94] Lim, C. J., Spiegelman, G. B., & Weeks, G. (2002). Cytoskeletal regulation by *Dictyostelium* Ras subfamily proteins. *Journal of Muscle Research and Cell Motility*, 23(78), 729736.

[95] Wilkins, A., Szafranski, K., Fraser, D. J., Bakthavatsalam, D., Mller, R., Fisher, P. R., ⋯ Insall, R. H. (2005). The *Dictyostelium* genome encodes numerous RasGEFs with multiple biological roles. *Genome Biology*, 6(8), R68.

[96] Bolourani, P., Spiegelman, G. B., & Weeks, G. (2006). Delineation of the roles played by RasG and RasC in cAMP-dependent signal transduction during the early development of *Dictyostelium discoideum*. *Molecular Biology of the Cell*, 17(10), 454350.

[97] Kae, H., Kortholt, A., Rehmann, H., Insall, R. H., Van Haastert, P. J. M., Spiegelman, G. B., & Weeks, G. (2007). Cyclic AMP signalling in *Dictyostelium*: G-proteins activate separate Ras pathways using specific RasGEFs. *EMBO Reports*, 8(5), 47782.

[98] Chen, Y., McQuade, K. J., Guan, X. J., Thomason, P. A., Wert, M. S., Stock, J. B., & Cox, E. C. (2007). Isoprenylcysteine carboxy methylation is essential for development in Dictyostelium discoideum. *Molecular biology of the cell*, 18(10), 4106-4118.

[99] Zhang S., Charest P. G. and Firtel R. A. (2008). Spatiotemporal regulation of Ras activity provides directional sensing., *Curr. Biol*, 18(20), 1587–93.

[100] Bolourani, P., Spiegelman, G. B., & Weeks, G. (2008). Rap1 activation in response to cAMP occurs downstream of ras activation during Dictyostelium aggregation. *Journal of Biological Chemistry*, 283(16), 10232-10240.

[101] Kortholt, A., & van Haastert, P. J. M. (2008). Highlighting the role of Ras and Rap during *Dictyostelium* chemotaxis. *Cellular Signalling*, 20(8), 14151422.

[102] Kortholt, A., Kataria, R., Keizer-Gunnink, I., Egmond, W. N. Van, Khanna, A., Van Haastert, P. J. M., ⋯ Van Haastert, P. J. M. (2011). *Dictyostelium* chemotaxis: essential Ras activation and accessory signalling pathways for amplification. *EMBO Reports*, 12(12), 17.

[103] Kortholt, A., Keizer-Gunnink, I., Kataria, R., & Van Haastert, P. J. M. (2013). Ras activation and symmetry breaking during *Dictyostelium* chemotaxis. *Journal of Cell Science*, 126(Pt 19), 450213.

[104] Srinivasan, K., Wright, G. A., Hames, N., Housman, M., Roberts, A., Aufderheide, K. J., & Janetopoulos, C. (2013). Delineating the core regulatory elements crucial for directed cell migration by examining folic-acid-mediated responses. *Journal of Cell Science*, 126(1), 221233.

[105] Wang, Y., Senoo, H., Sesaki, H., & Iijima, M. (2013). Rho GTPases orient directional sensing in chemotaxis. *Proceedings of the National Academy of Sciences*, 110(49), E4723-E4732.

[106] Plak, K., Keizer-Gunnink, I., van Haastert, P. J., & Kortholt, A. (2014). Rap1-dependent pathways coordinate cytokinesis in Dictyostelium. *Molecular biology of the cell*, 25(25), 4195-4204.

[107] Chattwood A., Bolourani P. and Weeks G. (2014). RasG signaling is important for optimal folate chemotaxis in *Dictyostelium.*, *BMC Cell Biol*, 15, 13.

[108] Bloomfield, G., Traynor, D., Sander, S. P., Veltman, D. M., Pachebat, J. A., & Kay, R. R. (2015). Neurofibromin controls macropinocytosis and phagocytosis in Dictyostelium. *Elife*, 4, e04940.

[109] Inaba, H., Yoda, K., & Adachi, H. (2017). The F-actin-binding RapGEF GflB is required for efficient macropinocytosis in Dictyostelium. *J Cell Sci*, jcs-194126.

[110] Ecke, M., & Gerisch, G. (2017). Co-existence of Ras activation in a chemotactic signal transduction pathway and in an autonomous wave-forming system. *Small GTPases*, 1-9.

[111] van Haastert, P. J. M., Keizer-Gunnink, I., & Kortholt, A. (2017). Coupled excitable Ras and F-actin activation mediates spontaneous pseudopod formation and directed cell movement. *Molecular Biology of the Cell*, 28(7), 922934.

[112] Xu, X., Wen, X., Veltman, D. M., Keizer-Gunnink, I., Pots, H., Kortholt, A., & Jin, T. (2017). GPCR-controlled membrane recruitment of negative regulator C2GAP1 locally inhibits Ras signaling for adaptation and long-range chemotaxis. *Proc. Natl. Acad. Sci. U.S.A.*, 114(47), E10092E10101.

[113] Li, X., Edwards, M., Swaney, K. F., Singh, N., Bhattacharya, S., Borleis, J., ... & Devreotes, P. N. (2018). Mutually inhibitory Ras-PI (3, 4) P2 feedback loops mediate cell migration. *Proceedings of the National Academy of Sciences*, 115(39), E9125-E9134.

[114] Edwards, M., Cai, H., Abubaker-Sharif, B., Long, Y., Lampert, T. J., & Devreotes, P. N. (2018). Insight from the maximal activation of the signal transduction excitable network in Dictyostelium discoideum. *Proceedings of the National Academy of Sciences*, 115(16), E3722-E3730.

[115] Liu, G., & NEWELL, P. C. (1988). Evidence that cyclic GMP regulates myosin interaction with the cytoskeleton during chemotaxis of Dictyostelium. *Journal of Cell Science*, 90(1), 123-129.

[116] Darcy, P. K., Wilczynska, Z., & Fisher, P. R. (1994). The role of cGMP in photosensory and thermosensory transduction in Dictyostelium discoideum. *Microbiology*, 140(7), 1619-1632.

[117] Veltman, D. M., Roelofs, J., Engel, R., Visser, A. J., & Van Haastert, P. J. (2005). Activation of soluble guanylyl cyclase at the leading edge during *Dictyostelium* chemotaxis. *Molecular biology of the cell*, 16(2), 976-983.

[118] Bosgraaf, L., Waijer, A., Engel, R., Visser, A. J., Wessels, D., Soll, D., & van Haastert, P. J. (2005). RasGEF-containing proteins GbpC and GbpD have differential effects on cell polarity and chemotaxis in *Dictyostelium. Journal of cell science*, 118(9), 1899-1910.

[119] Veltman, D. M., & Van Haastert, P. J. (2006). Guanylyl cyclase protein and cGMP product independently control front and back of chemotaxing *Dictyostelium* cells. *Molecular biology of the cell*, 17(9), 3921-3929.

[120] Chen, L., Iijima, M., Tang, M., Landree, M. A., Huang, Y. E., Xiong, Y., ··· Devreotes, P. N. (2007). PLA2 and PI3K/PTEN Pathways Act in Parallel to Mediate Chemotaxis. *Developmental Cell*, 12(4), 603614.

[121] Kamimura, Y., Xiong, Y., Iglesias, P. A., Hoeller, O., Bolourani, P., & Devreotes, P. N. (2008). PIP3-independent activation of TorC2 and PKB at the cell's leading edge mediates chemotaxis. *Current Biology*, 18(14), 1034-1043.

[122] Veltman, D. M., Keizer-Gunnik, I., & Van Haastert, P. J. M. (2008). Four key signaling pathways mediating chemotaxis in *Dictyostelium discoideum*. *Journal of Cell Biology*, 180(4), 747753.

[123] Bosgraaf, L., & Van Haastert, P. J. (2009). Navigation of chemotactic cells by parallel signaling to pseudopod persistence and orientation. PloS one, 4(8), e6842.

[124] Kamimura, Y., Cai, H., & Devreotes, P. N. (2010). TORC2 and chemotaxis in *Dictyostelium discoideum*. Enzymes (1st ed., Vol. 28). *Elsevier Inc.*

[125] Liao, X. H., Buggey, J., & Kimmel, A. R. (2010). Chemotactic activation of *Dictyostelium* AGC-family kinases AKT and PKBR1 requires separate but coordinated functions of PDK1 and TORC2. *J Cell Sci*, 123(6), 983-992.

[126] Khanna, A., Lotfi, P., Chavan, A. J., Montao, N. M., Bolourani, P., Weeks, G., ... & Kortholt, A. (2016). The small GTPases Ras and Rap1 bind to and control TORC2 activity. *Scientific reports*, 6, 25823.

[127] Scavello, M., Petlick, A. R., Ramesh, R., Thompson, V. F., Lotfi, P., & Charest, P. G. (2017). Protein Kinase A regulates the Ras, Rap1, and TORC2 pathways in response to the chemoattractant cAMP in Dictyostelium. *J Cell Sci*, jcs-177170.

[128] Tanabe, Y., Kamimura, Y., & Ueda, M. (2018). Parallel signaling pathways regulate excitable dynamics differently for pseudopod formation in eukaryotic chemotaxis. *J Cell Sci*, jcs-214775.

[129] Meinhardt, H. (1999). Orientation of chemotactic cells and growth cones: models and mechanisms. *J Cell Sci*, 112(17), 2867-2874.

[130] Altschuler, S. J., Angenent, S. B., Wang, Y., & Wu, L. F. (2008). On the spontaneous emergence of cell polarity. *Nature*, 454(7206), 886.

[131] Shibata T., Nishikawa M., Matsuoka S. and Ueda M. (2012). Modeling the self-organized phosphatidylinositol lipid signaling system in chemotactic cells using quantitative image analysis., *J. Cell. Sci*, 125, 5138–5150.

[132] Semplice, M., Veglio, A., Naldi, G., Serini, G., & Gamba, A. (2012). A bistable model of cell polarity. *PloS one*, 7(2), e30977.

[133] Shibata T., Nishikawa M., Matsuoka S. and Ueda M. (2013). Intracellular encoding of spatiotemporal guidance cues in a self-organizing signaling system for chemotaxis in *Dictyostelium* cells., *Biophys. J.*, 105(9), 2199-2209.

[134] Taniguchi D., Ishihara S., Oonuki T., Honda-Kitahara M., Kaneko K. and Sawai S. (2013). Phase geometries of two-dimensional excitable waves govern self-organized morphodynamics of amoeboid cells., *Proc. Natl. Acad. Sci. U.S.A.*, 110, 5016–5021.

[135] Goehring, N. W., & Grill, S. W. (2013). Cell polarity: mechanochemical patterning. *Trends in cell biology*, 23(2), 72-80.

[136] Knoch, F., Tarantola, M., Bodenschatz, E., & Rappel, W.-J. (2014). Modeling self-organized spatio-temporal patterns of PIP3 and PTEN during spontaneous cell polarization. *Phys. Biol*, 11, 046002.

[137] Rappel, W. J., & Edelstein-Keshet, L. (2017). Mechanisms of cell polarization. Current opinion in systems biology, 3, 43-53.

[138] Hrning M., & Shibata T. (2018), Three-dimensional cell geometry controls excitable membrane signaling in Dictyotelium cells. *bioRxiv*, doi: https://doi.org/10.1101/278853

Insight from mammalian cells

[139] Xu, G., O'Connell, P., Viskochil, D., Cawthon, R., Robertson, M., Culver, M., ... & Weiss, R. (1990). The neurofibromatosis type 1 gene encodes a protein related to GAP. *Cell*, 62(3), 599-608.

[140] Pacold M. E., Suire S., Perisic O., Lara-Gonzalez S., Davis C. T., Walker E. H., Hawkins P. T., Stephens L., Eccleston J. F. and Williams R. L. (2000). Crystal structure and functional analysis of Ras binding to its effector phosphoinositide 3-kinase gamma., *Cell*, 103(6), 931–43.

[141] Kang, S., Bader, A. G., & Vogt, P. K. (2005). Phosphatidylinositol 3-kinase mutations identified in human cancer are oncogenic. *Proceedings of the National Academy of Sciences*, 102(3), 802-807.

[142] Condeelis J., Singer R. H. and Segall J. E. (2005). THE GREAT ESCAPE: When Cancer Cells Hijack the Genes for Chemotaxis and Motility., *Annu. Rev. Cell Dev. Biol*, 21, 695–718.

[143] Vazquez F., Matsuoka S., Sellers W. R., Yanagida T., Ueda M. and Devreotes P. N. (2006). Tumor suppressor PTEN acts through dynamic interaction with the plasma membrane., *Proc. Natl. Acad. Sci. U.S.A.*, 103, 3633–3638.

[144] Yuan, T. L., & Cantley, L. C. (2008). PI3K pathway alterations in cancer: variations on a theme. *Oncogene*, 27(41), 5497.

[145] Leslie N. R., Batty I. H., Maccario H., Davidson L. and Downes C. P. (2008). Understanding PTEN regulation: PIP2, polarity and protein stability., *Oncogene*, 27(41), 5464–76.

[146] Yoo, S. K., Deng, Q., Cavnar, P. J., Wu, Y. I., Hahn, K. M., & Huttenlocher, A. (2010). Differential Regulation of Protrusion and Polarity by PI(3)K during Neutrophil Motility in Live Zebrafish. *Developmental Cell*, 18(2), 226236.

[147] Lumb C. N. and Sansom M. S. (2013). Defining the membrane-associated state of the PTEN tumor suppressor protein., *Biophys. J*, 04(3), 613–21.

[148] Kalli A. C., Devaney I. and Sansom M. S. (2014). Interactions of phosphatase and tensin homologue (PTEN) proteins with phosphatidylinositol phosphates: insights from molecular dynamics simulations of PTEN and voltage sensitive phosphatase., *Biochemistry*, 53(11), 1724–32.

[149] Stephen, A. G., Esposito, D., Bagni, R. K., & McCormick, F. (2014). Dragging ras back in the ring. *Cancer cell*, 25(3), 272-281.

[150] Xiong, D., Xiao, S., Guo, S., Lin, Q., Nakatsu, F., & Wu, M. (2016). Frequency and amplitude control of cortical oscillations by phosphoinositide waves. *Nature Chemical Biology*, 12(3), 159166.

[151] Yang, H. W., Collins, S. R., & Meyer, T. (2016). Locally excitable Cdc42 signals steer cells during chemotaxis. *Nature Cell Biology*, 18(2), 191201.

About Single-molecule Imaging

[152] Michael J. Saxton and Ken Jacobson. (1997). SINGLE-PARTICLE TRACKING: Applications to Membrane Dynamics., *Annu. Rev. Biophys. Biomol. Struct*, 26, 373–399.

[153] Sako Y., Minoghchi S. and Yanagida T. (2000). Single-molecule imaging of EGFR signalling on the surface of living cells., *Nat. Cell Biol*, 2(3), 168–72.

[154] Daniel Axelrod. (2001). Total Internal Reflection Fluorescence Microscopy in Cell Biology., *Traffic*, 11, 764–774.

[155] Ueda M., Sako Y., Tanaka T., Devreotes P. and Yanagida T. (2001). Single-molecule analysis of chemotactic signaling in *Dictyostelium* cells., *Science*, 294(5543), 864–7.

[156] Matsuoka S., Shibata T. and Ueda M. (2009). Statistical analysis of lateral diffusion and multistate kinetics in single-molecule imaging., *Biophys. J*, 97, 1115–1124.

About Excitable dynamics

[157] Hodgkin, A. L., & Huxley, A. F. (1952). A quantitative description of membrane current and its application to conduction and excitation in nerve. *Bulletin of Mathematical Biology*, 52(12), 2571.

[158] Krahe, R., & Gabbiani, F. (2004). Burst firing in sensory systems. *Nature Reviews Neuroscience*, 5(1), 1323.

[159] Lindner, B., Garca-Ojalvo, J., Neiman, A., & Schimansky-Geier, L. (2004). Effects of noise in excitable systems. *Physics Reports*, 392(6), 321424.

[160] Karsenti, E. (2008). Self-organization in cell biology: a brief history. *Nature Reviews Molecular Cell Biology*, 9(3), 255262.

[161] Eldar, A., & Elowitz, M. B. (2010). Functional roles for noise in genetic circuits. *Nature*, 467(7312), 167173.

[162] Loewer, A., Batchelor, E., Gaglia, G., & Lahav, G. (2010). Basal Dynamics of p53 Reveal Transcriptionally Attenuated Pulses in Cycling Cells. *Cell*, 142(1), 89100.

[163] Norman, T. M., Lord, N. D., Paulsson, J., & Losick, R. (2015). Stochastic Switching of Cell Fate in Microbes. *Annual Review of Microbiology*, 69(1), 381403.

[164] Mnke, G., Cristiano, E., Finzel, A., Friedrich, D., Herzel, H., Falcke, M., & Loewer, A. (2017). Excitability in the p53 network mediates robust signaling with tunable activation thresholds in single cells. *Scientific Reports*, 7(March), 46571.

Others

[165] Watts, D. J., & Ashworth, J. M. (1970). Growth of myxameobae of the cellular slime mould *Dictyostelium discoideum* in axenic culture. *The Biochemical Journal*, 119(2), 1714.

[166] Weiner M. P.,Costa G. L., Schoettlin W., Cline J., Mathur E. and Bauer J. C. (1994). Site-directed mutagenesis of double-stranded DNA by the polymerase chain reaction., *Gene*, 151, 119–123.

[167] Vervoort, E. B., Ravestein, A. V., Peij, N. N. V., Heikoop, J. C., Haastert, P. J. V., F. Verheijden, G., & Linskens, M. H. (2000). Optimizing heterologous expression in Dictyostelium: importance of 5′ codon adaptation. *Nucleic acids research*, 28(10), 2069-2074.

[168] Eichinger, L., Pachebat, J. A., Glckner, G., Rajandream, M. A., Sucgang, R., Berriman, M., ... & Tunggal, B. (2005). The genome of the social amoeba *Dictyostelium discoideum. Nature*, 435, 43–57.

[169] Veltman, D. M., Akar, G., Bosgraaf, L., & Van Haastert, P. J. M. (2009). A new set of small, extrachromosomal expression vectors for *Dictyostelium discoideum. Plasmid*, 61(2), 110118.

[170] Kuwayama S., pHK12 シリーズベクターについて., http://nenkin.lab.nig.ac.jp/assets/pHK12series.pdf

[171] Gaudet, P., Pilcher, K. E., Fey, P., & Chisholm, R. L. (2007). Transformation of *Dictyostelium discoideum* with plasmid DNA. *Nature protocols*, 2(6), 1317.

[172] Kuwayama S., モデル生物 細胞性粘菌 NBRP トレーニングコース用実験手引書., http://nenkin.lab.nig.ac.jp/beginners_guide

Publication List

Fukushima, S., Matsuoka, S. and Ueda, M., "Excitable dynamics of Ras triggers spontaneous symmetry breaking of PIP3 signaling in motile cells", *Journal of Cell Science*, doi: https://doi.org/10.1101/356105., February 2019.

Watabe, M., Arjunan, S.N.V., Fukushima, S., Iwamoto, K., Kozuka, J., Matsuoka, S., Shindo, Y., Ueda, M. and Takahashi, K., "A computational framework for bioimaging simulation.", *PLoS One*,
doi: https://doi.org/10.1371/journal.pone.0130089, July 2015.

Oral presentation

Fukushima, S., Matsuoka, S., Ueda, M., "Observation and modeling of Ras dependent PIP3 localization pattern formation", 第 56 回日本生物物理学会年会, 2A1436, 岡山, 岡山大学 津島キャンパス, September 2018.

Fukushima, S., Matsuoka, S., Ueda, M., "Ras の興奮性から生まれる PIP3 局在パターンの解析", 理研シンポジウム「細胞システムの動態と論理 X」, 1-4, 埼玉, 国立研究開発法人理化学研究所 生物科学研究棟, April 2018.

Fukushima, S., Matsuoka, S., Ueda, M., "自発的な運動を生む自己組織的な極性形成メカニズムの解析", 生体運動班会議, 13, 東京, 法政大学 市ヶ谷キャンパス, January 2018.

Fukushima, S., Matsuoka, S., Ueda, M., "PIP3 代謝に関わる分子の包括的な観察による GTP 型 Ras 依存的な局在パターン形成の解明", 第 69 回日本細胞生物学会大会, T6-01, 仙台, 仙台国際センター, June 2017.

Fukushima, S., Matsuoka, S., Ueda, M., "自己組織的なＰＩＰ３局在形成メカニズムの解析", 「理論と実験」２０１６, 5-2, 広島県, 広島大学, October 2016.

Fukushima, S., Matsuoka, S., Ueda, M., "多階層同時イメージングによる細胞の極性形成における自己組織化メカニズムの解明", 新学術領域"動く細胞と秩序"第 4 回若手の会, 熊本県, 火の国ハイツ, September 2014.

Poster presentation

Fukushima, S., Matsuoka, S., Ueda, M., "Excitable signaling network governs self-organized localization pattern for spontaneous cell migration ", Gordon Research Conference: Oscillations and Dynamic Instabilities in Chemical Systems, Mon/Tue 14, Les Diablerets, Les Diablerets Conference Center, Switzerland, July 2018.

Fukushima, S., Matsuoka, S., Ueda, M., "Analysis and Modelling of Self-organized PIP3 Localization ", Gordon Research Conference: Directed Cell Migration, 1-24, Galveston, Hotel Galvez, TX, Janualy 2017.

Fukushima, S., Matsuoka, S., Ueda, M., "Single-molecule Analysis of Regulating Mechanism of PI3K in Polarized Cells ", Gordon Research Conference: Single-Molecule Microscopy, 30, Hong Kong, The Chinese University of Hong Kong, China, June 2016.

Fukushima, S., Matsuoka, S., Ueda, M., "細胞の極性形成における PIP3 自己組織化メカニズムの解析", 理研シンポジウム「細胞システムの動態と論理 VIII」, 5, 埼玉, 国立研究開発法人理化学研究所 生物科学研究棟, April 2016.

Fukushima, S., Matsuoka, S., Ueda, M., "Positive feedback loop composed by PI3K and Ras regulates self-organization of PIP3. ", 第 53 回日本生物物理学会年会, 1P161, 金沢県, 金沢大学, September 2015.

Fukushima, S., Matsuoka, S., Ueda, M., "Analysis of the Regulation Mechanism of PI3K Activity by Live-cell Single-molecule Imaging. ", 第 52 回日本生物物理学会年会, 3P083, 北海道, 札幌コンベンションセンター, September 2014.

Fukushima, S., Matsuoka, S., Ueda, M., "Simultaneous Imaging of Single-molecule and Bulk Localization of PTEN. ", Biophysical Society 58th Annual Meeting, 2625-Pos, Moscone Center, San Francisco, CA, USA, February 2014.

Fukushima, S., Matsuoka, S., Ueda, M., "Simultaneous Imaging of Single-molecule and Bulk Localization of PTEN", 第 51 回日本生物物理学会年会, 2P297, 京都, 国立京都国際会館, October 2013.

Fukushima, S., Matsuoka, S., Ueda, M., "Simultaneous Imaging of Single-molecule and Bulk Localization of PTEN", 日本細胞性粘菌学会第 3 回例会, 京都, 京都大学, October 2013.

Fukushima, S., Matsuoka, S., Ueda, M., "2 波長同時イメージングによる PTEN の膜局在と 1 分子の同時解析", 日本顕微鏡学会第 69 回学術講演会, 21-P31, 大阪府, ホテル阪急エキスポパーク, May 2013.

Acknowledgement